UNIVERSITAT POLITÈCNICA DE VALÈNCIA

Escuela Técnica Superior de Ingeniería del Diseño

UNIVERSITAT POLITÈCNICA DE VALÈNCIA

Escuela Técnica Superior de Ingeniería Aeroespacial y Diseño Industrial

Análisis numérico del quemador Cambridge Spray Swirl Burner alimentado con diferentes combustibles

Trabajo Fin de Máster

Máster Universitario en Ingeniería Aeronáutica

AUTOR/A: Martínez Ruiz, Laura

Tutor/a: García-Cuevas González, Luis Miguel

Cotutor/a externo: CIOTTOLI, PIETRO PAOLO

CURSO ACADÉMICO: 2022/2023

UNIVERSITAT POLITÈCNICA DE VALÈNCIA

Escuela Técnica Superior de Ingeniería del Diseño

Universitat Politècnica de València
escuela técnica superior de ingeniería del diseño

NUMERICAL ANALYSIS OF THE CAMBRIDGE SPRAY SWIRL BURNER FUELED WITH DIFFERENT FUELS

MASTER'S THESIS
MASTER'S DEGREE IN AEROSPACE ENGINEERING

Author:
Laura Martínez Ruiz
Tutor:
Luis Miguel García-Cuevas González
External tutor:
Pietro Paolo Ciottoli
External co-tutor:
Jacopo Liberatori

ACADEMIC YEAR 2022-2023

Acknowledgements

I would like to express my gratitude to my family for supporting me throughout my training and giving me the opportunity to participate in a mobility program. It has been one of the greatest experiences of my life.

To all my friends, especially those I met in Rome, who have provided invaluable support to carry out this project.

To Elfi, who consistently supports me in every aspect of my life and whose judgment I can always rely on.

I also want to express my gratitude to Jacopo Liberatori, my co-tutor at La Sapienza University, for giving me his knowledge, support and encouragement. With his help, I have created a project that I am extremely proud of.

Finally, I would like to thank my tutors, professors Pietro Paolo Ciottoli and Luis Miguel García-Cuevas González for giving me advice and guiding me in this process of completing my master's thesis.

Laura Martínez, Valencia, September 2023

Abstract

The pollution problem has reached global dimensions and all governments must face its consequences. The transport sector is one of the dominant sectors in which new technologies are being investigated to reduce the emissions of pollutants and greenhouse gases. The aerospace sector is also immersed in this task, among the alternatives are SAFs (Sustainable Aviation Fuels).

The impact of unusual physical and chemical properties of SAFs may deeply affect the performance and operability of engines, e.g., in terms of altitude relight, lean blow-off, and cold start. The CFD (Computational Fluid Dynamics) tool is an essential tool to carry out these investigations. In this study, a Swirl Burner that has been previously studied by Cambridge University with different fuels is reviewed to analyse their characteristics using a URANS (Unsteady Reynolds-Averaged Navier-Stokes) simulation in OpenFOAM.

With this objective, different simulations are carried out: two cold gas and three reactive with heptane. The cold gas simulations have been successfully validated with experimental results from the official Cambridge repository. The first heptane simulation is made with a single-step chemical reaction, useful as a preliminary study for the ones with the chemical mechanisms. Two mechanisms are tested out one with 52 species and the other with 37 species. When compared with the experimental results, the first has managed to represent the flame in a qualitative way but the lift-off phenomenon appears. The second mechanism is not valid since the flame was extinguished when the simulation started. This project makes clear the need to continue investigating the limits and characteristics of combustion to develop numerical methods and move towards a more sustainable future in the field of engines.

Keywords: climate-neutral aviation; sustainable aviation fuels; swirl burner; computational fluid dynamics; chemical mechanism

Resumen

El problema de la contaminación ha alcanzado dimensiones globales y todos los gobiernos deben afrontar sus consecuencias. El sector del transporte es uno de los sectores dominantes en el que se investigan nuevas tecnologías para reducir las emisiones de contaminantes y gases de efecto invernadero. El sector aeroespacial también está inmerso en esta tarea, entre las alternativas se encuentran los SAF (*Sustainable Aviation Fuels*).

El impacto de las propiedades físicas y químicas inusuales de los SAF puede afectar profundamente el rendimiento y la operatividad de los motores, por ejemplo, en términos de reencendido en altitud, *blow-off* y arranque en frío. La herramienta CFD (*Computational Fluid Dynamics*) es una herramienta imprescindible para realizar estas investigaciones. En este estudio se revisa una cámara de combustión con *swirl* que ha sido previamente estudiado por la Universidad de Cambridge con diferentes combustibles para analizar sus características mediante una simulación URANS (*Unsteady Reynolds-Averged Navier-Stokes*) en OpenFOAM.

Con este objetivo, se realizan diferentes simulaciones: dos con gas frío y tres reactivas con heptano. Las simulaciones de gas frío han sido validadas con éxito con los resultados experimentales del repositorio oficial de Cambridge. La primera simulación de heptano se realiza con una reacción química de un solo paso, útil como estudio preliminar para los mecanismos químicos. Se prueban dos mecanismos, uno con 52 especies y el otro con 37 especies. En comparación con los resultados experimentales, el primero ha conseguido representar la llama de forma cualitativa pero aparece el fenómeno de *lift-off*. El segundo mecanismo no es válido ya que la llama se apagó al iniciar la simulación. Este proyecto deja clara la necesidad de seguir investigando los límites y características de la combustión para desarrollar métodos numéricos y avanzar hacia un futuro más sostenible en el campo de los motores.

Palabras clave: aviación climáticamente neutra; combustibles sostenibles de aviación; cámara de combustión con *swirl*; mecánica de fluidos computacional; mecanismo químico

Resum

El problema de la contaminació ha assolit dimensions globals i tots els governs deuen afrontar les seues conseqüències. El sector del transport és un dels sectors dominants en el que s'investiguen noves tecnologies per reduir les emissions de contaminants i gasos d'efecte hivernacle. El sector aeroespacial també està immers en aquesta tasca, entre les alternatives es troben els SAF (*Sustainable Aviation Fuels*).

L'impacte de les propietats físiques i químiques inusuals dels SAF pot afectar profundament el rendiment i l'operativitat dels motors, per exemple, en termes de reencesa en altitud, *blow-off* i arrencada en fred. L'eina CFD (*Computational Fluid Dynamics*) és una eina imprescindible per fer aquestes investigacions. En aquest estudi es revisa una càmera de combustió amb *swirl* que ha estat prèviament estudiat per la Universitat de Cambridge amb diferents combustibles per analitzar-ne les característiques mitjançant una simulació URANS (*Unsteady Reynolds-Averged Navier-Stokes*) amb OpenFOAM

Amb aquest objectiu, es realitzen diferents simulacions: dos amb gas fred i tres reactives amb heptà. Les simulacions de gas fred han sigut validades amb èxit amb els resultats experimentals del dipòsit oficial de Cambridge. La primera simulació d'heptà es realitza amb una reacció química d'un sol pas, útil com a estudi preliminar per als mecanismes químics. Se proven dos mecanismes, un amb 52 espècies i l'altre amb 37 espècies. En comparació amb els resultats experimentals, el primer ha aconseguit representar la flama de forma qualitativa però apareix el fenomen de *lift-off*. El segon mecanisme no és vàlid ja que la flama es va apagar al iniciar la simulació. Aquest projecte deixa clara la necessitat de seguir investigant els límits i les característiques de la combustió per desenvolupar mètodes numèrics i avançar cap a un futur més sostenible en el camp dels motors.

Paraules clau: aviació climàticament neutra; combustibles sostenibles d'aviació; càmera de combustió amb *swirl*; mecànica de fluids computacional; mecanisme químic

Contents

List of Figures

List of Tables

Acronyms

I Project report **1**

1 Introduction **2**
1.1 State of the art . . . 3
1.1.1 Impact of aviation in the environment . . . 3
1.1.2 Aviation fuels . . . 4
1.1.3 Studies with CFD . . . 5
1.1.4 Cambridge Swirl Burner . . . 6
1.2 Objectives of the project . . . 6
1.3 Project Structure . . . 7

2 Theoretical Background **9**
2.1 Gas turbine combustors . . . 9
2.1.1 The design of a GTC . . . 10
2.2 Classification of flames . . . 11
2.2.1 Laminar premixed flames . . . 12
2.2.2 Laminar nonpremixed flames . . . 12
2.2.3 Combustion in turbulent flows . . . 12
2.3 Swirling flows in combustion . . . 14
2.3.1 Vortex breakdown in a confined burner . . . 15
2.3.2 Swirl for reduction of pollutant emissions . . . 17
2.3.3 Swirl characterization . . . 18
2.4 Combustion chemical reactions . . . 19
2.5 Computational fluid dynamics (CFD) . . . 21
2.5.1 Turbulent flow . . . 21
2.5.2 RANS approach . . . 24
2.5.3 High-Reynolds Number Linear Eddy Viscosity Models . . . 26
2.5.4 Turbulent boundary layers . . . 27
2.6 Eddy Dissipation Concept (EDC) . . . 29
2.7 Finite Volume Method . . . 30
2.8 Mesh . . . 32
2.8.1 Mesh induced errors . . . 33
2.9 Interpolation schemes . . . 34
2.10 Temporal discretization . . . 35
2.11 Algorithms . . . 36

2.11.1 Pressure correction methods . . . 36
2.11.2 Relaxation factor . . . 36
2.11.3 SIMPLE . . . 36
2.11.4 PISO . . . 38
2.11.5 PIMPLE . . . 40
2.11.6 Density correction methods . . . 40
2.12 Other models . . . 41
2.12.1 Sutherland's model . . . 41
2.12.2 Arrhenius's law . . . 41
2.12.3 Ranz Marshall correlation . . . 41
2.12.4 Rosin Rammler distribution . . . 42
2.12.5 Reitz Diwakar model . . . 42
2.12.6 Sphere drag . . . 43
2.12.7 Partially Stirred Reactor model (PaSR) . . . 43

3 Case Setup **45**
3.1 Geometry . . . 45
3.2 Swirl Generation . . . 47
3.3 Software used for the project's development . . . 48
3.3.1 OpenFOAM . . . 48
3.3.2 ParaView . . . 49
3.4 Mesh . . . 49
3.5 Test cases . . . 51
3.6 Directory structure . . . 51
3.6.1 Constant folder . . . 52
3.6.2 System folder . . . 53
3.6.3 Chemkin folder . . . 55

4 Results and discussion **56**
4.1 Cold gas simulations . . . 56
4.1.1 C1 case . . . 56
4.1.2 C2 case . . . 63
4.2 Reacting simulations: Heptane (H1S1) . . . 66
4.2.1 H1S1: One step chemical reaction . . . 66
4.2.2 H1S1: CERFACS chemical mechanism . . . 79
4.2.3 H1S1: High-temperature chemical mechanism . . . 89

5 Conclusions and Future Work **92**
5.1 Conclusions . . . 92
5.2 Future work . . . 94

II Economic cost **95**

6 Economic cost **96**
6.1 Personnel expenditure . . . 96
6.2 Operational cost . . . 97
6.3 Equipment costs . . . 98
6.4 Total cost . . . 99

III Terms and conditions **100**

7 Terms and conditions **101**
7.1 Legal framework 101
7.1.1 General conditions 101
7.1.2 UPV master's thesis regulations 102
7.2 Carbon footprint of the project 104

Bibliography **106**

A Degree of alignment of the project with the Sustainable Development Goals. **110**

List of Figures

1.1 Fuel consumption and aircraft fuel burn per seat. [12] . . . 3
1.2 Direct CO_2 emissions from fossil jet kerosene combustion; emissions from biojet kerosene are accounted for as net zero emissions, as per United Nations Framework Convention on Climate Change (UNFCCC) accounting. [24] . . . 4

2.1 Main components of a conventional combustor.[33] . . . 10
2.2 Bluff body vortices scheme. [41] . . . 11
2.3 Diagram for premixed turbulent combustion. [29] . . . 13
2.4 Turbulent non premixed flames. [29] . . . 14
2.5 (a) Mean axial velocity, u, with identification of Wake Recirculation Zone (WRZ), Corner Recirculation Zone (CRZ) and Toroidal Recirculation Zone (CTRZ) and the zero axial velocity isolines in the longitudinal plane of the burner; (b) Vorticity magnitude contours. [46] . . . 15
2.6 Representation of the helical structure of PVC. [9] . . . 16
2.7 Burner configuration. [6] . . . 16
2.8 Fields of axial and azimutal velocities under-reacting and non-reacting conditions. [6] 17
2.9 Variation of EINOx versus O_2 addition for equivalence ratios of 0.8, 0.9, and 1 and swirl numbers (S) of 0.8 and 1.4. [38] . . . 18
2.10 Cylindrical coordinate system for the swirling flow and their corresponding velocities. [30] . . . 19
2.11 Turbulent energy cascade. [15] . . . 22
2.12 Energy cascade of turbulent kinetic energy (logarithmic scale). [22] . . . 24
2.13 Control volume example for the finite volume method. [14] . . . 31
2.14 Example of a structured triangular mesh and an unstructured triangular mesh in a unit box. [20] . . . 33
2.15 Orthogonal and skew mesh. [17] . . . 34
2.16 Non-orthogonal and non-skew mesh. [17] . . . 34
2.17 SIMPLE process. [36] . . . 38
2.18 PISO algorithm. [10] . . . 39
2.19 PIMPLE algorithm scheme. [11] . . . 40
2.20 Reitz-Diwakar break-up processes. [25] . . . 43

3.1 Cambridge swirl burner scheme with dimensions.[44] . . . 45
3.2 Burner Geometry. . . . 46
3.3 Burner Geometry. . . . 46
3.4 Swirler of the Cambridge Swirl Burner. [7] . . . 47
3.5 Air Annulus of the Cambridge swirl burner. [7] . . . 47
3.6 Mesh. . . . 50
3.7 Mesh details. . . . 50

4.1 (a) Temperature field for the C1 case. (b) Velocity field for the C1 case. . . . 56
4.2 Axial and radial velocities for the C1 case. . . . 57

4.3 Axial velocities for the cold gas case C1. . . . 58
4.4 Comparison between experimental and numerical results of the axial velocities for the cold gas case C1. . . . 59
4.5 Radial velocities for the cold gas case C1. . . . 60
4.6 Comparison between experimental and numerical results of the radial velocities for the cold gas case C1. . . . 61
4.7 Swirl velocities for the cold gas case C1. . . . 62
4.8 Comparison between experimental and numerical results of the swirl velocities for the cold gas case C1. . . . 63
4.9 Velocity field for the C2 case. . . . 64
4.10 Streamlines with axial and radial velocities for the C2 case. . . . 64
4.11 Axial velocities for the cold gas case C2. . . . 65
4.12 Comparison between experimental and numerical results of the axial velocities for the cold gas case C1. . . . 66
4.13 Mass fraction of reactants for the one step heptane case. . . . 67
4.14 Mass fraction of products for the one step heptane case. . . . 68
4.15 Inert gas mass fraction for the one-step heptane case. . . . 68
4.16 Mass fractions for different Z normal surfaces along the burner. . . . 69
4.17 Temperature field for the one-step heptane case. . . . 70
4.18 Velocity field for the one-step heptane case. . . . 70
4.19 Velocity streamlines in a Y normal slice for the one step heptane case. . . . 71
4.20 Velocity streamlines within the velocity field for the one-step heptane case. . . . 71
4.21 Density field for the one-step heptane case. . . . 72
4.22 Reaction rate for the one-step heptane case (logarithmic scale). . . . 72
4.23 Eddy Dissipation Concept (EDC) for the one step heptane case. . . . 73
4.24 Droplets diameter within fuel mass fraction. Droplets scale= $10 \cdot d$. . . . 74
4.25 Droplets temperature. . . . 74
4.26 Vaporization rate of droplets. Droplets scale= $10 \cdot d$. . . . 75
4.27 Reaction Rate for different time instants for the one-step heptane case. . . . 76
4.28 Temperature field for different time instants for the one step heptane case. . . . 77
4.29 Velocity field with streamlines (radial and axial) for different time instants for the one step heptane case. . . . 78
4.30 Temperature field with the CERFACS mechanism for the heptane reacting case. (time=0.2538s) . . . 79
4.31 Velocity field with the CERFACS mechanism for the heptane reacting case with streamlines for the radial and axial velocity. (time=0.2538s) . . . 80
4.32 Reaction Rate with the CERFACS mechanism for the heptane reacting case with a logarithmic scale. (time=0.2538s) . . . 81
4.33 Major combustion products with the CERFACS mechanism for the heptane reacting case. (t=0.2538s) . . . 82
4.34 Intermediate combustion products with the CERFACS mechanism for the heptane reacting case. (t=0.2538s) . . . 83
4.35 Mass fraction of some species along the longitudinal axis of the burner. (t=0.2538s) . 83
4.36 Pressure field with the CERFACS chemical mechanism for the heptane reacting case. (t=0.2538s) . . . 84
4.37 Experimental OH measurements obtained through various methods from the University of Cambridge repository. [51] [50] . . . 85
4.38 Results obtained using the OpenFOAM software for the reactive case of heptane with the CERFACS chemical mechanism. The reaction rate is shown on a logarithmic scale. 85
4.39 (a) Schematic of a swirled jet flow in a combustion chamber with its inner (ISL) and outer (OSL) shear layers and the inner (IRZ) and outer (ORZ) recirculation zones. (b) V flame. (c) M flame. [18] . . . 86

4.40 Comparison of the axial velocities obtained through OpenFOAM and the experimental data from the Cambridge University repository. 87
4.41 Temperature field for different time instants with the CERFACS chemical mechanism for the n-heptane reacting case. 88
4.42 Reaction rate for different time instants with the CERFACS chemical mechanism for the n-heptane reacting case (logarithmic scale). 89
4.43 Temperature for different time instants with the high-temperature chemical mechanism for the n-heptane reacting case. 90
4.44 Reaction rate for different time instants with the high-temperature chemical mechanism for the n-heptane reacting case (logarithmic scale). 90

6.1 Pie chart of the total project costs. 99

List of Tables

3.1 Test cases conditions. 51
3.2 Solution subdictionaries for the case of study. 54

6.1 Personnel cost for the project. 97
6.2 Social security contributions. 97
6.3 Software license costs. 98
6.4 Total project electricity consumption cost. 98
6.5 Electronic equipment cost for the completion of the project. 99
6.6 Total cost of the project. 99

A.1 Degree of alignment of the project with the Sustainable Development Goals of the 2030 agenda. 110

Acronyms

ACARE Advisory Council for Aeronautics Research in Europe

CDS Centered Difference Scheme

CERFACS Centre Europeén de Recherche et de Formation Avancée en Calcul Scientifique

CFD Computational Fluid Dynamics

CRZ Corner Recirculation Zone

CTRZ Central Toroidal Recirculation Zone

DIC Diagonal Incomplete-Cholesky

DILU Diagonal Incomplete-LU

DNS Direct Numerical Simulation

EDC Eddy Dissipation Concept

FDS Flux Difference Splitting Schemes

FVM Finite Volume Method

GAMG Geometric Algebraic Multigrid

HVO Hydrogenated Vegetable Oil

IRZ Internal Recirculation Zone

ISL Inner Shear Layer

JANAF Joint Army–Navy–Air Force

LES Large Eddy Simulation

LHV Lower Heating Value

OSL Outer Shear Layer

PaSR Partially Stirred Reactor model

PCG Preconditioned Conjugate Gradient

PDA Phase Doppler Anemometer

PISO Pressure-Implicit with Splitting of Operators

PLIF Planar Laser Induced Fluorescence

PSR Perfectly Stirred Reactor

PVC Precession Vortex Core

QSSA Quasy Steady State Assumption

QUICK Quadratic Upstream Interpolation for Convective Kinematics

RAS Reynolds Averaged Simulation

SAF Sustainable Aviation Fuels

SIMPLE Semi-Implicit Method for Pressure Linked Equations

SMD Sautter Mean Diameter

UNFCCC United Nations Framework Convention on Climate Change

UPV Universitat Politècnica de València

WRZ Wake Recirculation Zone

Nomenclature

Latin symbols

t	Time	s
NO_x	Nitrogen oxides	
SO_x	Sulfure oxides	
$VOCs$	Volatile Organic Compounds	
PM	Particulate Material	
l	Length scale	m
`L`	Viscous length	m
`U`	Friction velocity	m/s
A	Area	m^2
C_D	Drag coefficient	
D	Drag force	N
$EINOx$	Nitrogen Oxides Emission Index	
G_{ax}	Axial momentum flux	$kg \cdot m/s^2$
G_{tg}	Axial flux of tangential momentum	$kg \cdot m/s^2$
h	Enthalpy	J
k	Turbulent kinetic energy	J
L	Characteristic length	m
L^*	Length scale	m
Nu	Nusselt number	
P	Pressure	Pa
Pr	Prandtl number	
R	Radius	m
Re	Reynolds number	
RR	Reaction rate	$J/(kg \cdot m^3)$
S	Swirl number	

S_μ	Sutherland constant	
T	Temperature	K
S	Swirl number	
S	Swirl number	
Y	Mass fraction	
$\tilde{Y^*}$	Favre-averaged mass fraction	
u^*	Velocity scale	m/s
U_θ	Swirl velocity	m/s
u'	Fluctuation velocity (turbulence)	m/s
$\dot{m}$	Mass flow rate	kg/s

Greek Symbols

α	Relaxation factor	
$\bar{\rho}$	Mean density of the mixture	kg/m^3
χ	Reactivity factor	
ϵ	Dissipation rate of turbulent kinetic energy	J/kg/s
γ_λ	Mass fraction of fine structures	
κ	Wave number associated to eddy structures	m^{-1}
μ	Dynamic viscosity	kg/m/s
ν	Kinematic viscosity	m^2/s
ϕ	Equivalence ratio	
ρ	Density	kg/m^3
τ	Time scale	s
$\tau_{z,r}$	Shear stress acting on the z,r plane	Pa
$\tau_{r,\theta}$	Shear stress acting on the r, θ plane	Pa
θ	Swirl intensity	
$\tilde{\omega}$	Production rate	

Subscripts

t	Turbulent
c	Chemical
mix	Mixing
η	Kolmogorov
j	jth species

K	At Kolmogorov scale
a	Activation
b	Burnt mixture (Laminar premixed flames)
u	Unburnt mixture (Laminar premixed flames)
$bulk$	Bulk
z	Axial
y	Radial
θ	Azimuthal or swirl

Part I

Project report

Chapter 1

Introduction

In recent years, the world of engineering has been facing one of its greatest challenges, addressing the devastation caused by pollution and greenhouse gases and moving towards a sustainable future. Government measures are becoming stricter to address the significant amount of current emissions, which are already having many effects on human quality of life and the environment. The aerospace industry is also immersed in this same challenge, as part of the transportation system, contributing to emissions due to the burning of fossil fuels.

While aviation is not the sector that contributes the most to pollution, the number of passengers per year has continued to increase. Strict pollution policies and societal concerns about it have led to a significant portion of research within the sector being focused on making airplanes more efficient.

The reduction of emissions from commercial airplanes involves both the aerodynamic design of the aircraft and the engine itself, along with airspace traffic control. With improvements in these three areas, a reduction of up to 50% in pollution is anticipated. This is one of the goals of Advisory Council for Aeronautics Research in Europe (ACARE).

This master's thesis will focus on the field of engines, more specifically on the combustion chamber. Aeronautical engines have greatly improved their operation. Fuel efficiency has improved, and specific consumption has been reduced by almost 40% (Figure 1.1). The amount of fuel burned per seat has decreased, but the total amount of fuel burned per year is increasing, and the forecast is that it will continue to increase due to the high demand of passengers.

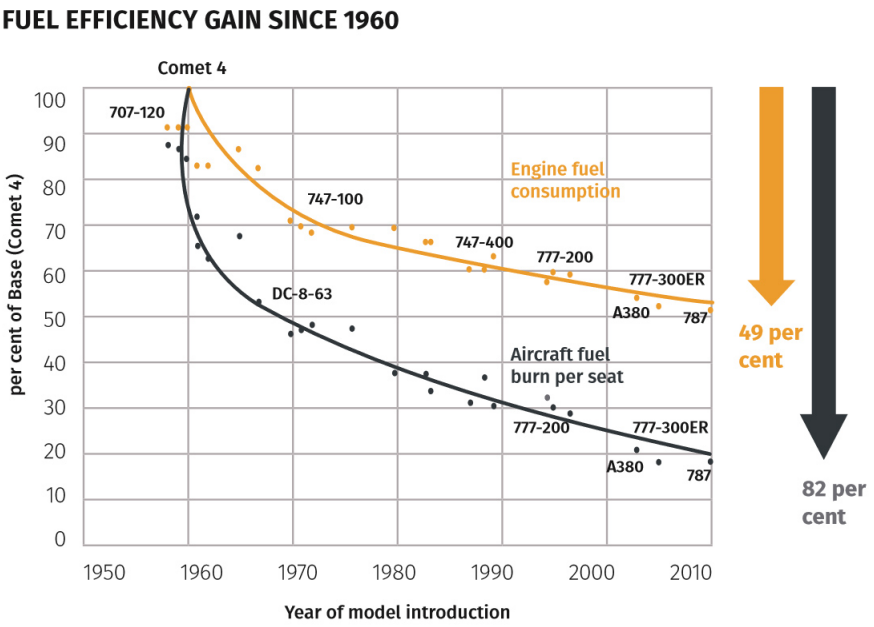

Figure 1.1: Fuel consumption and aircraft fuel burn per seat. [12]

All of this context has forced the industry and its engineers to develop even more efficient combustors, in terms of pollution. The development of an aeronautical engine is of great complexity; even the development of a small part requires a substantial investment in resources and time, as well as a large team of professionals. Since the 1960s, a series of computer programs with numerical systems capable of solving fluid mechanics problems have been developed, a branch of physics essential for studying combustion systems, among others. These Computational Fluid Dynamics (CFD) programs have become established in the field of engineering, allowing for the simulation of numerous problems of varying scales. However, the accurate configuration of one of these problems demands extensive expertise to achieve optimal results. The validation and interpretation of the results from these programs and numerical systems are of vital importance to extract valuable conclusions for research. This is the focal point of this project.

1.1 State of the art

1.1.1 Impact of aviation in the environment

Air transportation has become a vital mode of transport for people and goods all around the world. With the increasing globalization of economies and the growth of tourism, the number of people travelling by air has been growing rapidly. However, this growth in air travel has led to an increase in the amount of pollution and greenhouse gas generated by commercial aviation, which has become a significant environmental concern (Figure 1.2). Commercial aviation has a substantial impact on both local and global air quality, contributing to climate change, acid rain, and other environmental issues. This impact has raised serious concerns about the sustainability of air travel and the need for effective measures to reduce its environmental impact.

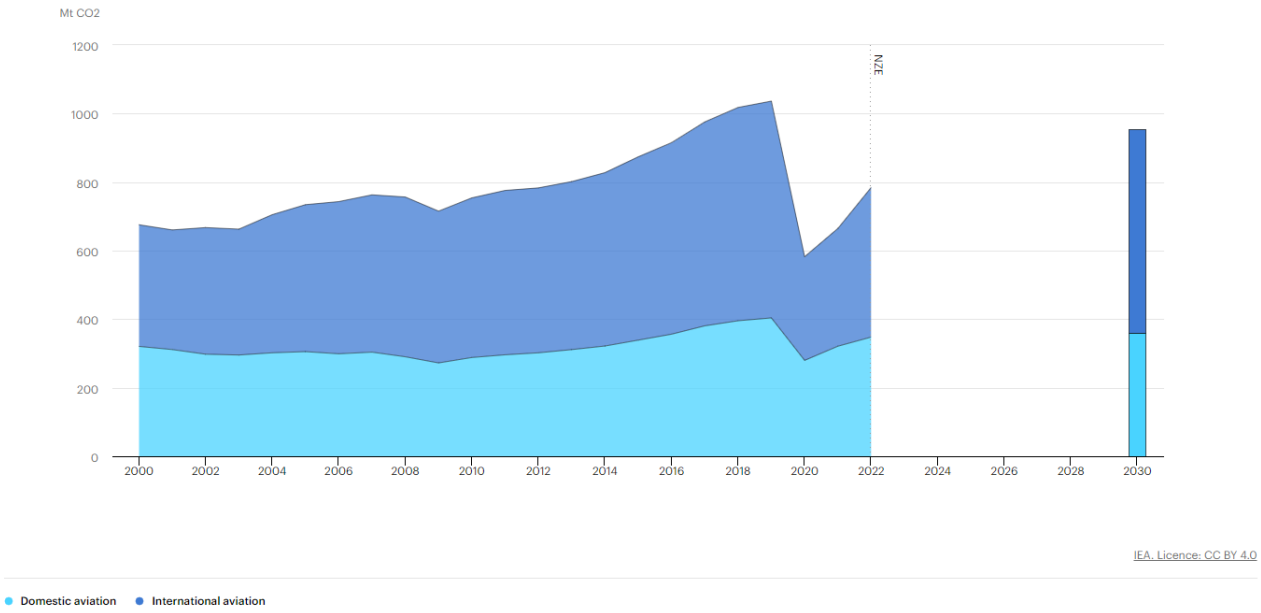

Figure 1.2: Direct CO_2 emissions from fossil jet kerosene combustion; emissions from biojet kerosene are accounted for as net zero emissions, as per United Nations Framework Convention on Climate Change (UNFCCC) accounting. [24]

Quantifying what was explained above, the aviation sector is responsible for 3.5% of all drivers of climate change due to human activities. The calculated CO_2 emissions due to aviation between 1940 and 2018 are 32.6 billion tons. [31]

The environmental problem has global dimensions and involves the entire planet. The current activity of the human being has accelerated this problem, increasing the emissions of polluting agents. That is why every day more efforts are invested in developing new technologies capable of avoiding emissions both in the sense of pollution and greenhouse effects. Aviation is not exempt from this problem and is also part of this movement that represents one of the greatest challenges for today's generation of scientists.

1.1.2 Aviation fuels

Traditional aviation fuels, such as kerosene, are fossil fuels that are derived from crude oil. They have been the primary fuel used in commercial aviation for many decades, and their combustion produces significant amounts of air pollutants and greenhouse gases. These emissions contribute to air pollution and have a negative impact on the environment and human health.

The combustion of kerosene in aircraft engines results in the emission of several air pollutants and greenhouse gases. These include carbon dioxide (CO_2), nitrogen oxides (NOx), sulfur oxides (SOx), particulate matter (PM), and volatile organic compounds (VOCs). CO_2 is an important greenhouse gas that contributes to climate change, while NOx, SOx, PM, and VOCs contribute to air pollution, which can cause respiratory problems, cardiovascular disease, and other health issues.

As has been explained, traditional aviation fuels have an important role in pollution and climate change. That is why, a huge number of investigations have the objective of developing alternatives for this industry to become environmentally friendly, if possible. These investigations include the development of alternative fuels such as biofuels, synthetic fuels and hydrogen, among others. These

have the potential to reduce emissions, but they present some disadvantages too.

Sustainable aviation fuels

Sustainable Aviation Fuels (SAF) are alternative fuels that have the potential to replace traditional aviation fuels like kerosene. These fuels are produced from renewable resources, such as waste oil, agricultural residues, and non-food crops, and can significantly reduce the environmental impact of air travel.

What is interesting about SAFs is that they can be used in aircraft without requiring significant modifications to engines and infrastructure. The idea is that they have a similar chemical composition to kerosene and can provide the same performance.

There are several types of SAF currently under development, including:

- Hydrogenated Vegetable Oil (HVO): made from vegetable oil, has a low carbon footprint and can reduce greenhouse gas emissions by up to 90%.
- Biojet fuel: made from a variety of renewable raw materials, including waste materials like cooking oil, municipal solid waste, and algae.
- Synthetic fuel: produced from renewable electricity and carbon dioxide, synthetic fuels have the potential to be carbon-neutral or even carbon-negative.
- Hydrogen: t has a higher Lower Heating Value (LHV) and energy per unit of mass than kerosene (33.33 kWh/kg and 12.14 kWh/kg, respectively), so it is a very interesting fuel to be considered. Plus, no carbon emissions are produced. Although, it presents a great drawback in terms of energy per unit of volume.

SAFs have already been successfully tested on commercial flights, and some airlines have started to incorporate them into their fuel mix. However, the widespread adoption of SAFs still faces several challenges, including the limited availability and high cost of production.

To fully replace kerosene with SAFs, significant investment and policy support are needed to scale up production and reduce costs. The aviation industry is working closely with governments, research institutions, and other stakeholders to accelerate the development and adoption of SAFs to mitigate the environmental impact of air travel.

1.1.3 Studies with CFD

The use of sustainable aviation fuels (SAFs) has the potential to significantly reduce the environmental impact of air travel. However, the characteristics of SAFs, such as their flammability limits and blow-off properties, differ from traditional aviation fuels like kerosene. As such, it is essential to conduct Computational Fluid Dynamics (CFD) studies to understand and optimize the combustion of SAFs in aircraft engines.

Flammability limits are the concentration ranges of fuel vapours in air that can support combustion. The flammability limits of SAFs are different from those of kerosene, and the combustion of SAFs requires different fuel-air ratios. CFD studies can help determine the optimum fuel-air ratio for SAFs, which can improve combustion efficiency and reduce emissions.

With computational fluid dynamic studies, it is possible to optimize some of the engine characteristics to improve SAFs performance. Some of these characteristics can be the injection system and the main chamber design. By conducting these studies, researchers can develop safer, more efficient, and more sustainable combustion systems for the aviation industry which can accelerate the adoption of SAFs and help the aviation industry meet its targets about the impact on the environment.

Given the complexity of CFD studies, it is preferable to first study a specific case with traditional fuels before examining the so-called SAFs (Sustainable Aviation Fuels) to validate the numerical schemes and algorithms used and ensure a proper representation through the software.

1.1.4 Cambridge Swirl Burner

The University of Cambridge has conducted a series of experiments on a swirl bluff-body burner with the aim of understanding local and global extinction mechanisms in swirl-stabilized flames.

The university has established a repository ([8]) that contains the data from experiments conducted on this burner using various fuels. The primary focus is on spray-injection fuels. This burner has been tested with both premixed and non-premixed flames. Those involved in this research hope that the provided data will be utilized to model a wide range of flame conditions and combustion phenomena using Computational Fluid Dynamics (CFD).

1.2 Objectives of the project

As previously mentioned, Computational Fluid Dynamics (CFD) is a powerful tool that requires proper validation and interpretation of results. The University of Cambridge provides experimental data for a specific geometry, the Swirl bluff-body burner. The experiments conducted on this burner range from cold gas simulations to various traditional fuels such as heptane, ethanol, and more. These data sets serve as a foundation for validating and fine-tuning CFD models, allowing for the simulation of a wide range of combustion scenarios and conditions. Specifically, the project will start by conducting simulations of cold gas cases, and then progress to reactive cases. The primary focus will be on heptane, which will be studied both as a single-step reaction and using reduced chemical mechanisms. The intention behind this approach is to systematically explore and validate the simulation process, moving from simpler scenarios to more complex and reactive conditions.

The main objective of this master's thesis project is to validate the Computational Fluid Dynamics (CFD) simulation of the Cambridge Swirl bluff-body burner using the models and numerical methods employed by the University of Rome, La Sapienza. This validation will involve a comparison of the CFD results with the experimental data from the Cambridge burner. The aim is to assess the accuracy and reliability of the CFD simulations conducted at La Sapienza by comparing them to the real-world experimental outcomes obtained from the Cambridge experiments. By utilizing the Cambridge repository for validation, this project seeks to contribute to the ongoing efforts to improve combustion simulation accuracy, ultimately aiding in the development of cleaner and more efficient combustion systems in the aerospace industry and beyond.

In addition to the main objective, one of the secondary goals of the project is to gain proficiency in using software like OpenFOAM, including its programming language (C++) and post-processing techniques for the simulated cases. It's worth noting that these simulations are unsteady (transient)

in nature. The project will also involve conducting simulations on a global scale, aiming to comprehend the chemical mechanisms and other widely used models in this type of simulation. Through this process, the project aims to not only achieve validation but also develop skills in using complex simulation tools, programming, and analysis techniques associated with unsteady combustion simulations.

Finally, the project serves as a practical application of concepts learned earlier during academic training in subjects such as combustion, computational fluid dynamics, gas turbine combustors, and more. It provides an opportunity to apply theoretical knowledge gained in these areas to a real-world scenario, enhancing the understanding of complex phenomena in combustion processes and the use of advanced simulation tools.

1.3 Project Structure

This project has been titled "Numerical Analysis Of The Cambridge Swirl Burner Fueled With Different Fuels" since the geometry proposed by Cambridge with cold gas and heptane is analyzed. The term "Fueled With Different Fuels" refers to the fact that different simulations are carried out with heptane and with different chemical treatments (chemical mechanisms). Furthermore, this master's thesis is the preliminary work for future research with more fuels.

The project report is structured as follows:

1. Introduction. The project proposal is introduced and its importance and motivation are justified. The current state of the field that encompasses the project is explained, and the research context is set. Additionally, the Cambridge repository, which is used for validating the simulations, is presented.

2. Theoretical background. In this chapter, a concise explanation of the necessary theory is provided to comprehend how the case setup has been conducted. Different sections within this chapter cover topics such as combustion and flames in general, the rationale behind employing swirling flows in combustion, as well as all the schemes and algorithms used in Computational Fluid Dynamics (CFD). Additionally, turbulence models and other relevant models used to simulate the study case are discussed.

3. Case setup. This chapter introduces the geometry employed in the project and explains how the swirl motion has been simulated. The software used for the simulations is presented, along with an explanation of the directory structure used for the OpenFOAM program. Moreover, this chapter elaborates on the schemes, algorithms, and conditions applied during the simulations.

4. Results and discussion. In this chapter, the obtained results from various study cases are presented, discussed, and justified. The results are analyzed and compared with both theoretical expectations and experimental data.

5. Conclusions and future work. The conclusions obtained during the project are detailed, and the steps to be taken in the future to continue this research are mentioned.

6. Economic cost. In this chapter, the economic cost of the project is calculated taking into account the personnel expenditure, the operational cost and the equipment cost.

7. Terms and conditions. The legal framework in which this project is immersed is explained and the carbon footprint of thesis is calculated.

Chapter 2

Theoretical Background

2.1 Gas turbine combustors

When mixing fuel and oxidizer in appropriate proportions, an exothermic reaction called combustion occurs. Combustion has been used for multiple purposes in history.

Within a gas turbine, the combustion chamber is where the combustion takes place to generate the energy that will power the system's operation. The objective of the combustion chamber is to burn large quantities of fuel (supplied by the nozzle) with air (supplied by the compressor). After this, the hot combustion products will be expanded and accelerated. All of this must happen with minimum pressure losses and maximum heat release.

The combustion process will have performance criteria that will help to assess the good behaviour of the combustor. These criteria will be: the capability of altitude relight, the auto-ignition and flashback possibility, the combustion stability and efficiency, the amount of pressure losses, the size and weight, the liner life and the exit temperature distribution (limited by the turbine).

The development of gas turbine combustors has to face high difficulties since the requirements for these combustors are more demanding as time passes. During the past half century, the combustion pressures have raised from 5 to 50 atmospheres, while the inlet air temperature has doubled and the outlet temperatures have raised from 1100 K to 1850 K. Despite the increasing severity of operating conditions, today combustors have close to 100% of combustion efficiency. However, some of the challenges that still remain are the following:

- Multi-fuel capability, as new technologies are being developed in order to reduce pollutant emissions. The rising price of petroleum fuel has forced the industry to develop alternative liquid fuels which require changes in the combustion design.
- Acoustic resonance, is a problem that happens when combustion instabilities become coupled with the acoustics of the combustor.
- Reduction of combustors size and weight while the trend develops toward a higher turbine inlet temperature.
- Greater reliability, durability, lower manufacturing and lower maintenance. This should be achieved with new materials and fabrication methods.
- Advanced wall cooling techniques.

These requirements must be reached ensuring high combustion efficiency as well as low pollutant and greenhouse gas emissions.

2.1.1 The design of a GTC

A conventional gas turbine combustor usually consists of the following regions and components:

1. Diffuser
2. Fuel nozzle
3. Primary zone
4. Intermediate zone
5. Dilution zone

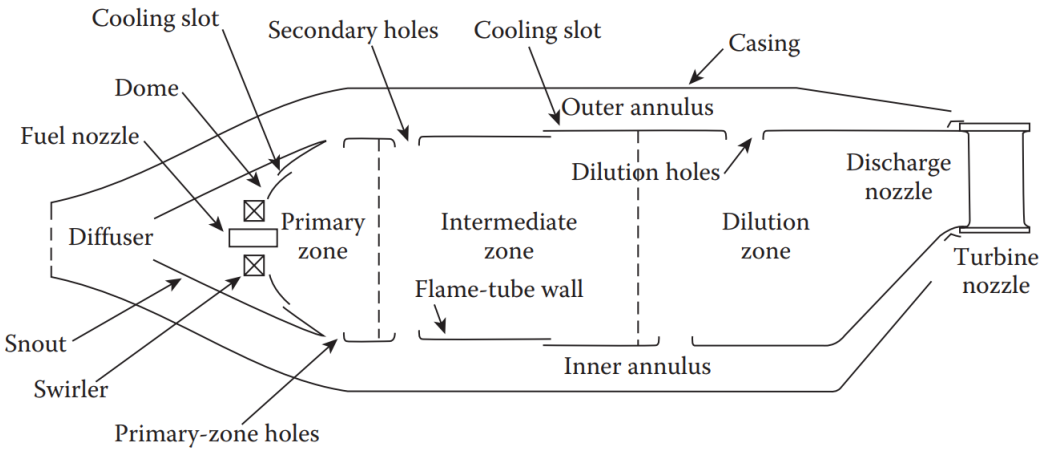

Figure 2.1: Main components of a conventional combustor.[33]

The combustor components are shown in the Figure 2.1.

When the air enters the main station, its velocity is too high for the combustion process since this air has come from the compressor. Burning fuel at high velocities has plenty of disadvantages, among these, the pressure losses in the combustor would be excessive. The function of the diffuser is to reduce flow velocity to help the combustion process, this means usually reducing the air velocity by about a fifth of its initial value.

The diffuser is usually a divergent duct. The length of this duct has some restrictions as well. If the duct is too short the flow will separate and stall causing pressure losses while if the diffuser is too long the pressure losses will increase due to friction. The optimum length will be the one that minimizes the total losses.

The air that has passed through the diffuser enters the primary zone. The primary zone is the zone where combustion is initiated. For this to happen the fuel must be atomized and vaporized.

The air entering the primary zone is still too fast to stabilize the flame. The air leaving the diffuser has a speed of about 25 m/s while the flame speed of a typical hydrocarbon is about 6 m/s. If the ignition of the flame is made under these circumstances it will be extinguished. This

occurs because the time available for combustion, that is, for the chemical reaction, is less than that necessary for ignition.

Bluff bodies are objects, such as a flat plate or V-gutter that are placed in the airflow (Figure 2.2). When the flow passes these objects, vortices are formed downstream. The velocity at the centre of the vortex is zero and will increase towards the tip of the vortex. This is a forced vortex. Combustion can start at the centre of the vortex, where the air velocity is low enough for the flame to be sustained. These vortices will break up and create a turbulence of smaller vortices. This turbulence will be positive because it can increase the rate of heat release and the amount of fuel burned, whereby the volume of fuel burned can be reduced.

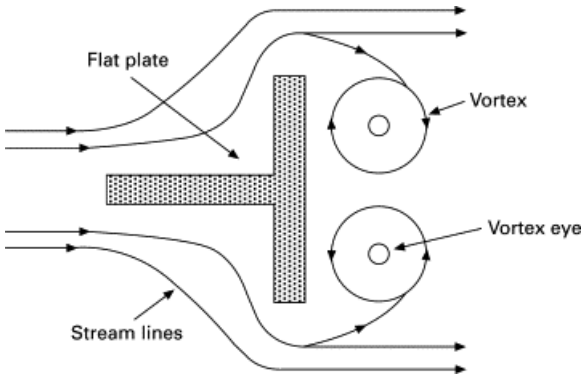

Figure 2.2: Bluff body vortices scheme. [41]

In the primary zone, both fuel and oxidizer are mixed with partially burned combustion products that are trapped in a recirculation flow, which will be explained and identified in the following sections.

In the intermediate zone the burning continues to happen toward completion. The equivalence ratio in the primary zone is around unity, the products of this zone will be unburned hydrocarbons and CO. The intermediate zone reduces these products by mixing small amounts of secondary air which will lean the mixture. Combustion should be complete by the final of the intermediate zone.

Finally, the dilution zone is where the remaining annulus air flow will be dumped through dilution holes into the hot gas stream. The hot gases are around 1800 K when they leave the intermediate zone, the dilution zone will ensure that the gas temperature entering the turbine is the right one.

2.2 Classification of flames

The mixture of oxidizer and fuel will be one of the decisive phenomena when assessing the quality of combustion. That is why the classification between premixed combustion and non-premixed combustion is probably one of the most important in combustion.

As already mentioned, before the combustion takes place, the oxidizer and the fuel must be mixed at molecular level. In addition, at least one of the reactants should be in gas or liquid phase, so that the molecules can disperse around the other reactant.

Premixed combustion is one that takes place when the reactants are well mixed before the reaction starts.

Non-premixed combustion reactants are brought together by the molecular process of diffusion and convective motion, in a common region where mixing and reaction take place simultaneously.

Once the difference between premixed combustion and non-premixed combustion has been explained, there is another important classification that must be made, the difference between laminar flames and flames in a turbulent regime.

2.2.1 Laminar premixed flames

In laminar premixed flames, it is possible to distinguish between unburned mixture and burnt mixture. The result is, when ignition occurs the flame propagates like a wave phenomenon. This type of reaction will be governed by the mass concentration of the deficient reactant. If a one-dimensional case is considered, the wave propagates with a velocity u_u.

Upstream of the wave, the mixture approaches the flame with speed u_u and temperature T_u. The subscript u refers to the term unburnt. Downstream of the wave, the mixture leaves the flame with a velocity u_b and a temperature T_b. The subscript b refers to "burnt".

2.2.2 Laminar nonpremixed flames

In most cases of combustion, fuel and oxidizer are not pre-mixed, as is the case study presented in this project.

This type of flame is made up of three zones, there is a reaction zone that separates the zone rich in fuel from the zone rich in oxidizer. The fuel and oxidizer are transported towards each other by diffusion and this will be accelerated if a convective system is added to improve the mixing.

This reaction occurs at a finite rate and the reaction zone has a finite thickness. Normally it is assumed that this type of reaction occurs infinitely fast, so what really determines the combustion rate are the transport ratios between fuel and oxidizer, which will therefore determine the heat release rate.

2.2.3 Combustion in turbulent flows

In reality, most combustion devices operate in turbulent flows. In a laminar flow, different streamlines can be distinguished, while in a turbulent flow, these streamlines do not exist and at any point in space the quantities fluctuate over time, it is possible to distinguish between the mean properties and the pulsating ones.

Turbulence in combustion has a positive impact in the sense that it improves the mixing between the reactants. However, it must be taken into account that excessive turbulence can cause local extinction, negatively affecting combustion efficiency.

As is known, turbulence is still one of the unsolved problems in the world of physics. Furthermore, with the combustion process, the complexity of the problem only increases. That is why the study of turbulent combustion has been mostly empirical until 1970.

To distinguish between turbulent and laminar flows, the well-known Reynolds number is used, which is a dimensionless parameter that characterizes the tendency of a flow to become unstable. For this reason, flows with a high Reynolds number are turbulent while those with a low Reynolds number are laminar. One of the reasons why a high Reynolds number characterizes turbulent flow

is because a high amount of kinetic energy is needed to sustain the generation of eddies, which will be dissipated by viscosity.

The structures that characterize a turbulent flow are eddies. These eddies extract energy from the mean flow. And they will break up into smaller eddies until a scale is achieved where viscous dissipation is effective. These phenomena will be explained in the following sections.

Turbulent premixed flames

Turbulent premixed flames are characterized by a series of dimensionless numbers. The most relevant of these is the Karlovitz number. This number relates the time scale of the chemical reaction and the time scale of turbulence.

In the Figure 2.3 you can see the different flames that are identified, as further to the right in the graph the flame is finer than the turbulent force. As higher up in the graph the velocity of the turbulent eddies is faster than the laminar velocity of the flame.

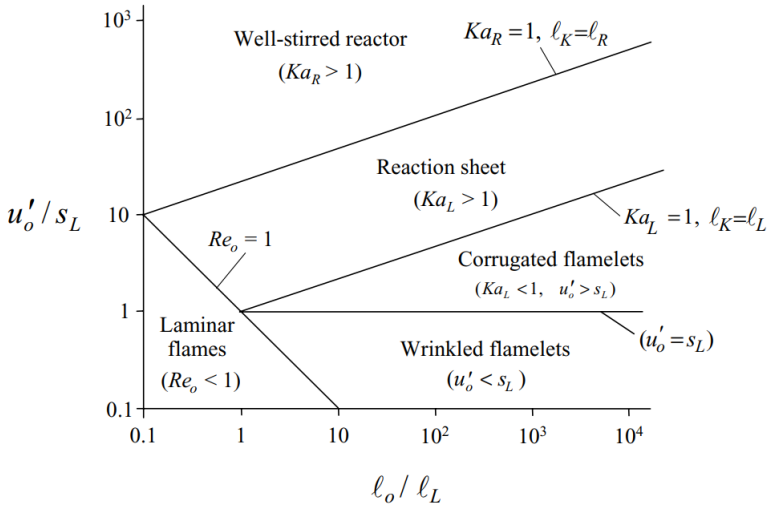

Figure 2.3: Diagram for premixed turbulent combustion. [29]

The turbulent flame velocity will be similar to the laminar burning velocity for premixed flames, although this phenomenon will be much more complex and less defined.

In the laminar case, the burning rate is a function of the diffusive-reactive properties of the mixture. In the turbulent case, this velocity also depends on the turbulent characteristics of the flow and its coupling with the subsequent combustion processes that occur within the flame.

Turbulent non-premixed flames

The fundamental description of turbulent non-premixed flames relies on the characteristic time and length scales, even though a non-premixed flame lacks a propagation velocity, making it challenging to pinpoint a suitable characteristic time scale.

The zone of preheating of these flames is determined solely by the convective-diffusive transport that causes the turbulent flow.

The determining parameter in this type of flame is the Dahmkoler number, which relates the characteristic time scale for transport to the characteristic time scale of the chemical reaction. This

number will represent the relative chemical strength of the flame.

In a turbulent flow, the Kolmogorov scale is expected to have the shortest turnover time and to have the most effective transport in the preheat zone. That is why the scale of transport in turbulent non-premixed flames will be the Kolmogorov scale.

The behaviour of these flames can be seen in the following diagram. To the right of the diagram the turbulence is more intense and towards the top the chemistry is faster.

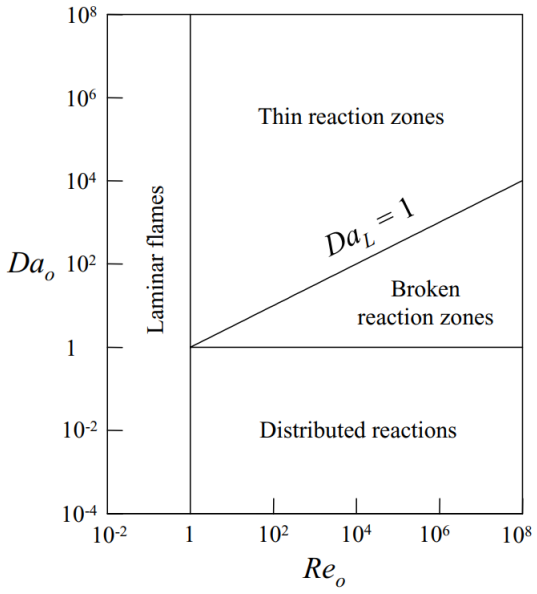

Figure 2.4: Turbulent non premixed flames. [29]

2.3 Swirling flows in combustion

Gas turbine combustors often use vortices to enhance the mixing of fuel and oxidant. The swirling motion can stabilize the flame to a certain point. With this type of flow recirculation zones usually appear. If the vortex intensity is very high, there is a strong interaction between the flame and the wall, possibly causing the flame to extinguish.

Turbulence intensity can be increased by swirl flows, which break up into small turbulent eddies. This increases the speed of the turbulent flame and accelerates the burning speed. In this section, the properties of this type of flow are investigated based on available experimental and numerical studies.

Turbulence improves the mixing of reactants and stabilizes the flame. Downstream of the swirler, a recirculation appears, where backflow mixes the hot product gases with the incoming fresh reactant stream. This results in a high and uniform combustion zone temperature. The energy required to ignite the unburned gases and stabilize the flame is supplied by this hot mixture. In non-premixed conditions, fuel is injected into the shear and recirculation regions formed near the zero-streamline boundary, providing low-velocity regions for flame stabilization and high temperatures from the flame.

Precession Vortex Core (PVC) is one phenomenon that occurs in swirling flows. This phenomenon is explained in the next section. It is clear that this type of flow offers many advantages, such as the ability to stabilize the flame and improve mixing with eddy fractures.

2.3.1 Vortex breakdown in a confined burner

As mentioned earlier, creating a recirculation zone is critical to flame stability and is achieved through the use of swirling flow. The formation of the recirculation zone is primarily affected by the pressure gradient and distribution within the combustor. As the flow passes through the vanes, it creates a tangential velocity component that creates a centrifugal force that moves out of the combustor. This force creates an equilibrium radial pressure gradient, also known as equilibrium simple radial flow.

Vortex breakdown is an important flow characteristic of swirl injectors and is often characterized by a sudden change in the thin vortex core that develops into a downstream recirculating bubble or spiral pattern. Eddy breakdown flow regions are responsible for the primary flame stabilization mechanism and are identified by the presence of internal stagnation points and backflow. Considerable effort has been expended to understand eddy collapse, but no theory can fully and accurately explain all its features.

Many authors have studied the recirculation zones in a flow with the characteristics that have been previously explained. It seems that at least three zones are clearly identified:

- Central Toroidal Recirculation Zone (CTRZ), is the main zone that recirculates upstream to the nozzle exit and is responsible for igniting the injected fresh reactants.
- Wake Recirculation Zone (WRZ): is the separation zone of the bluff body. ´
- Corner Recirculation Zone (CRZ): zone at the corner due to wall confinement.

These zones are easily observed in the Figure 2.5.

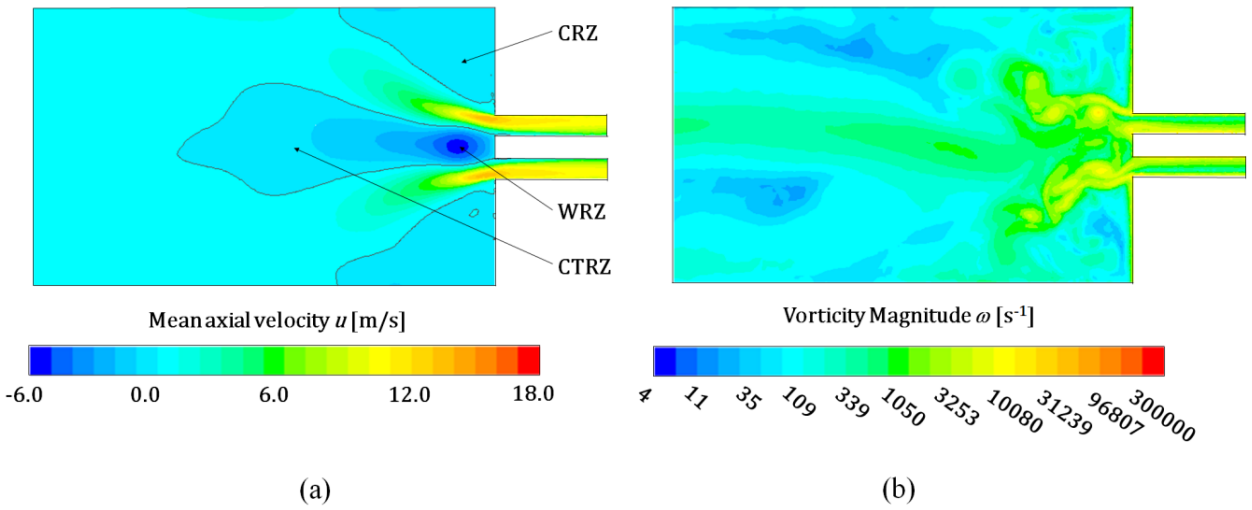

Figure 2.5: (a) Mean axial velocity, u, with identification of Wake Recirculation Zone (WRZ), Corner Recirculation Zone (CRZ) and Toroidal Recirculation Zone (CTRZ) and the zero axial velocity isolines in the longitudinal plane of the burner; (b) Vorticity magnitude contours. [46]

An unstable asymmetric flow structure called a precessing vortex core (PVC) frequently manifests in turbulent swirl combustion devices (Figure 2.6). PVC, which is typically connected to vortex breakdown and the associated recirculation zone in high Reynolds number flows, takes place when

a central vortex core precesses around the axis of symmetry at a particular frequency. Although the presence of a PVC improves turbulence intensity and mixing in combustion systems, it can also result in resonant coupling with low-frequency acoustic oscillation in gas turbine combustors.

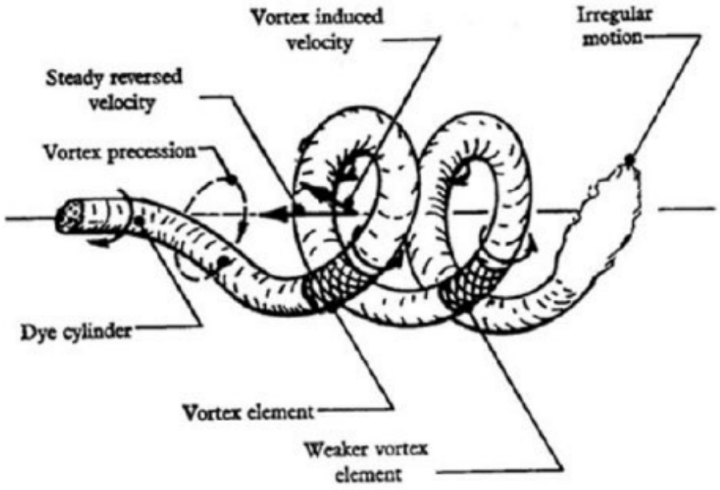

Figure 2.6: Representation of the helical structure of PVC. [9]

The initiation of PVC is influenced by several factors, including:

- Swirl number.
- The existence of a Central Recirculation Zone (vortex breakdown, reverse flow, and PVC manifest above a certain swirl number threshold).
- Fuel injection method.
- Combustor design.
- Equivalence ratio.

Boushaki et al.[6] investigated turbulent flames on a swirl burner with radial fuel injection. This burner is formed of two concentric tubes with a swirler (shown in Figure 2.7).

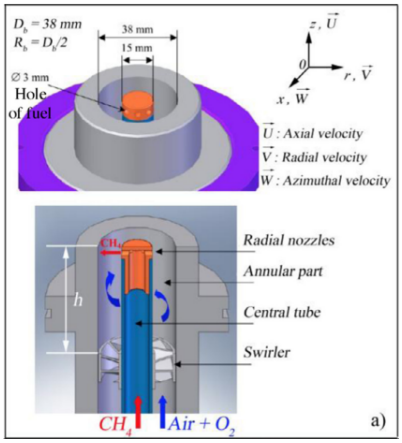

Figure 2.7: Burner configuration. [6]

Experimental and numerical investigations were performed on this burner, and the results showed that the use of high swirl intensity leads to the appearance of an Internal Recirculation Zone (IRZ) for both reacting and non-reacting conditions (Figure 2.8), which is mainly the same as the CTRZ. The IRZ expands with combustion due to changes in fluid density and is more intense in the reacting case than in the non-reacting case.

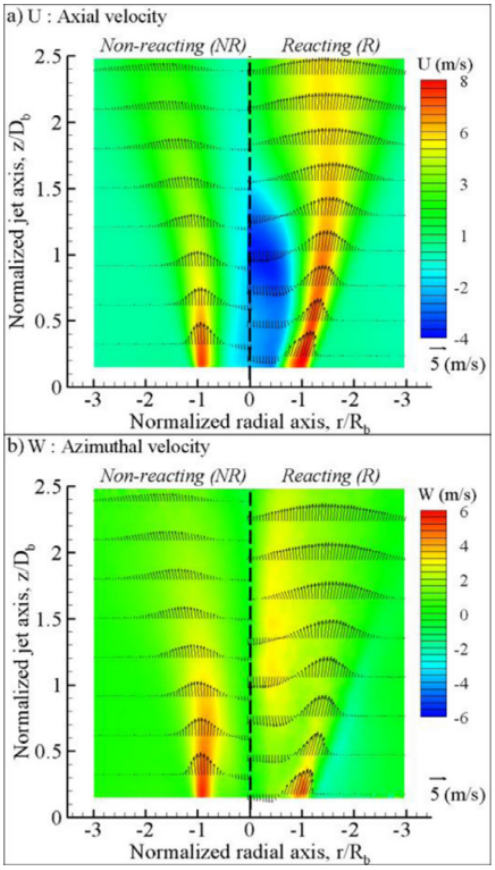

Figure 2.8: Fields of axial and azimutal velocities under-reacting and non-reacting conditions. [6]

2.3.2 Swirl for reduction of pollutant emissions

Swirling in non-premixed combustion can help to reduce pollutant emissions such as nitrogen oxides. The swirl effect improves reactant mixing while also lowering flame temperature and NOx emissions. However, a swirl intensity that achieves a balance between lowering pollutant emissions and preventing flashback is required. Boushaki et al. [6] and Nazim et al. [38] reported that increasing the swirl number tends to reduce the EINOx formation, particularly for oxygen rates up to 27% (Figure 2.9). This is because swirling causes a decrease in flame temperature via the Zeldovich mechanism. The swirl intensity may also improve mixing and lengthen the residence time within the reaction zone, promoting CO to CO_2 conversion.

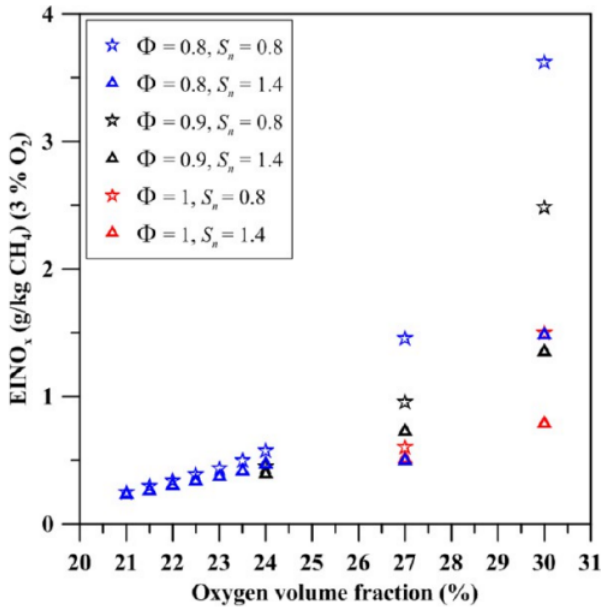

Figure 2.9: Variation of EINOx versus O_2 addition for equivalence ratios of 0.8, 0.9, and 1 and swirl numbers (S) of 0.8 and 1.4. [38]

2.3.3 Swirl characterization

Swirling flows are typical anisotropic turbulent flows. They can be described as the combination of an axial velocity component and a vortex flow component. They are frequently treated as axisymmetric since the dominant velocity components primarily align along the radial and axial directions. However, it's important to acknowledge that this assumption may not always be valid.

The velocity components of the swirling flows can be characterised by a cylindrical coordinate system. Velocity components are represented as the sum of mean and fluctuating velocity as can be seen in the Figure 2.10. Previous investigations on swirl flows have shown that the radial component of velocity is generally much smaller than the axial and tangential components.

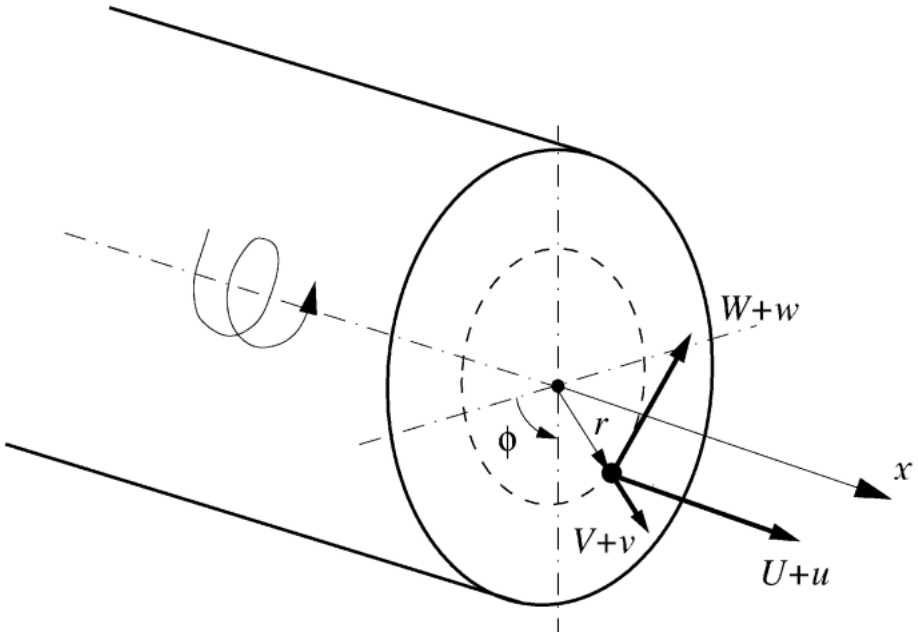

Figure 2.10: Cylindrical coordinate system for the swirling flow and their corresponding velocities. [30]

The swirl number is a dimensionless number that is used to characterize the rotating flows. It is proposed by (Beér and Chigier). The swirl number is the ratio of angular and linear momentum.

$$S = \frac{G_{tg}}{RG_{ax}} \tag{2.1}$$

Where G_{tg} is the axial flux of tangential momentum, G_{ax} is the axial flux of axial momentum, and R is the outer radius of the annulus. This number can be calculated through the momentum definition, in this case, it is necessary to know the velocity and pressure distribution on cross sections of the flow. It can also be calculated geometrically.

$$S = \frac{\int_0^R r^2 UW\, dr}{\int_0^R rU^2 W\, dr} \tag{2.2}$$

Other authors (Cantrak) use the swirl intensity as a measure of the amount of swirl.

$$\theta = \frac{\int_0^R rW^2 U\, dr}{\int_0^R rU^3\, dr} \tag{2.3}$$

Both expressions are characteristic of the flow, and two different flows can have the same swirl numbers. The different swirl number formulations make clear the great effort that has been made in order to define this number. Despite the formulation used, there is a set of assumptions that are necessary to calculate this number. For example, the high Reynolds number is a hypothesis widely used that is suitable in the case of combustors.

2.4 Combustion chemical reactions

Combustion is a chemical reaction in which there is an oxidizing agent and a reducing agent.

Today, there are a number of levels around combustion that researchers are working on. These are:

1. Quantum mechanics and direct measurements of the kinetic constants of the rates and the intermediate reactions and products. In this step, the thermochemical parameters and the reaction constants required for analyzing the chemical reactions are calculated accurately.

2. Fuel structure. The species and reactions are combined into detailed chemical mechanisms that are validated through experiments.

3. CFD studies with reduced chemistry. The previous mechanisms are reduced trying to preserve the target features which can be, for example, the ignition time or the flame speed, among others.

4. Practical applications.

A chemical reaction is the result of many chemical processes. The reaction mechanism is a sequence of intermediate steps that occur on a molecular scale. Each of these intermediate steps is called an elementary stage. In these stages, the species that appear are neither reactants nor products and therefore are not in the chemical reaction. These species are the reaction intermediates, whose life is very short as they are highly reactive species that are consumed in the following stages.

A kinetic chemical mechanism represents this since it contains a list of all the species with their thermodynamic parameters and the elementary reactions with their respective rate constants.

A chemical kinetic mechanism needs a numerical model to represent practical devices such as shock tubes, jet-stirred reactors, etc. Software that is commonly used to simulate these chemical systems are CHEMKIN, Cantera, OPENSMOKE, FlameMaster, among others.

A well-validated combustion model will be one that can represent the oxidation of a fuel for a wide range of physical conditions and mixture compositions, temperatures, and pressures. Therefore, one of the most important steps when developing a chemical model is to have enough data to validate the model.

To demonstrate the dimension of this problem, it is enough to say that the oxidation of hydrogen requires approximately 30 elementary reactions. For the oxidation of methane, which is an even more complex mechanism, around 30 species and 200 elementary reactions are necessary. As can be deduced, the computational cost of detailed mechanisms is very high, so it is not surprising that various methods are used to reduce them. There are mechanisms with fewer than 10 species that work well for a qualitative analysis of a methane flame. Although the mechanisms around 20 species are the ones that usually work best for small hydrocarbons. Simulations of many practical systems, particularly liquid-fueled engines, need to use larger hydrocarbons such as n-heptane.

A detailed mechanism that has been used extensively for n-heptane and has been validated for low ignition temperatures and stirred reactor consists of 561 species and 2539 reactions. There are other mechanisms with good precision and smaller ones that still consist of more than 100 species, which supposes a great computational cost.

There are several ways to reduce the detailed mechanisms. Among them, is the skeleton reduction, which eliminates from the mechanism the species and reactions that are not important. This is done with algorithms that are capable of identifying species that are highly coupled to the main species, such as fuel.

Many times the reduction of the skeleton can be the previous step to a reduced mechanism. The strategies to follow are diverse. For example, for large hydrocarbons Isomer lumping can be used. Large hydrocarbons have a number of isomers, which are important at low ignition temperatures. These isomers can be grouped since they have the same molecular weight and similar thermodynamic and transport properties, so their transport equations can be combined. Another reduction mechanism is the time scale reduction with Quasy Steady State Assumption (QSSA). With this mechanism, it is considered that species that are depleted quickly reach a steady state after a transient period.

2.5 Computational fluid dynamics (CFD)

2.5.1 Turbulent flow

Turbulent flows are chaotic flows that are basically characterized by an irregular and chaotic movement, which makes them unpredictable. Some of the principal characteristics of turbulent flows are recirculation, eddies and randomness. Turbulence, although it can be accompanied by many positive aspects in the world of engineering, is also complicated to study, which makes the difficulty of analyzing a turbulent flow high. CFD is one of the tools used in the industry to analyze these types of flows. Some of the principal characteristics of a turbulent flow are:

- High velocities and lower viscosities.
- The Reynolds number is a dimensionless number that relates the viscous and inertial forces of a fluid. It serves to determine if the fluid will have a laminar and turbulent behaviour. Generally, when the Reynolds number is greater than 3500, it is considered a fluid in a turbulent regime.
$$Re = \frac{\rho U L}{\mu} \tag{2.4}$$
- Irregular flow, this is why turbulent flows are treated statistically.
- Diffusivity, this is the characteristic responsible for better mixing, which means that the rates of mass, momentum and energy transports are increased.
- Rotationality. Turbulent flows are characterized by vortex generation which is a strong three-dimensional structure.

Energy cascade and turbulent scales

Turbulent flows are characterized by a spectrum of eddies. There are different scales that can be identified in a turbulent flow.

Turbulent flows exist because the mean flow is forced into a condition where the instability develops. These instabilities give energy to those eddies whose characteristic size is the greatest, set by the dimension of the device. These eddies become turbulent and show considerable variability even at much smaller scales. This event is described as an energy cascade (Figure 2.11).

For turbulent flows with high Reynolds numbers, there exists an energy transfer rate independent of molecular viscosity. This is called a cascade because vortices are transformed and folded by others.

This means that bigger eddies transfer their energy into small eddies at a rate of energy transfer that can be calculated. The energy will be transferred until the smallest size in which viscous dissipation dominates. This smallest range is the Kolmogorov scale.

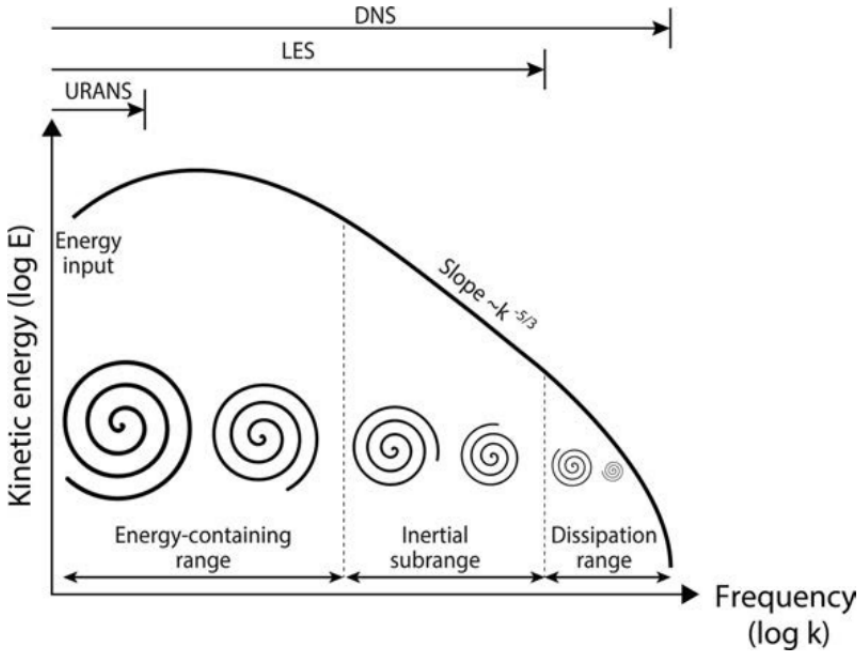

Figure 2.11: Turbulent energy cascade. [15]

Turbulent structures are characterized by time and length (or velocity) scales that vary with eddy size. The largest vortices in the shear layer or casing increase in size until they fill the entire layer or flow domain. Therefore, the characteristic length scale L is clearly determined by the flow's characteristic dimension and is limited only by the physical boundaries of the flow. These eddies are not the most energetic ones and play a significant role in transporting momentum, heat, and substances. Because of this, they are referred to as the "diffusion length scale".

The 'energy vortex', characterized by a slightly smaller size compared to its predecessor, is the most efficient structure for extracting energy from mean motion but also plays an active role in the energy cascade to smaller scales. The time and length of this scale are associated with k (Turbulent kinetic energy) and ϵ (Dissipation rate of turbulent kinetic energy).

$$\tau = \frac{k}{\epsilon}[s] \quad l = \frac{k^{3/2}}{\epsilon}[m] \quad Re_\tau = \frac{k^{1/2}l}{\upsilon} \tag{2.5}$$

The actual dissipation of kinetic energy into heat takes place in the finest vortex structures corresponding to the "dissipation (Kolmogorov) scale". When a dimensional analysis is done the Kolmogorov time length and velocity can be determined.

$$\tau_\eta = \left(\frac{\nu}{\epsilon}\right)^{1/2}[s] \quad l_\eta = \left(\frac{\nu^3}{\epsilon}\right)^{1/4}[m] \quad Re_K = \left(\frac{\eta}{\theta}\right)\frac{\eta}{\nu} = 1 \tag{2.6}$$

An important idea that must be mentioned is that in the turbulence there is an energy conservation which means that the rate of energy dissipation in the Kolmogorov eddy is the rate of energy transfer in the inertial subrange (ϵ).

Turbulent kinetic energy

Turbulent dynamics can be qualitatively expressed as the turbulent kinetic energy dynamics defined as the average kinetic energy per unit mass in a fluctuating velocity field.

$$k = \frac{1}{2}\overline{u_i u_i} = \frac{1}{2}\left(\overline{u_1^2 + u_2^2 + u_3^2}\right) \tag{2.7}$$

The turbulent kinetic energy is half the trace of the Reynolds stress tensor.

As has been said, the generation mechanism is the extraction of energy from the mean flow and subsequent transfer to the maximum turbulence scale. The failure mechanism is the dissipation of kinetic energy into heat, and as observed previously, this only occurs when the turbulence scale is small enough.

Turbulence energy spectrum

The turbulence energy spectrum is the one-point turbulent kinetic energy and is another definition needed to understand turbulent flows.

$$\int_0^\infty E(\kappa)d\kappa = \frac{1}{2}\overline{u_i u_i} = k \tag{2.8}$$

As has been said in the figure, there are different spectral regions and scales in turbulence.

Low-frequency ranges characterized by small wavenumbers contain large eddies that "remember" their origin and maintain an imposed orientation.

Then, for intermediate wavenumbers, the corresponding structure is the most energetic eddy, which is nearly isotropic and independent of kinematic viscosity (if Re is large enough). The **"inertial subregion"** is characterized by small, isotropic vortices. The energy cascade process still depends only on the turbulent kinetic energy k and the dissipation rate (if Re is large enough).

Finally, beyond the wavenumber threshold, a small dissipative scale appears and this region is still characterized by isotropy. This scale is called the **Kolmogorov scale**.

The distribution of the cascade, when the necessary data is collected, presents a universal behaviour at high wavenumbers. That is why in logarithmic scale is possible to see and slope of -5/3 (Figure 2.12).

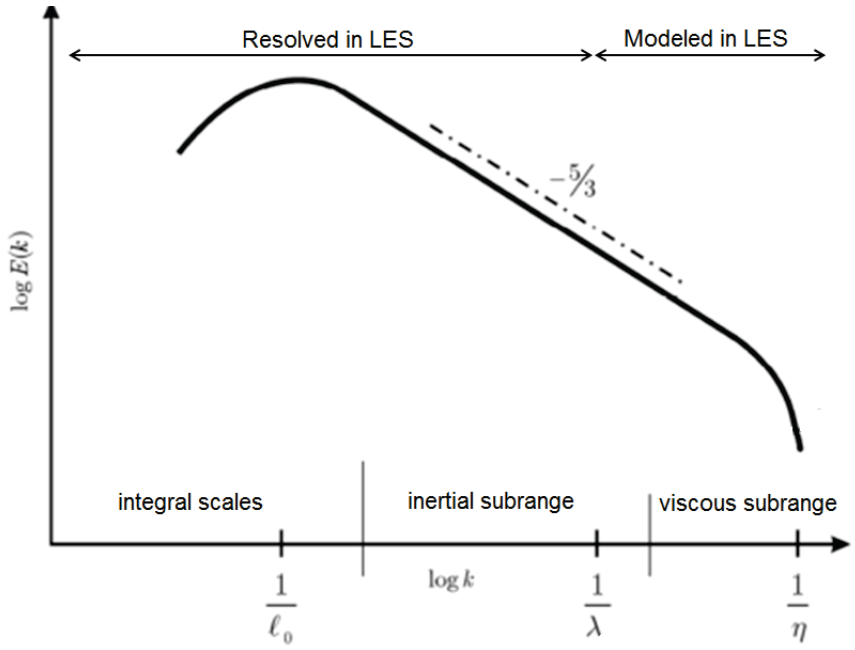

Figure 2.12: Energy cascade of turbulent kinetic energy (logarithmic scale). [22]

From a practical point of view, the Direct Numerical Simulation (DNS) approach solves all spectrum areas. Large Eddy Simulation (LES) is resolved down to the inertial subdomain, allowing to reconstruct only part of the discontinuities that characterize the flow under consideration. Instead, RANS does not resolve any part of the spectrum.

2.5.2 RANS approach

As previously explained, there are different approaches in CFD to solve the equations that characterize the flow.

Direct Numerical Simulation (DNS) is performed when directly solving the Navier-Stokes equations. For DNS to perform correctly, it must cover the full range, starting with the smallest turbulence scale (Kolmogorov) until the integral scale. With current technology, DNS can only run for very few problems, minor ones. However, this solution helps to understand different phenomena and generate simplified models that can be used with less computational cost.

The Navier-Stokes equations can be filtered to discard the minimum wavelength. Finally, most of the energy comes from integral upscaling. The solution of the filtered Navier-Stokes equation is called **Large Eddy Simulation (LES)** because the maximum scale of turbulence is solved. The computational complexity of LES is much less than the DNS because the size of the smallest cell can be orders of magnitude larger. Since the minimum scale behaviour seems to be universal, this range can be modelled since its information is not irrelevant.

Modelling all scales of turbulence without solving can reduce the amount of computation associated with LES. The resulting equation is called the **Reynolds-averaged Navier-Stokes equation (RANS)**. For non-stationary, a "U" is usually added at the beginning to indicate "non-stationary".

The Reynolds Averaged Navier Stokes (RANS) equations, are a simplified form of the Navier Stokes equations, which are one of the most important and complex equations in the physical world. In the RANS equations, the steady state solution is decoupled or separated for the unsteady

or fluctuating one. This technique is called Reynolds decomposition. Reynolds decomposition will express a property as the sum of a mean and fluctuating part.

$$\hat{\Phi} = \bar{\Phi} + \phi' \tag{2.9}$$

A general quantity average can be calculated as a time average for the statistically stable state of turbulence.

$$\bar{\hat{\Phi}} = \lim_{\tau\to\infty} \frac{1}{\tau} \int_0^\tau \hat{\Phi}(x_i, t)dt \quad \bar{\phi'} = \lim_{\tau\to\infty} \frac{1}{\tau} \int_0^\tau \hat{\phi'}(x_i, t)dt \tag{2.10}$$

The mean can be computed as the ensemble mean. This ensemble averaging is possible when the temporal scale is comparable to the turbulent structures.

$$\bar{\Phi} = \lim_{n_e\to\infty} \frac{1}{n_e} \sum_{j=1}^{n_e} \hat{\Phi}^j(x_i, t) \tag{2.11}$$

A direct result of this decomposition is that there are twice as many unknowns to solve, so additional equations are used that are based on modelling the random component from turbulence. In order to obtain the equations used in the RANS method the Reynolds decomposition must be applied to the conservation equation of a generic variable. When operating and considering incompressible flow ($\rho' = 0$), the Reynolds averaged momentum equation for a Newtonian fluid is the following.

$$\bar{\rho}\frac{D\bar{U}_i}{Dt} = \bar{\rho}g_i - \frac{\partial \bar{P}}{\partial x_i} + \frac{\partial}{\partial x_j}\left[\mu\left(\frac{\partial \bar{U}_i}{\partial x_j} + \frac{\partial \bar{U}_j}{\partial x_i} - \frac{2}{3}\frac{\partial \bar{u}_k}{\partial x_k}\delta_{ij}\right) - \bar{\rho}\overline{u_i' u_j'}\right] \tag{2.12}$$

Where $\overline{u_i' u_j'}$ is the turbulent stress tensor.

The following problem that has to be faced is to solve or compute the Reynolds stress tensor, also known as **clousure problem**. There are two main categories for finding the Reynolds stress tensor: the turbulent viscosity hypothesis and the Reynolds stress equation model.

"First Order Closure" (or "Eddy Viscosity Model"): The eddy viscosity model assumes that the turbulence (momentum, heat, species) is associated with the mean flow field and therefore is resolved within the flow field using variables. This method saves computing time by not introducing a specific transport equation for the second moment. These models can be divided into linear and nonlinear eddy viscosity models. Linear viscosity models use the Boussinesq hypothesis. The Boussinesq approximation states that the density variation is significant only in the lift term and can be neglected in the rest of the equation.

$$\tau_{ij}^t = -\frac{2}{3}\rho k\delta_{ij} + \mu_t\left(\frac{\partial \bar{U}_i}{\partial x_j} + \frac{\partial \bar{U}_j}{\partial x_i} - \frac{2}{3}\frac{\partial \bar{u}_k}{\partial x_k}\delta_{ij}\right) \tag{2.13}$$

According to Boussinesq's definition, the turbulent viscosity scalar field μ_t is included in the equation, which increases the molecular viscosity. This field will have to be modelled using first-order closure models that are developed from the Boussinesq hypothesis. The different approaches are the following:

- Algebraic models or zero equations. Turbulent viscosity is a function of a characteristic length and the average velocity of the flow.

- Models of one equation. There is an additional transport equation that is solved to obtain the turbulent viscosity.
- Two equation models. Two more differential equations are solved to obtain the turbulent kinetic energy and the spatial integral scale.

"Second Order Closure" (or "Second Moment Closure" or "Reynolds Stress Modeling"): This model solves all tensor components, which is why it adds seven additional equations. As one can imagine, this complicates the calculations but allows better solutions for flows with large mean curvatures, rotations, or very fast deviations from the mean flow.

2.5.3 High-Reynolds Number Linear Eddy Viscosity Models

$k-\epsilon$ Model

This method solves two additional transport equations. The variables transported are the turbulent kinetic energy (k) and the turbulent dissipation rate (ϵ). This model assumes a turbulent viscosity to be isotropic and that the mixing length is: $l_m = k^{3/2}/\epsilon$. The additional equations for the model require several fit constants that are selected empirically and are usually valid for a wide range of flows. This model is a simple model that applies in many cases. However, it is a model that does not adequately represent boundary layer problems with large detrimental pressure gradients, and highly rotational flow.

It is a semi-empirical model, since the turbulent kinetic energy is obtained from a rigorous development of equations but the turbulent dissipation is approximated empirically.

The equations used for these two variables are as follows.

$$\frac{Dk}{Dt} = \frac{\partial k}{\partial t} + U_j \frac{\partial k}{\partial x_j} = \frac{\partial}{\partial x_j}\left[\left(\upsilon + \frac{\upsilon_t}{\sigma_k}\right)\right] + P + G - \epsilon \tag{2.14}$$

$$\frac{D\epsilon}{Dt} = \frac{\partial}{\partial x_k}\left[\left(\upsilon + \frac{\upsilon_t}{\sigma_\epsilon}\frac{\partial \epsilon}{\partial x_j}\right)\right] + \left(C_{\epsilon 1}P + C_{\epsilon 3}G\right)\frac{\epsilon}{k} - C_{\epsilon 2}\frac{\epsilon^2}{k} \tag{2.15}$$

$$\upsilon_t = C_\mu \frac{k^2}{\epsilon} \quad P = \upsilon_t \left(\frac{\partial U_i}{\partial x_j} + \frac{\partial U_j}{\partial x_i}\right)\frac{\partial U_i}{\partial x_j} \tag{2.16}$$

The coefficients are obtained through the experimental method or DNS data (semi-empirical).

RNG $k-\epsilon$ Model

Yakhot et al developed a method to renormalise the Navier-Stokes equation with a Re-Normalisation Group (RNG). With this method, smaller scales of motion are taken into account. The main difference of the model is that the numerical constants of $k-\epsilon$ are obtained from the renormalization group theory. This model has been supplemented with scale expansions in most of the software, including the one used in OpenFOAM.

With the implementation of this model in OpenFOAM, an additional parameter is taken into account, which is the additional expansion parameter (η) that represents the ratio of the turbulent to mean strain time cycle. This is a dimensionless tensor which is equal to zero in isotropic turbulence. This expansion parameter is not reflected in the functional form of the standard $k-\epsilon$ model, this

will only be of importance with large values of η. Unfortunately, in many applications this number is considerable.

$$\eta = S\frac{k}{\epsilon} \tag{2.17}$$

$$S = (2S_{ij}S_{ij})^{1/2} \tag{2.18}$$

Where the mean strain S_{ij} is defined as $S_{ij} = \frac{1}{2}\left(\frac{\partial U_i}{\partial x_j} + \frac{\partial U_j}{\partial x_i}\right)$

Whit this values the $C_{\epsilon 2}$ constant is recalculated as follows.

$$C_{2\epsilon}^{*} = C_{2\epsilon} + \frac{C_\mu \eta^3(1-\eta/\eta_0)}{1+\beta\eta^3} \tag{2.19}$$

β is a factor derived from experiment. The OpenFoam model already has this coefficients set in the default model.

The main difference found with this model with respect to the standard is that in the standard model the eddy viscosity is calculated from only one turbulent scale, so this diffusion is calculated only for that scale. In reality, all moving scales contribute to turbulent diffusion. With this approach, the ϵ equation tries to take into account other different scales through changes in the production term.

$k-\omega$ Model

This model, similar to the $k-\epsilon$, uses the specific turbulent dissipation ($\frac{\epsilon}{k}$) as the second transport equation. This model is more accurate for regions close to walls but tends to be worse at modeling free-flow zones.

$$\frac{D}{Dt}\left(\omega = \frac{\epsilon}{k}\right) \rightarrow \frac{D\omega}{Dt} = \frac{1}{k}\frac{D\epsilon}{Dt} - \frac{\epsilon}{k^2}\frac{Dk}{Dt} \tag{2.20}$$

$k-\omega$ SST (Shear Stress Transport) Model

It is a hybrid between the models explained above, this is common to use the best of both and have a more accurate modelling. This model uses a $k-\omega$ in the inner zones of the boundary layer and transitions to a $k-\epsilon$ model far from the walls.

2.5.4 Turbulent boundary layers

Turbulence is greatly affected by the presence of boundaries. As is known, in a solid boundary the boundary condition will be that the speed of the fluid is zero. In this case, both the average and the pulsating velocity will be zero as well. The Reynolds tensor will also be null which does not happen far from the wall, in free flow where normally the value of the tensor is large. The only remaining tensor is the viscosity tensor. Wall flow is more complicated than free flow since viscosity starts to be an important phenomenon, which introduces a new problem. There will be three main regions in the boundary layer that are somewhat analogous to the turbulent scales discussed above.

- Viscous sublayer. It is the closest sublayer to the wall, it extends up to the distance in which the Reynolds number takes the value of unity. Friction is important.
- Inertial sublayer. It is the next sublayer, where the viscosity is not taken into account. It is a section analogous to the inertial range, where the flow is dominated neither by turbulent

viscosity nor by turbulent kinetic energy. It serves as a separation between the two layers.

- Turbulent boundary layer. This layer is dominated by the size of the eddies, known in turbulence as the inertial scale. From this distance, it can be assumed that the flow no longer has any dependency on the boundary layer.
- Free fluid. This is the region in which the flow is not turbulent and is irrotational.

To quantify all of the above, it has been shown that the boundary layers have a similarity property, thus the normalized velocity can be related to the distance.

$$\frac{U}{u} = f\left(\frac{y}{L}\right) \tag{2.21}$$

The characteristic speeds and lengths can be derived as follows:

$$\mathtt{U} = \sqrt{\frac{\tau_w}{\rho}} = U_\tau \quad \mathtt{L} = \nu\sqrt{\frac{\rho}{\tau_w}} = \frac{\nu}{U_\tau} \tag{2.22}$$

Which are called the friction velocity and viscous length. The similarity relation can also be found in dimensionless form.

$$\frac{U}{U_\tau} = f\left(\frac{yU_\tau}{\nu}\right) \rightarrow U^+ = f(y^+) \tag{2.23}$$

To be able to calculate with wall functions, a certain value of y + is needed, which is only known after running the simulation. Normally an estimate of y + is made, it is meshed with said estimate and then the mesh is calculated and corrected if necessary.

Since the turbulent region, governed by large vortices, is characterized by the lack of dependence of the velocity gradient on molecular viscosity, it is possible to define two boundary layer zones that are calculated as follows.

$$U^+ = y^+ \quad viscous \quad sublayer \quad (y^+ < 5 - 6) \tag{2.24}$$

$$U^+ = \frac{1}{k} ln(y^+) + B \quad logarithmic \quad region \quad (20 - 30 < y^+ < 150 - 200) \tag{2.25}$$

Wall functions

In order to represent what happens with turbulence near the walls, as has been explained before, CFD uses some wall functions. Wall functions are the practical approach of the theory explained before.

Wall functions are empirical equations used to represent what happens near the wall. They are a bridge between this zone and the fully developed flow. When using wall functions, the boundary layer does not have to be solved, which saves computational cost. On the other hand, as they are empirical relations will only be accurate in some conditions.

This approach was proposed in 1972 and relies on the fact that the first cell centre at the wall has to be located in the logarithmic layer, if it is located in the viscous the results will be inaccurate.

Second Moment Closure or Reynolds Stress Modeling

Currently, two-equation models are the most commonly employed models in the field of Computational Fluid Dynamics (CFD). In industrial applications, the second-moment closure method is anticipated to replace these two-equation models. However, despite several decades of development, only a handful of CFD companies provide this option, mainly because the developers of many of these software packages are hesitant to acknowledge the method's superiority, which is still viewed as being in the developmental stages.

Actually, second-moment closure is nothing more than the RANS model but uses a transport equation for each component of the Reynolds tensor. Since these equations contain high-order correlations that give rise to new terms, new equations to the Navier Stokes system will be necessary, and the computational cost is higher. Examples of this approach can be seen in the following equations.

$$\frac{DU_i}{Dt} = -\frac{\partial}{\partial x_j}(\overline{u_i u_j}) + ... \tag{2.26}$$

$$\frac{D\overline{u_i u_j}}{Dt} = -\frac{\partial}{\partial x_k}(\overline{u_i u_j u_k}) + ... \tag{2.27}$$

$$\frac{D\overline{u_i u_j u_k}}{Dt} = -\frac{\partial}{\partial x_l}(\overline{u_i u_j u_k u_l}) + ... \tag{2.28}$$

About the boundary layer, standard wall functions with second-moment closure approach are able to predict with a reasonable accuracy the flow pattern and pressure distribution, with the exception of the vicinity of the separation. This is why this approach can be applied in cases where walls or interfaces are not significant factors.

2.6 Eddy Dissipation Concept (EDC)

The Eddy Dissipation Concept (EDC) is an extension of Magnussen's Eddy Dissipation model. This concept models turbulent mixing method for modeling combustion.

Many of the fuels are fast burning so the rate of reaction is actually controlled by turbulent mixing. In this model, the chemical reaction is governed by large-scale turbulent mixing. It is assumed that combustion occurs within regions where reactants are thoroughly mixed at the molecular level and where turbulence energy dissipation occurs. These regions are often referred to as "fine structures," and their size is approximately on the same scale as the Kolmogorov scales. Therefore this model is a concept for dealing with the interaction between turbulence and flame chemistry.

The EDC relies on a cascade model of energy dissipation, transferring from larger to smaller scales. This enables the characterization of scale relationships using a closure. A control volume is conceptually divided into fine structures and its surrounding environment. Small eddies are treated as a reaction and the reaction rate is calculated from the species mass balance.

Fine structures are those that are responsible for combustion. These structures are defined by residence time τ^*, a length scale L^* and a velocity scale u^*.

It is suggested that the proportion between the mass of areas that possess fine features and the overall mass can be defined as follows:

$$\gamma_\lambda = C_\gamma \left(\frac{\nu\epsilon}{k^2}\right) = C_\lambda Re_T^{-1/4} \tag{2.29}$$

Where C_λ is called the model parameter.

The residence time of the fine structures is calculated with the Kolmogorov time scale:

$$\tau* = C_\tau \tau_\eta = C_\tau \left(\frac{\nu}{\epsilon}\right)^{1/2} \tag{2.30}$$

Where C_τ is also a model constant. Both constants that have been used in the previous equations will provide the degrees of freedom to different versions of EDC models.

In other sources, these degrees of freedom are defined also as $C_{D1} = (3C_\tau)/(2C_\gamma^2)$ and $C_{D2} = 3C_\tau^2$. The chemical production rate of the species ($\tilde{\omega}_j$) is one of the unclosed factors in the chemical species conservation equation for turbulent reacting flows. The EDC model formulates the mean production rate as follows:

$$\tilde{\dot{\omega}}_j = g(\gamma_\lambda, \chi)\bar{\rho}\frac{\tilde{Y}_j^* - \tilde{Y}_j}{\tau^*} \tag{2.31}$$

After a time-lapse(τ^*) under Perfectly Stirred Reactor (PSR) circumstances, ($\tilde{Y}_j^*$) signifies the Favre-averaged mass fraction of the jth species.

The most general formulation for the $g(\gamma_\lambda, \chi)$ factor is the following one:

$$g(\gamma_\lambda, \chi) = \frac{\gamma_\lambda^n \chi}{1 - \gamma_\lambda^m \chi} \tag{2.32}$$

The exponents n and m will have different values according to different versions of the EDC. But what is evident is that the important factors for this factor are the fine structures length fraction (γ_λ) and the reactivity factor (χ) which accounts for the fraction of structures that are effectively reacting.

In summary, the Eddy Dissipation Concept is an important tool in combustion modelling that is based on the idea that turbulence and the dissipation of energy in a flow are fundamental to understanding how components mix and react in a combustion process. This concept is widespread and is used in a wide variety of commercial software.

2.7 Finite Volume Method

The Finite Volume Method (FVM) is a discretization method used to approximate the conservation, or balance, of one or more quantities expressed by a single or system of partial differential equations. In this method, a mesh is necessary and it will represent the domain where the variable exists. The mesh is composed of elements which are called control volumes. The equation of balance will be obtained by integrating each control volume.

A peculiarity of FVM over the finite difference method is that the discretization is performed on the local equilibrium equations rather than the partial differential equations.

The approach is made from the following transport equation.

$$\int_{V_P} \frac{\partial \rho\phi}{\partial t} dV + \int_{V_P} \nabla \cdot (\rho u \phi) dV - \int_{V_P} \nabla \cdot (\rho \Gamma_\phi \nabla_\phi) dV = \int_{V_P} S_\phi(\phi) dV \tag{2.33}$$

From left to right the terms of this equation are temporal, convective, diffusion and source term. The convective term represents the transport due to the velocity or the fluid motion. The diffusive

term is a second-order derivative in space.

This is an equation of second order. In order to have good results, the order of the discretization should be greater than or equal to the order of the equation being discretized. Starting from this equation it is possible to write down the Navier Stokes equation, so this development also applies to Navier Stokes.

It is going to be assumed that the discretization practice is at least second order in space and time, so the variables will be assumed to vary linearly around a point P in space and instant t in time.

The solution space will be divided into a finite number of arbitrary control volumes or cells. The solutions will be sought within each control volume. These cells can take any shape, such as a tetrahedron, hexahedron, prism, and so on. The only requirement is that the elements be convex and the faces that make up the control volume be flat. Also, the volumes inside and the ones are the boundaries are known.

This domain information must be characterized by different vectors. The $\vec{d}$ vector is the one that connects the centroid P of $\vec{V_p}$ and the centroid N of the neighbour cell (control volume Vn).

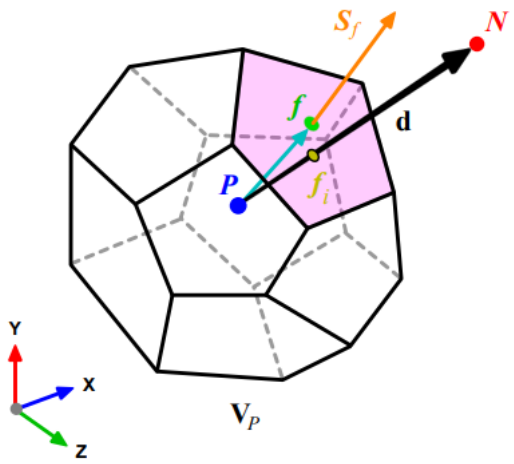

Figure 2.13: Control volume example for the finite volume method. [14]

Finally, it is assumed that the values of all variables are computed and stored in the centroid of the control volume and that they are represented by a piecewise constant profile, the mean value (Equation 2.34).

$$\phi_P = \bar{\phi} = \frac{1}{V_P} \int_{V_P} \phi(x) dV \tag{2.34}$$

The faces are labelled as an f, and where the $\vec{d}$ vector intersects a face it is denoted as f_i. S_f is the face area vector.

Gauss Divergence theorem

The Gauss or Divergence theorem states that the outward flux of a vector field through a closed surface is equal to the volume integral of the divergence over the region inside the surface.

$$\int_V \nabla \cdot a dV = \oint_{\partial V} dS \cdot a \tag{2.35}$$

With this theorem, it will be possible to convert volume integrals of the equation into area integrals.

$$\frac{\partial}{\partial t}\int_{V_P}(\rho\phi)dV + \oint_{\partial V_P} dS\cdot(\rho u\phi) - \oint_{\partial V_P} dS\cdot(\rho\Gamma_\phi\nabla_\phi) = \int_{V_P} S_\phi(\phi)dV \tag{2.36}$$

Now, the problem is to know the values of the variables in the centres of the faces. This can be done by interpolating.

Convective term

The convective term has been converted to convective flux thanks to the Gauss Theorem previously. Now this term can be represented as the sum of the surface integrals over each control surface of the volume in question.

$$\oint_{\partial V_P} dS\cdot(\rho u\phi) = \sum_f S_f\cdot(\overline{\rho u\phi})_f \tag{2.37}$$

Difusive term

The same thing that has been explained previously occurs with the diffusive term that remains as follows.

$$\oint_{\partial V_P} dS\cdot(\rho\Gamma_\phi\nabla_\phi) = \sum_f S_f\cdot(\overline{\rho\Gamma_\phi\nabla_\phi})_f \tag{2.38}$$

Gradient term

Gradients at the cell centroid are approximated by Gauss's theorem.

$$(\nabla\phi)_P = \frac{1}{V_P}\sum_f(S_f\phi_f) \tag{2.39}$$

Source term

The source term is divided into a non-linear part and a constant part. This is an approximation that will only be fully representative of reality if the source term is really constant or linear.

$$\int_{V_P} S_\phi(\phi)dV = S_cV_P + S_pV_P\phi_P \tag{2.40}$$

Finally, the final transport equation that has been developed for the FV method is the following.

$$\int_{V_P}\frac{\partial\rho\phi}{\partial t}dV + \sum_f S_f\cdot(\rho u\phi)_f - \sum_f S_f\cdot(\rho\Gamma_\phi\nabla_\phi)_f = (S_cV_p + S_pV_P\phi_P) \tag{2.41}$$

2.8 Mesh

A mesh is a set of finite volumes in which the problem is discretized. A good mesh is very important for effective computation. Meshes can be divided into two groups structured meshes and unstructured meshes (Figure 3.7).

In a **structured mesh**, the cells are ordered and have regular connectivity. Using the same number of cells and the same network quality, structured grids provide better convergence and higher accuracy than unstructured grids. It takes significant effort to create complex geometries with this type of mesh.

Unstructured meshes are irregular meshes, with connectivity between cells not trivially obtainable as a two-dimensional or three-dimensional array in storage. The associated computational cost is much higher than with structured meshes. 2D triangles and 3D tetrahedrons are commonly used, although other elements with an arbitrary number of faces (polyhedra) can also be used. They are easy to generate automatically.

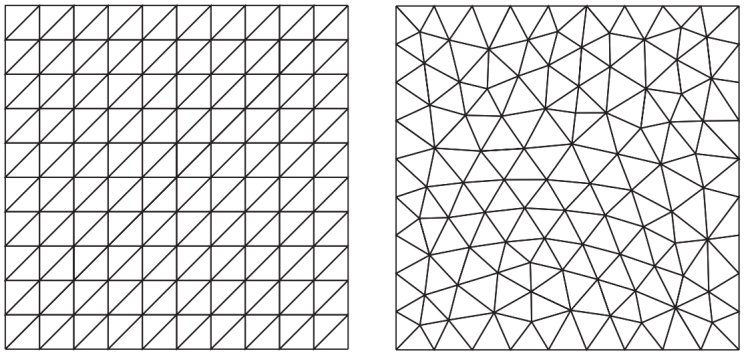

(a) Structured mesh (b) Unstructured mesh

Figure 2.14: Example of a structured triangular mesh and an unstructured triangular mesh in a unit box. [20]

Meshes do not have to be of the same type across domains. The mesh can be created by zones to accomplish a mix of structured and unstructured meshes: **hybrid meshes**. Block meshes can also be created with subdivisions into structured or unstructured meshes. Block meshes can be used to efficiently generate meshes within zones depending on the complexity of the geometry. It can also be used, for example, when some zones of the domain need to deform the mesh or use a mobile mesh.

Maintaining good mesh quality is very important in general. Cell resizing should be smooth which means that the size between adjacent cells should not change by an order of magnitude. Also, cell stretching should not be excessive, unless flow properties permit it.

The cells are not very deformable. There are several ways to measure deflection but they are usually based on the maximum and minimum angles formed by the corners. Depending on the definition used for the deformation parameter (skewness), the corresponding limits are usually higher or lower. High values of the parameter should be avoided (around 0.85 for hexahedral cells). The mesh should be refined in certain regions (boundary layers, shock waves, regions with high gradients of the state vectors). In other areas, it can be coarsened to reduce computational cost.

The fact that a converged solution is obtained does not imply that an exact solution has been obtained. A mesh convergence (or mesh independence) study should be performed to ensure that the size does not affect the solution. The general idea is to use the largest mesh size that solves the problem.

2.8.1 Mesh induced errors

Non-orthogonality and skewness are irregularities of the mesh that are relevant.

An orthogonal arrangement is that the face normal is in the same direction of the direction of the vector connecting the centroids of the two cells, which means that there is an alignment between the d vector and the face-normal vector S.

Skewness happens when the vector d goes through the face centroid.

In the Figure 2.15 it can be seen an example of an orthogonal and skew mesh while in the Figure 2.16 it is shown a non-orthogonal and non-skew example.

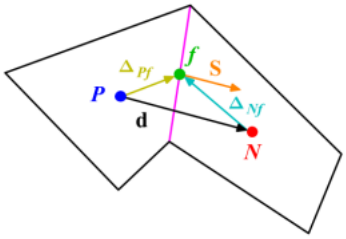

Figure 2.15: Orthogonal and skew mesh. [17]

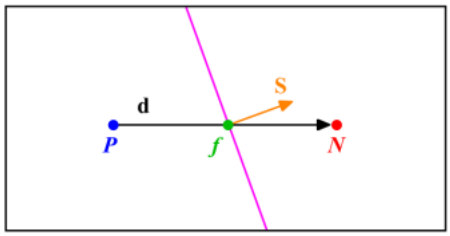

Figure 2.16: Non-orthogonal and non-skew mesh. [17]

The interpolation of the variable and its gradient to the faces centroids depends on equations that are second-order accurate only when the skewness vector Δi is null. The non-orthogonality characteristic also preserves the second-order accuracy when the skewness vector is null. When this does not happen the equations have to be corrected to accomplish the second order accuracy.

2.9 Interpolation schemes

As discussed above, when the mesh is done it is necessary to calculate the property of interest at the center of the cells. There are different methods to perform this calculation, the best known are upwind, linear upwind, CDS and QUICK.

Upwind discretionary methods are used to numerically solve partially hyperbolic differential equations. What these methods do to solve is a strict discretization in the direction that is determined by the sign of the velocity characteristics. The upwind method is first-order, highly stable, and introduces significant numerical diffusion. It can converge faster than other methods due to the damping of disturbances caused by its high diffusivity.

When upwinding, the speed of the interface is checked. If the velocity is going from the first cell to the second, the vector from the first state is used, otherwise, the second one is used. Numerical diffusivity is very high when the convection direction does not align with the principal axes of the cells It can be reduced by refining the grid.

In the **Centered Difference Scheme (CDS)**, the state vector is estimated at the boundary as the average between the values in the adjacent cells. It is a second-order scheme. Therefore,

this scheme uses the information not only from the cell where the flow comes from but also from the neighbouring one to solve the flow. This method is characterized by being limited to the Peclet number, it has to be lower than two, otherwise, it tends to cause divergence. This method is used for LES.

In the **linear upwind** method the speed of the interface is also checked. If the velocity goes from the first cell to the second, the state vector of the first cell and the one upstream of the first cell is used. If it goes from the second to the first, the state vector of the second cell and the one upstream of the second cell is used. It is a second-order method and is generally stable. This method generates numerical dispersion and more information is needed than in the other methods.

The **Quadratic Upstream Interpolation for Convective Kinematics (QUICK)** method performs a squared interpolation to obtain the state vector at the front between cells. For the adjustment of the parabola, the points are moved in the direction from which the transport occurs (upwinding). This is a less extended third order than the tight one. It is a third-order scheme.

2.10 Temporal discretization

The main methods of solving the Euler and Navier-Stokes equations are based on space and time-independent resolution schemes. This approximation offers great flexibility because different approximation levels can be chosen for both convective and viscous flows.

The idea is to evaluate in time the semi-discrete transport equation.

$$\int_t^{t+\Delta t}\left[\left(\frac{\partial \rho\phi}{\partial t}\right)_P+\sum_f \vec{S}_f\cdot(\overline{\rho\vec{u}\phi})_f\right]dt=\int_t^{t+\Delta t}\left[(S_cV_P+S_PV_P\phi_P)+\sum_f \vec{S}_f\cdot(\overline{\rho L\nabla\phi}_f)\right] \quad (2.42)$$

There are multiple discretization schemes, for example, Euler and Crank-Nicolson.

The integrators used are **implicit integrators**, which use information that depends on the future. Implicit methods are more expensive, since their error is proportional to the time step that is why small steps are needed. These integrators are widely used to solve equations.

The **implicit Euler** time scheme will be used with the URANS analysis. This is a first-order accurate scheme. To show how this method works it will be analyzed the following first order ordinary differential equation:

$$\frac{d\phi(t)}{dt}=f(t,\phi(t)) \quad \phi(t_0)=\phi^0 \quad (2.43)$$

The simplest way to obtain the solution at a generic time (t_{n+1}) is:

$$\int_{t_n}^{t_{n+1}}\frac{d\phi}{dt}dt=\phi^{n+1}-\phi^n=\int_{t_n}^{t_{n+1}}f(t,\phi(t))dt \quad (2.44)$$

The **Backward Euler method** estimates the right-hand side of the equation by evaluating the integral at the generic time (t_{n+1}):

$$\phi^{n+1}=\phi^n+f(t_{n+1},\phi^{n+1})\Delta t \quad (2.45)$$

2.11 Algorithms

The system of equations obtained by solving the Navier-Stokes equations present coupled terms and nonlinearities. It can be solved either in a single step in a coupled manner or in a segregated manner through iterative steps. There are two main formulations: the pressure-based and the density-based.

2.11.1 Pressure correction methods

The pressure-based formulation was originally developed to solve incompressible flows. These methods have been modified to be able to solve compressible flows too. The classical pressure-based formulation solves the system of equations (conservation of mass, momentum, and energy) in a decoupled way, but there are some algorithms that allow to solve the system coupled.

In a **segregated algorithm** each of the equations is solved starting with an approximate solution of its terms and its solution is then improved. It is necessary to iterate to obtain the final state vector.

The pressure-based method is the default option for most CFD solvers, including OpenFOAM.

Some of the most famous segregated solvers in the pressure correction methods are **SIMPLE, SIMPLEC, PISO and PIMPLE.**

2.11.2 Relaxation factor

A **relaxation factor** is used to limit the variation of each variable from the previous iteration to the next one. The introduction of relaxation factors speeds up convergence since changing one variable affects how the coefficients in the other equations are calculated. Additionally, the calculations are slowed down. Default values can be consulted in the literature, but it is possible to adapt them to the problem being simulated. The relaxation of a variable ϕ is achieved as follows:

$$\phi_P^n = \phi_P^{n-1} + \alpha \cdot (\phi_P^{n*} - \phi_P^{n-1}) \tag{2.46}$$

Where α is the factor that defines the relaxation, $\alpha < 1$ means under relaxation, $\alpha = 1$ means not relaxation, $\alpha > 1$ means over relaxation. n refers to the new value of the variable, $n-1$ refers to the previous value of the variable and $n*$ refers to the new predicted value of the variable.

The relaxation factor will result with a new matrix with a modified diagonal of the variables and a modified source vector component. In fact, the under-relaxation technique is beneficial due to the fact that increases the diagonal dominance of the matrix.

It is important to remember that a sufficient condition for the iterative procedure to converge is that the coefficient matrix is strictly diagonally dominant.

2.11.3 SIMPLE

The **Semi-Implicit Method for Pressure Linked Equations (SIMPLE)** algorithm is one of the first developed to calculate the Navier-Stokes equations using finite volumes. It was originally developed for incompressible flow, although it has been modified to account for compressibility effects.

The SIMPLE algorithm solves the momentum equation given an initial approximation of the pressure field, obtaining an intermediate velocity field. The velocity field obtained will not, in

general, comply with the continuity equation. A correction for the pressure field is calculated that allows partial fulfilment of the continuity equation. The new pressure is calculated and with it, the velocity. This method has to be iterated until convergence is reached.

The fundamental equations are the discretized continuity equation and momentum equation.

$$\frac{\partial(\rho u_i^{m*})}{\partial x_i} = 0 \tag{2.47}$$

$$a_P^{u_i} u_{i,P}^{m*} i,nb + \sum_{nb} a_{nb}^{u_i} u_{i,nb}^{m*} i,nb = Q_{u_i}^{m-1} - \left(\frac{\delta p^{m-1}}{\delta x_i}\right)_P \tag{2.48}$$

The momentum equation is modified with an under-relaxation factor as has been previously explained.

In every iteration, the right-hand terms are evaluated with the previous iteration variables (m-1). As has been said, the velocity components $u_{i,P}^{m*}$ do not satisfy the mass conservation, which is why they are marked with an asterisk.

In order to make this solution comply with the continuity condition, the provisional values of the pressure and velocity must be corrected:

$$u_i^m = u_i^{m*} + u_i^{'} \tag{2.49}$$

$$p^m = p^{m-1} + p' \tag{2.50}$$

If these expressions are substituted into the momentum equation:

$$a_P^{u_i} u_{i,P}^m - a_P^{u_i} u_{i,p}^{'} + \sum_{nb} a_{nb}^{u_i} u_{i,nb}^m - \sum_{nb} a_{nb}^{u_i} u_{i,nb}^{'} = Q_{u_i}^{m-1} - \left(\frac{\partial p^m}{\partial x_i}\right)_P + \left(\frac{\partial p'}{\partial x_i}\right)_P \tag{2.51}$$

The following relation between velocity and pressure corrections is obtained:

$$u_{i,P}' = \tilde{u}_{i,P}^{'} - \frac{1}{a_P^{u_i}} \left(\frac{\partial p^{'}}{\partial x_i}\right)_P \tag{2.52}$$

$$\tilde{u}_{i,P}^{'} = -\frac{\sum_{nb} a_{nb}^{u_i} u_{i,nb}^{'}}{a_P^{u_i}} \tag{2.53}$$

If the discretized continuity equarion is substituted with the corrected velocities the following pressure correction equation is obtained:

$$\frac{\partial}{\partial x_i}\left[\frac{\rho}{a_P^{u_i}}\left(\frac{\partial p'}{\partial x_i}\right)\right]_P + \left[\frac{\partial(\rho \tilde{u}_i^{'})}{\partial x_i}\right]_P \tag{2.54}$$

It is common to neglect the second part of the right-hand equation, because velocity corrections are unknown.

This method is severe to velocity correction and it is why the SIMPLE algorithm does not have a rapid convergence.

So, at this point, the pressure correction is obtained from Equation 2.54 and the velocities from Equation 2.49 and Equation 2.52. Since a_P coefficients are functions of other variables the

momentum equations are not satisfied, that is why an iterative process is needed until convergence is met.

An scheme of the process described can be seen in the Figure 2.17.

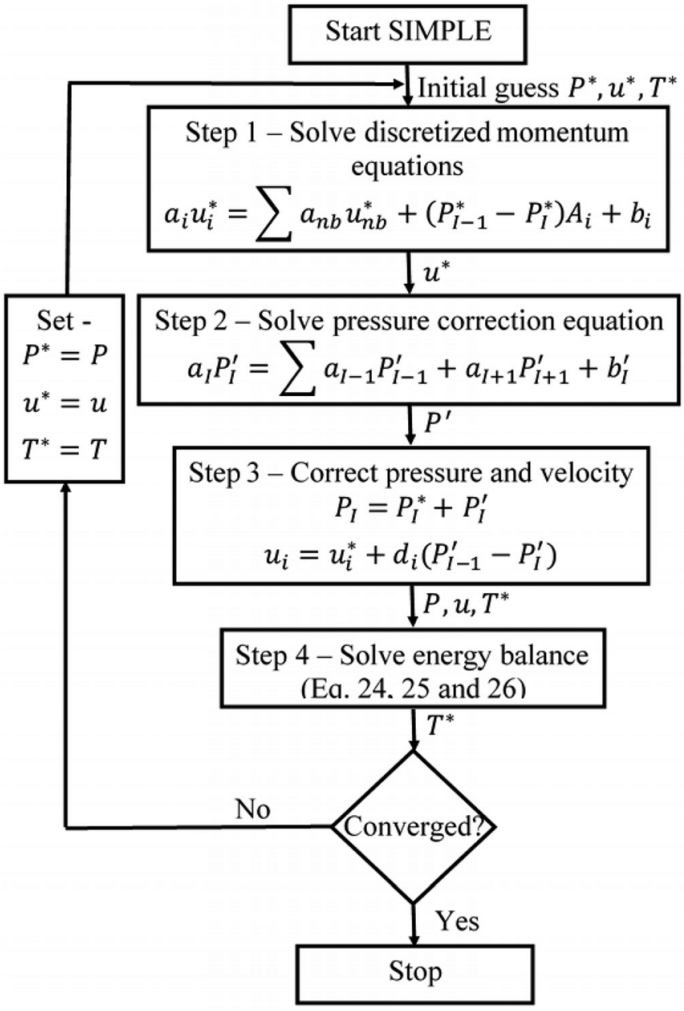

Figure 2.17: SIMPLE process. [36]

2.11.4 PISO

The **Pressure-Implicit with Splitting of Operators (PISO)** algorithm is similar to the SIMPLE algorithm, although it adds an extra corrective step. Thus, it is possible to achieve the same or higher stability with larger relaxation factors. The PISO algorithm was originally developed to solve non-stationary problems, although it was modified to solve stationary problems as well.

In the PISO method, after the new pressure and velocity fields are calculated another corrector step takes place, which means, another velocity correction u'':

$$u_{i,P}'' = \tilde{u}_{i,P}' - \frac{1}{a_P^{u_i}} \left(\frac{\partial p''}{\partial x_i} \right)_P \tag{2.55}$$

As has been explained before, this leads to a second pressure correction equation:

$$\frac{\partial}{\partial x_i}\left[\frac{\rho}{a_P^{u_i}\left(\frac{\partial p''}{\partial x_i}\right)}\right]_P = \left[\frac{\partial(\rho\tilde{u}_i')}{\partial x_i}\right]_P \tag{2.56}$$

A flowchart of the PISO algorithm can be seen in Figure 2.18.

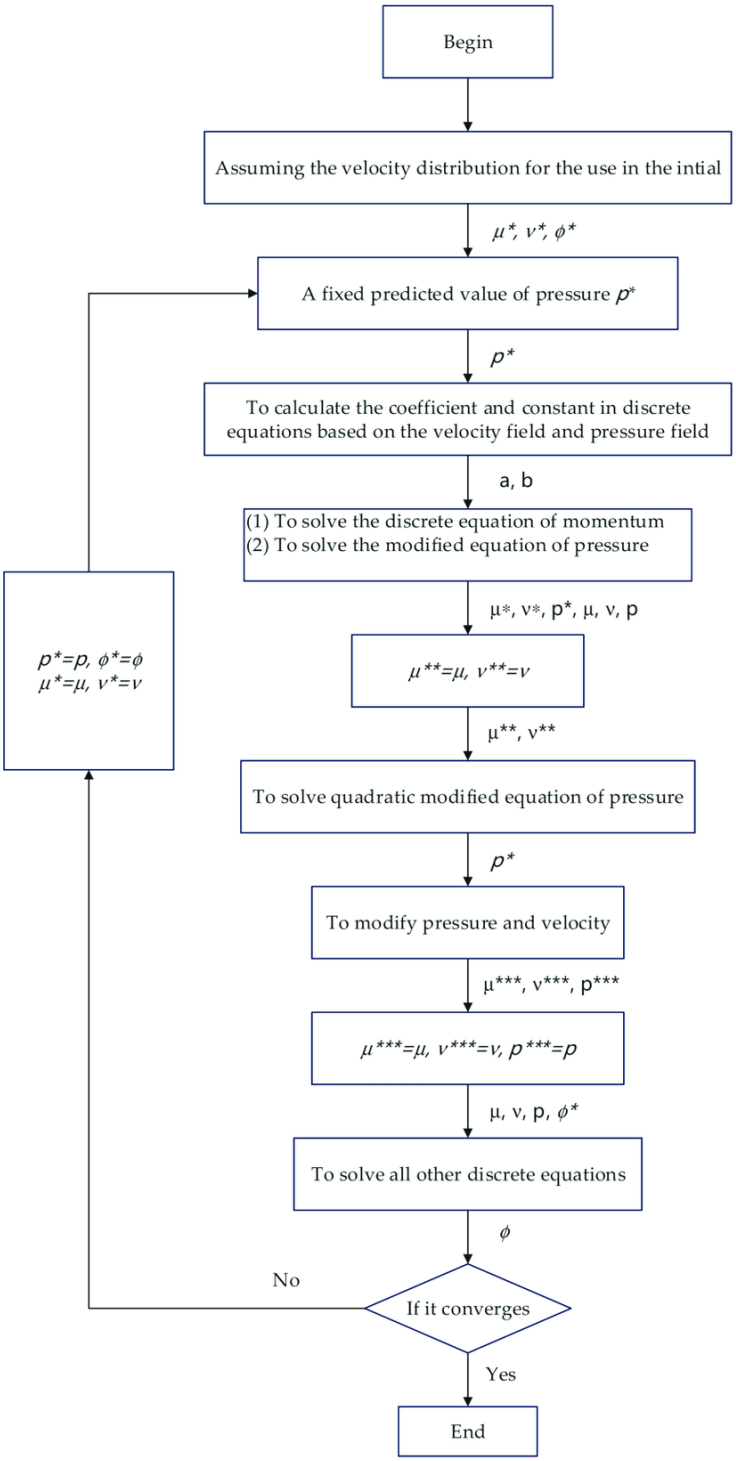

Figure 2.18: PISO algorithm. [10]

The PISO algorithm does not need an under-relaxation factor for pressure, this method is able to ensure numerical stability even though under-relaxation is not used for the variables.

2.11.5 PIMPLE

PIMPLE algorithm is a combination of SIMPLE and PISO. This method is often employed in transient simulations. This algorithm ultimately allows control of one or more loops (so-called "outer relaxation") of the PISO loop within a single time step. This allows the introduction of under-relaxation between two consecutive PISO loops, but the PISO algorithm does not provide under-relaxation. An explanation scheme can be seen in the Figure 2.19.

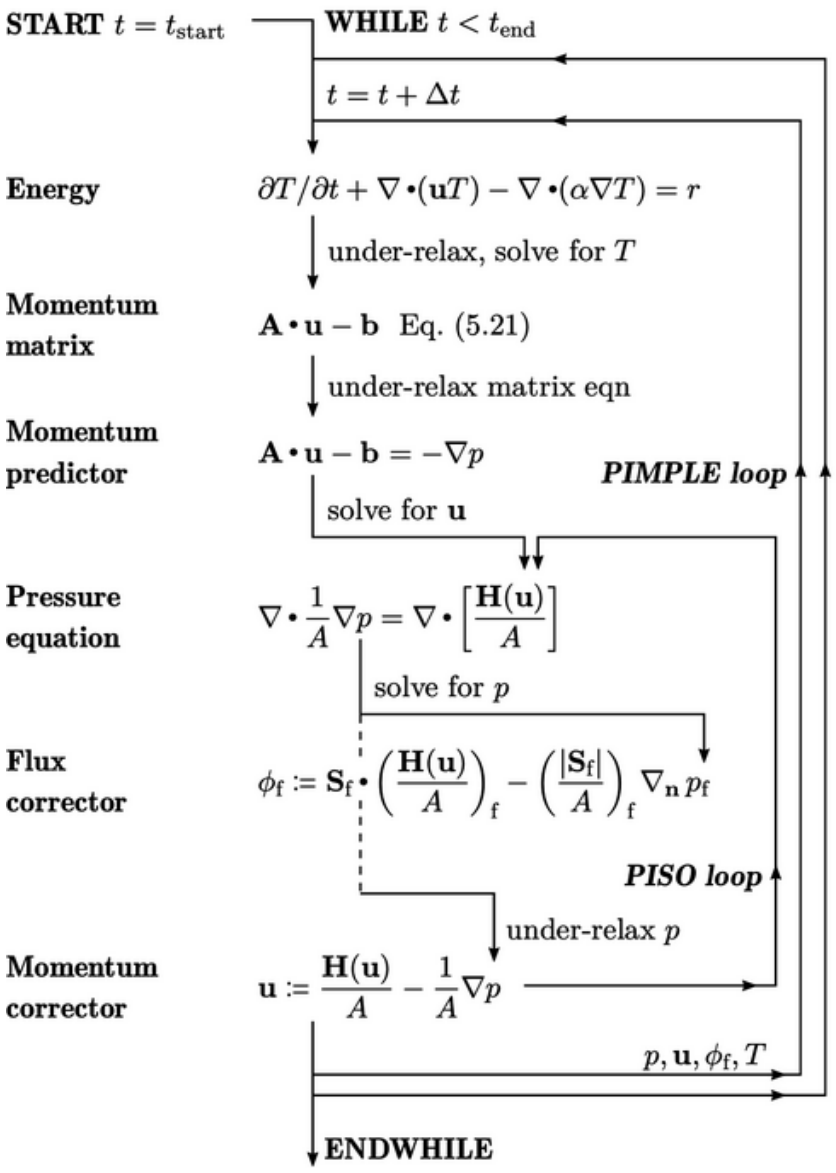

Figure 2.19: PIMPLE algorithm scheme. [11]

2.11.6 Density correction methods

The density-based formulation was originally developed to solve compressible flows. For incompressible flows, the eigenvalues of the system tend toward infinity and the other eigenvalues toward

zero, leading to numerical problems. To solve it, preprocessing is used. A matrix multiplication system is solved that guarantees that all eigenvalues have the same magnitude.

The classical density-based formulation solves the system of equations (conservation of mass, momentum, and energy) in a fully coupled manner. At each time step, the Riemann problem at the interface between cells is solved with the so-called flux difference separation scheme. These are Flux Difference Splitting Schemes (FDS).

As a general recommendation that must be reviewed on a case-by-case basis: for low speed, it is advisable to solve with a pressure-based formulation; for high speed, it is advisable to solve with a density-based formulation.

2.12 Other models

In this section will be explained other models commonly used during the setup of a CFD problem.

2.12.1 Sutherland's model

Sutherland's law is an approximation to estimate the viscosity of gases taking into account their dependence on temperature.

$$\frac{\mu}{\mu_0} = \left(\frac{T}{T_0}\right)^{3/2} \frac{T_0 + S_\mu}{T + S_\mu} \tag{2.57}$$

Where S_μ is an effective temperature called the Sutherland constant and each gas has its own value. This law can also be formulated for thermal viscosity.

The Equation 2.57 is valid for single-component gases at low pressure but it also works well for air because it is mainly composed of nitrogen and oxygen and these two gases have alike properties.

2.12.2 Arrhenius's law

Arrhenius' law is an approximation which calculates the velocity of a chemical reaction as a function of temperature. The velocity constant of a chemical reaction is called k. This value represents the number of collisions between particles that a reaction produces.

$$k = A \cdot T^\beta \exp\left[\frac{-T_a}{T}\right] \tag{2.58}$$

Where A is the pre-exponent factor, this factor represents the frequency of collisions between two molecules of the reactants with an appropriate geometric orientation which may or may not produce a chemical reaction. T_a is the activation temperature and β is the exponent of temperature in the calculation of the reaction rate. The Arrhenius equation is widely used to calculate the rate of chemical reactions. Arrhenius's concept can be explained with the Energy of activation, which is the minimum amount of energy that the reactants must have in order to transform into products. At an activation temperature, the molecules have a greater kinetic energy than the activation one.

2.12.3 Ranz Marshall correlation

The problem of heat transfer from a spherical particle to the surrounding appears in plenty of industrial processes, due to its importance a considerable amount of work has been done in order

to address the problem, especially in thermal spray processes. The Ranz and Marshall correlation explains the heat transfer between a spherical particle and the plasma gas. This can be written as:

$$Nu = h\frac{d_p}{k} = a + bRe^m Pr^n \tag{2.59}$$

Where Nu is the Nusselt number, Re the Reynolds number, Pr the Prandtl number, h the heat coefficient and k is the thermal conductivity of the gas. a, b, n and m are numerical constants that depend on the fluid and the flow geometry.

The Reynolds number and Prandtl number are defined as follows.

$$Re = \frac{\rho_c |u_{rel}| d_p}{\mu_c} \tag{2.60}$$

Where ρ_c is the density of carrier in the film surrounding particle, μ_c is the dynamic viscosity of carrier in the film surrounding particle, d_p is the particle diameter and u_{rel} is the relative velocity between particle and carrier.

$$Pr = \frac{C_p \mu_c}{k_c} \tag{2.61}$$

Where C_p is the specific heat capacity at constant pressure and k_c is the thermal conductivity of carrier in the film.

2.12.4 Rosin Rammler distribution

The Rosin-Rammler distribution is an accurate representation of the distribution of the droplet size for liquid sprays and is a "two-parameter Weibull distribution". It is difficult to describe this behaviour with only one parameter, so two parameters have been used in most of the literature. One of the parameters is often used to describe the absolute size of particles and the other is the uniformity of the sizes. With this distribution method, the range of sizes is divided into discrete intervals that are adequate, each interval is represented by a mean diameter. The mass fraction of droplets with a diameter greater than d is:

$$Y_d = \exp -(d/\bar{d})^n \tag{2.62}$$

Where $\bar{d}$ is the size constant and n the size distribution parameter which describes the uniformity.

2.12.5 Reitz Diwakar model

During the combustion process droplets break into smaller droplets for vaporisation. Accurate simulation of this process is important in order to identify possible flaws like quenching of the flame.

The Reitz-Diwakar break-up model assumes two types of separation processes: the bag break-up model and stripping break-up. When the internal pressure of the fuel particle is greater than the surface tension bag break-up occurs, this happens when the Weber number overcomes the critical one. The stripping break-up happens when the fuel is trimmed on the particle surface by surface tension.

These processes are summed up in the Figure 2.20.

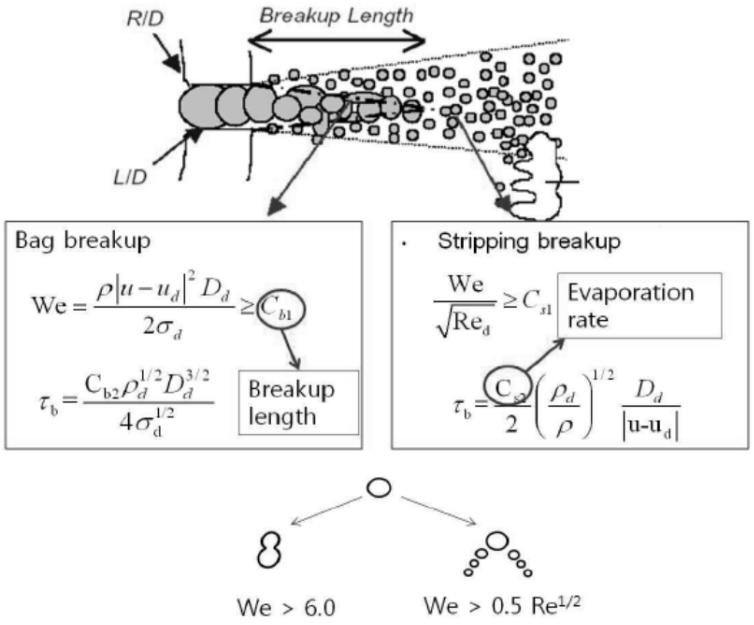

Figure 2.20: Reitz-Diwakar break-up processes. [25]

2.12.6 Sphere drag

The drag coefficient is an adimensional, it is calculated dividing the drag force by the dynamic pressure. It represents the air resistance for a given shape.

$$C_D = \frac{D}{\frac{1}{2}\rho U^2 A} \tag{2.63}$$

The Sphere drag is a model in which the drag forces are computed based on empirical expressions with the constraint that the particle remains spherical (no distortion). This is applicable to particles with homogeneous spatial distribution.

The drag expressions used are the following.

$$D = \frac{3}{4}\frac{\mu_c C_D Re}{\rho_p d_p^2} \tag{2.64}$$

$$\begin{aligned} C_D &= \frac{24}{Re}\left(1 + \frac{1}{6}Re^{2/3}\right) \quad if\ Re \leq 1000 \\ C_D &= 0.424 \quad if\ Re > 1000 \end{aligned} \tag{2.65}$$

2.12.7 Partially Stirred Reactor model (PaSR)

The chemical reaction rates are calculated with the Arrhenius' law. As a result, it is difficult to directly calculate the mean reaction rates from the average values (species mass fractions, density and temperature). Chemical source terms used both in RANS and LES simulations must be closed using turbulent combustion models.

In the Partially Stirred Reactor model (PaSR) model each cell is divided into two regions, one

reacting and one non-reacting. The mean reaction rate ($\bar{\dot{\omega}}$) will be calculated based on the mass exchange between the two zones.

$$\bar{\dot{\omega}} = \kappa \frac{\bar{\rho}(Y_i^* - Y_i^0)}{\tau^*} \tag{2.66}$$

Where $\bar{\rho}$ is the Reynolds-averaged density, Y_i^0 is the ith species mass fraction in the non-reacting zone while Y_i^* is the one in the reacting zone, τ^* is the residence time in the structure and κ is the volume fraction of the reactive region and it is the parameter that provides the Partially Stirred model.

This parameter can be known thanks to the chemical time scale (τ_c) and the mixing time (τ_{mix}) scale.

$$\kappa = \frac{\tau_c}{(\tau_c + \tau_{mix})} \tag{2.67}$$

The mass fraction in the reacting zone (Y_i^*) is obtained considering the reacting zone as an ideal reactor that evolves from the mass fraction of the non-reacting zone during the residence time.

$$\frac{dY_i^*}{dt} = \frac{\dot{\omega}_i^*}{\rho} \tag{2.68}$$

Where ω_i^* is the instantaneous formation rate of the ith species. The integration of the Equation 2.68 over the residence time gives an estimation of the reacting zone mass fraction.

The residence time will be considered as the minimum between the chemical time scale and the mixing time scale. The calculation of these time scales is another problem that must be faced. In the *OpenFoam* software class for PaSR implements the τ^* equal to the Kolmogorov time scale:

$$\tau_\eta = \sqrt{\nu_{eff}/\epsilon} \tag{2.69}$$

Where ν_{eff} is the effective viscosity (considering also turbulence) and ϵ is the turbulence dissipation rate.

The chemical time scale is calculated with the following expression.

$$\tau_c = \sum_{j=1}^{n_R} \frac{c_{tot}}{\sum_{i=1}^{N_{s,RHS}} \nu_{i,j} k_{f,j}} \tag{2.70}$$

Where n_R is the number of chemical reactions, c_{tot} is the total species concentration, $N_{s,RHS}$ the number of product species in a reaction, $\nu_{i,j}$ is the stoichiometric coefficient and $k_{f,j}$ the production rate.

In the end, the chemical time scale is the measure obtained by dividing the total species concentration by the rate at which these species transforms from the reactants to the products.

Chapter 3

Case Setup

In this chapter, a detailed explanation will be provided regarding the cases to be studied and the conditions under which they will be examined. The geometry of the analyzed combustor is also presented. Furthermore, the entire numerical setup that has been established for the simulation in OpenFOAM is described and explained.

3.1 Geometry

The geometry of the burner which is being studied can be seen in the Figure 3.1.

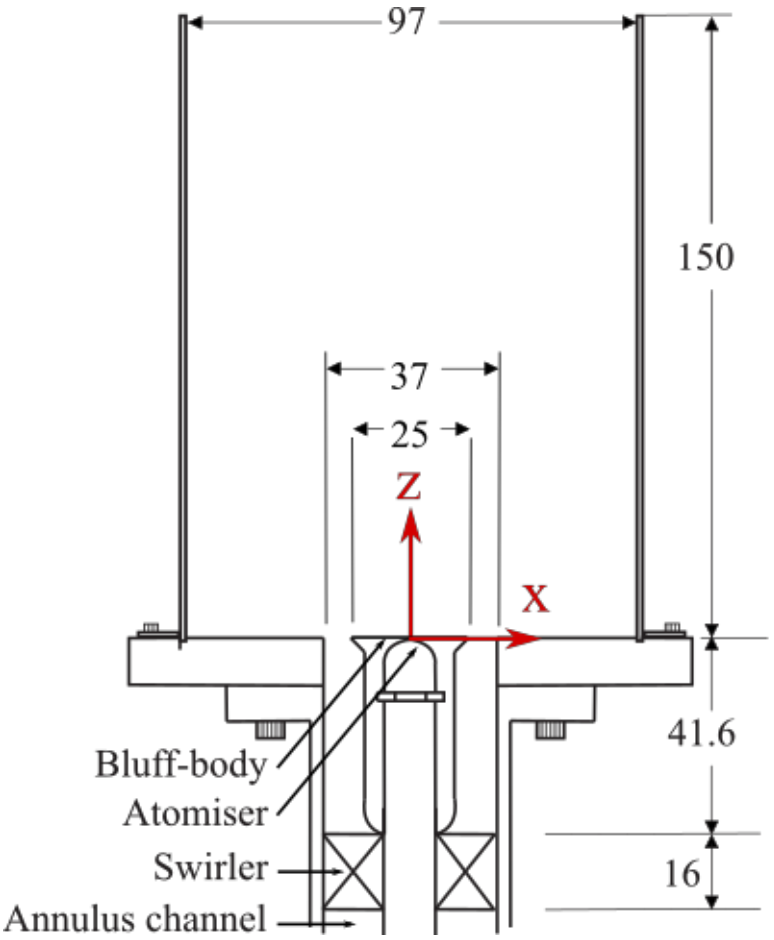

Figure 3.1: Cambridge swirl burner scheme with dimensions.[44]

Once this scheme has been generated in the OpenFOAM software, it results in a domain shown in Figure 3.2 and Figure 3.3.

Figure 3.2: Burner Geometry.

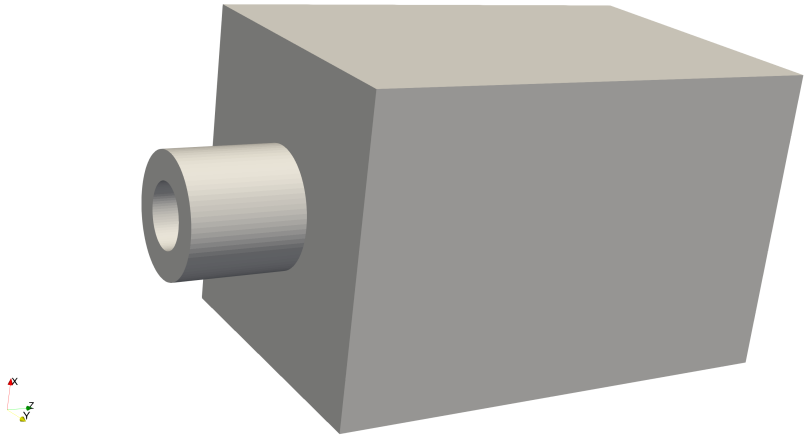

Figure 3.3: Burner Geometry.

In order to generate the swirling motion, a swirler is needed, which in this case can be observed in the Figure 3.4. As can be seen, the diameter of the hub is 11 mm while the diameter of the tip is 37 mm. The angle of the swirler blades is 60 degrees.

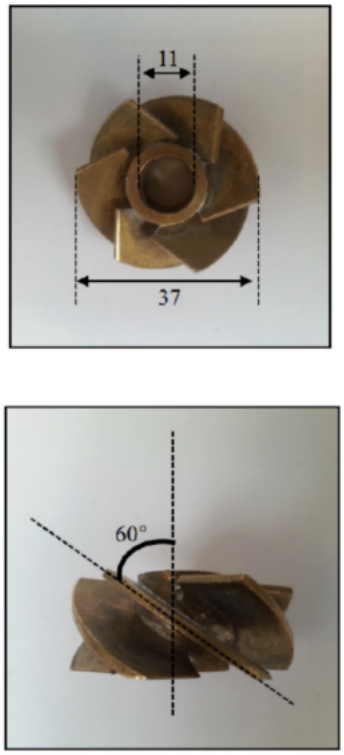

Figure 3.4: Swirler of the Cambridge Swirl Burner. [7]

In the Figure 3.5 it also can be observed the Air annulus of the Cambridge Swirl Burner, whose inner diameter is 19.6 mm.

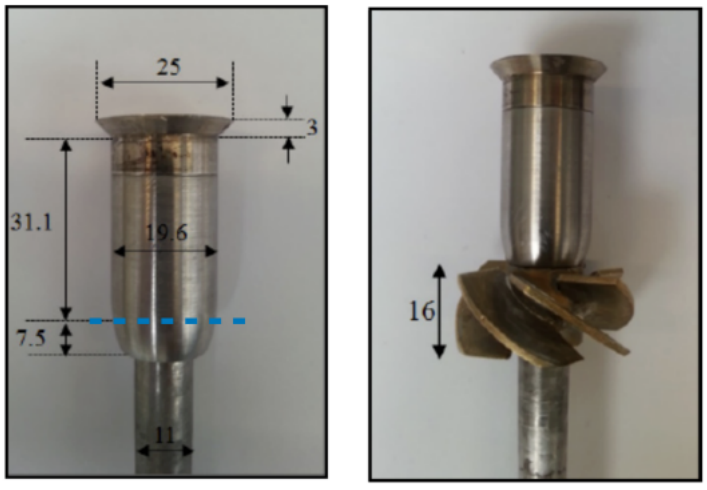

Figure 3.5: Air Annulus of the Cambridge swirl burner. [7]

3.2 Swirl Generation

The swirl in the simulation is imposed by the axial and azimuthal velocity profiles.

For stationary, axisymmetric and parallel flow, the axial and azimuthal momentum equations

with body forces are the following ([26]).

$$\begin{aligned} \frac{1}{r}\frac{d}{dr}(r\tau_{zr}) + f_z = 0 \\ \frac{1}{r}\frac{d}{dr}(r\tau_{r\theta}) + \frac{\tau_{r\theta}}{r} + f_{theta} = 0 \end{aligned} \tag{3.1}$$

For a swirling flow, it can be assumed that $u_r = 0$. Substituting the shear stresses in the momentum equations, the analytical solutions for the axial and tangential velocity can be found within some constants that will be specified by the physical conditions. For an annular jet, the conditions that have to be used are nonslip conditions. With these conditions, the velocity inflow profiles for an annular jet are:

$$\begin{aligned} U_z = -\frac{1}{4}\frac{f_z}{\mu_{air}}\left(r^2 - \frac{R_{inner}^2 - R_{tip}^2}{\ln R_{inner} - \ln R_{tip}}\ln r + \frac{R_{inner}^2 \ln R_{tip} - R_{tip}^2 \ln R_{inner}}{\ln R_{inner} - \ln R_{tip}}\right) \\ U_\theta = -\frac{1}{3}\frac{f_\theta}{\mu_{air}}\left(r^2 - \frac{R_{inner}^2 + R_{inner}R_{tip} + R_{tip}^2}{R_{inner} + R_{tip}}r + \frac{R_{inner}^2 R_{tip}^2}{R_{inner} + R_{tip}}\frac{1}{r}\right) \end{aligned} \tag{3.2}$$

Where f_z and f_θ are fictitious body forces defined to satisfy maximum axial velocity and swirl level requirements. These forces have to be solved with the following method.

The body force in the axial direction, f_z is obtained by solving the equation:

$$\int_{R_{inner}}^{R_{tip}} \rho_{air} U_z(r) 2\pi r dr = \dot{m}_{air} \tag{3.3}$$

The swirl number is estimated assuming a 60 flat-vane axial swirl generator.

$$S = \frac{2}{3}\left[\frac{1 - (R_{hub}/R_{tip})^3}{1 - (R_{hub}/R_{tip})^2}\right]\tan\varphi \tag{3.4}$$

The body force in the azimuthal direction, f_θ is solved with the following equation:

$$S = \frac{G_\theta}{R_{tip}G_z} = \frac{\int_{R_{inner}}^{R_{tip}} \rho_{air} U_z(r) U_\theta(r) r^2 dr}{R_{tip}\int_{R_{inner}}^{R_{tip}} \rho_{air} U_z^2(r) r dr} \tag{3.5}$$

3.3 Software used for the project's development

3.3.1 OpenFOAM

OpenFOAM is a widely used software in the engineering world. It is very popular due to its multiple advantages such as open code, a wide range of applications and friendly syntax.

This software is based on the FVM (Finite Volume Method) approach and solves problems related to CFD (Computational Fluid Dynamics) with compressible and incompressible flows. Also, both steady and unsteady problems can be represented with OpenFOAM.

When using OpenFOAM, solvers for different fluid configurations are developed for example with single-phase or multiphase flows. Another interesting characteristic is the capability of using systems with fixed or movable boundaries and, if necessary, rotating reference frames. Furthermore, it enables the creation of solvers for simulating problems such of different areas of expertise such as

combustion, elasticity and electromagnetics.

FOAM stands for Field Operation and Manipulation because it treats the known "field" problems, which deal with velocity, pressure, density and other fields.

3.3.2 ParaView

ParaView is a widely used software for postprocessing CFD problems and other applications which makes it an attractive option in the field of engineering. Also, one of the things that makes it interesting to use is that is cost-free and open-code.

With the help of this program, data can be seen and analysed, enabling the possibility to explore 3D data too. Large datasets can be analyzed using the program on supercomputers, while smaller ones can be analyzed on PCs. Another facility offered by this program is that it allows vertical applications to be made so that all its components can be reused.

3.4 Mesh

The mesh of the cases is created with the mesh generation utility, `blockMesh`. With this utility the mesh is created with a dictionary file named `blockMeshDict`. Reading this dictionary the mesh data, points, faces and boundary files are written in the directory.

Also, `blockMesh` decomposes the domain in different three dimensional hexahedral blocks. In the case of study the number of blocks are 14.

Among the geometry, the boundaries need to be defined. A boundary is usually formed by a group of patches. One patch can include various areas of the boundary which do not have to be connected in a physical way.

In this case, two types of patches are defined:

- **Type patch:** this is defined for the inlet and outlet. This type of condition does not contain geometric or topological information about the mesh. It is a generic patch.
- **Type wall:** is used for the rest of the walls. This type is used for wall functions in turbulent flows as it stores the distance from the wall to the centre of the cell as part of the patch.

In the case of study the mesh is composed only of hexahedra and the number of cells is **1488800**. The maximum non-orthogonality is 42.3^{o} with an average value of 8.2^{o} and the maximum skewness is 0.69.

The mesh can be observed in the Figure 3.6 and Figure 3.7.

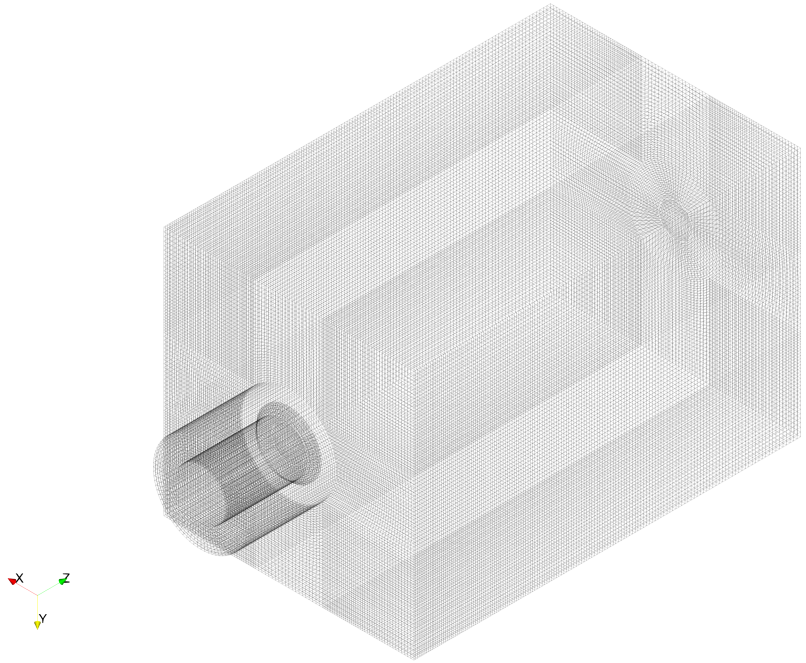

Figure 3.6: Mesh.

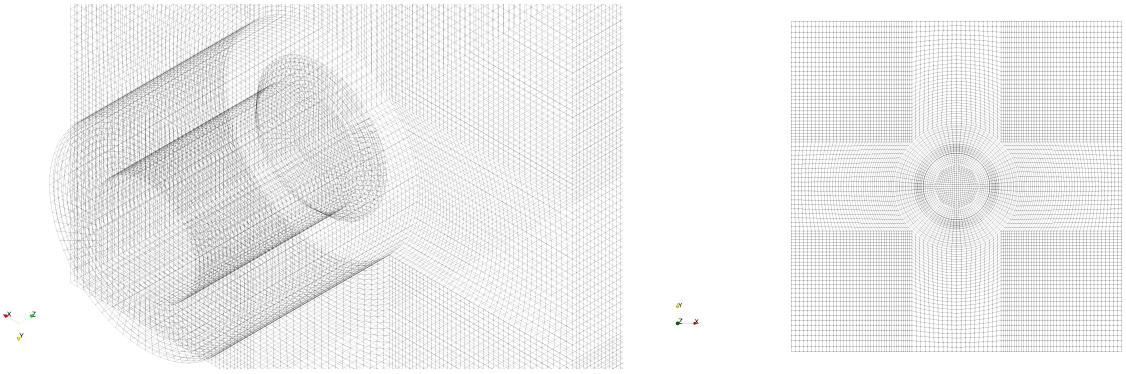

(a) **(b)**

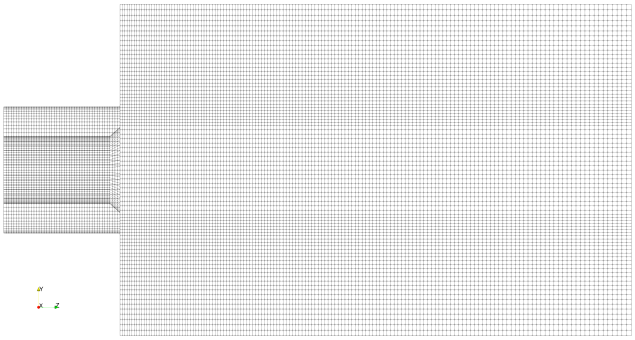

(c)

Figure 3.7: Mesh details.

3.5 Test cases

In this project, a series of cases have been carried out in the OpenFOAM software. The main characteristics are shown in the Table 3.1.

First, two cold gas simulation cases, in which only air with different velocities has been used. Second, a reactive case with heptane has been simulated. The reactive case has been simulated in two different ways, first with a **one-step chemical reaction** and second with a **reduced chemical mechanism of 52 species** provided by Centre Europeén de Recherche et de Formation Avancée en Calcul Scientifique (CERFACS). [5]

Finally, due to the results obtained with the CERFACS mechanism and because time has been available one more simulation has been carried out with another mechanism. This second mechanism is a high-temperature ignition one with **37 species and 88 reactions** [40].

Fuel type	**Condition name**	$\dot{\mathbf{m}}$ **[g/s]**	$\mathbf{U_{bulk}}$ **[m/s]**	ϕ
Cold Flow	C1	-	14.3	-
Cold Flow	C2	-	18.5	-
n-Heptane	H1S1	0.27	17.1	0.32

Table 3.1: Test cases conditions.

The simulations are conducted under atmospheric conditions, with a pressure of 1 atmosphere. The reactive case of n-heptane is performed with air. Furthermore, as can be seen in the table, the equivalence ratio is less than 1, which means that the reactive simulations are lean. This indicates that there is more air than needed for combustion. There are several reasons for choosing to operate gas turbine combustors with a lean fuel-air mixture. By running the combustion process lean, it's possible to avoid the combustion temperatures at which the rates of NO formation begin to increase. Additionally, it becomes feasible to achieve conditions that are favourable for oxidizing unburned hydrocarbons and carbon monoxide. Consequently, operating with a lean mixture offers clear advantages in terms of emissions control.

3.6 Directory structure

In order to simulate the cases a directory has been created with the typical structure of OpenFOAM directories.

There are three main folders: constant, system and 0.

The *constant* folder is the one which contains the information that is constant during the simulation. Inside the constant folder, there is the *polymesh* folder which has all the information about the mesh (points, faces, boundary, etc.).

The *system* directory holds all the parameters related to the solution process.

The *0* directory represents the initial time step or zero time. It contains the initial and boundary conditions for variables such as pressure (p) and velocity (U), which are stored in separate files.

3.6.1 Constant folder

In the *constant* folder can also be found different files which specify physical properties for the application.

Some of the files in this folder are the following:

- Species: defines the number of species that will take place in the reaction. It also defines the thermodynamics and transport characteristics. The polynomial model coefficients are used for the heat capacity and Sutherland's model coefficients for viscosity.

  In the **one step heptane case** there are five species: C_7H_{16}, O_2, N_2, CO_2 and H_2O. In the case of the **chemical mechanism**, the interpreted species come from the *chemkin* folder that will be explained later.

- Reactions: contains the reactions that are going to happen during the simulation. In the no-reacting test cases, there is only cold air through the chamber. In the reacting test cases will appear different reactions.

  For the **one step heptane case** the reaction is defined as an irreversible Arrhenius reaction in which the reaction is defined as:

$$C_7H_{16}^{0.25} + 11O_2^{1.5} = 7CO_2 + 8H_2O \tag{3.6}$$

  Where the exponents are the reaction orders which are calibrated to reproduce global reactions. The reaction rate is calculated using the Arrhenius equation (Equation 2.58). For the one step case the values are $A = 2811706.63\ s^{-1}$ $\beta = 0$ and $T_a = 79450.36$ K.

  In the case of the chemical mechanism, all of this will be interpreted based on the information contained in the *chemkin* folder, which will be explained later on.

- Thermophysical properties: the physical properties of the species can be set. In the reacting cases, a **multi-component mixture** is defined. The transport properties that are temperature-dependent are calculated with Sutherland's formula. The thermophysical model calculator is the `hePsiThermo` whose calculation is based on enthalpy or internal energy and compressibility. The specific heat at constant pressure is evaluated by a function of coefficients from Joint Army–Navy–Air Force (JANAF) thermodynamic tables, thanks to this the enthalpy and entropy can be evaluated.

- Thermophysical transport: the turbulence thermophysical transport model class is defined. a Non-unity-Lewis-Eddy-diffusivity model is used. This model allows independent Prandtl and Schmidt numbers. Lewis is assumed as unity in laminar. In this case, the Prandtl and Schmidt are defined as 1.

- Momentum transport: defines the simulation type and treatment of turbulence. In the case of study, the type of simulation is **Reynolds Averaged Simulation (RAS)** and the turbulence model is `RNGkEpsilon` which is a mathematical technique that allows to develop a turbulence model that is similar to the k-epsilon.

- Combustion model. Defines the combustion properties. In this case, the combustion model used is the **Eddy Dissipation Concept (EDC)** which is a turbulent combustion model.

Also, the partially stirred reactor turbulent combustion model is used with a Cmix parameter of 1. This parameter is used to scale the turbulence mixing time scale.

- Spray cloud properties: defines the properties of the spray. The integration schemes are the Euler for the velocity and analytical for temperature. The initial temperature for the spray droplets is 300 K and the density 678.03 kg/m^3.

  In this file are also described other sub-models as the following: There is an additional force which is the sphere Drag which calculates the drag force.

  The injection model is also described. In the case of study, a **cone injection** is used. The dimensions of this cone are defined as well as the flow type which is one of constant velocity. The size distribution of the droplets is calculated with the Rosin Rammler distribution.

  For the heat transfer from the surface of a sphere, the Ranz-Marshall correlation is used. The break-up model is the Reitz-Diwakar.

  This file also describes the mixture as a single phase with a phase change model of liquid evaporation boil that uses an ideal gas assumption. There is no stochastic collision model which means dummy collision. The wall interaction model is "rebound" which optionally specifies elasticity and restitution coefficients. There is no atomization model so the phase change is dummy.

- Radiation properties: defines the type of radiation used. In the case of study the **radiation is not considered** so the `noRadiation` class is used, which does nothing to energy equation source terms.

3.6.2 System folder

The system folder contains all the parameters essential to the solution procedure. In this directory the folowing files can be found.

- *controlDict*: specifies the run control parameters, start and end times, time step, write interval, etc. In this file, the simulation's final time is defined as 1 second (`endTime`), and the time step is set to 1e-06 seconds.

- *fvSchemes*: the finite volume discretisation schemes are defined here. The first-time derivative terms are discretized with the **Euler scheme**, which is of first order and implicit.

  The gradient schemes are discretized with a **Gauss Linear**. For the divergence terms, the Gauss scheme is the only choice of discretisation but the interpolation scheme can be selected. For the velocity, enthalpy and pressure a **Gauss linear upwind** method is used, which is an accurate and stable numerical scheme (second order accurate).

  For the discretization of the diffusive terms, a fully orthogonal scheme is used which is a **Gauss Linear Corrected** in which an explicit **non-orthogonal correction** can be added to the orthogonal component. This correction increases in size if the non-orthogonality increases.

  The interpolation schemes are **linear**.

  A **corrected surface-normal gradient scheme** is used, which is a central difference gradient scheme with explicit non-orthogonal correction.

The distance to the wall is found solving the Poisson equation.

- *fvSolution*: contains equation solvers and algorithm controls.

  The linear solvers that are used for each discretised equation are specified. The linear solver is the term used to describe the method of number-crunching the group of linear equations in order to solve them. These solvers distinguish between symmetric and asymmetric matrices.

  In this file, the solution tolerances are also defined. As the solutions are iterative, the solvers are based on reducing the residuals of each equation. In each iteration, the residual is re-evaluated. A `tolerance`, relative tolerance (`relTol`) and a maximum number of iterations (`maxIter`) may be defined. These values will guide to know when to stop the iterations. If the residual is lower than the tolerance, or the ratio of current to initial residual is lower than the relative tolerance or the maximum number of iterations is reached, the solver will stop.

  The tolerance defines if the residual is small enough to accept the solution (among other things) while the relative tolerance limits the relative improvement between the initial to final solution. In transient simulations, the solver relative tolerance is usually set to zero to force the convergence.

  There are also options for preconditioning of matrices in the conjugate gradient solvers. The idea of this preconditioning is to modify the system in order to obtain an equivalent modified system for which the convergence is reached faster.

  There are solvers that require a smoother that must be specified. The smoothers are operators that would drive the solution error toward zero. Typically they are used to reduce high-frequency errors.

  Relaxation factors are also defined. The relaxation factor is set to 1 so there is **not under-relaxation**. The solver and conditions used for each variable are specified in the Table 3.2.

Variables	Solver	Preconditioner	Smoother	Tolerance	Relative tolerance
ρ	PCG	DIC		1e-05	0.1
U,k,ϵ,R	smooth solver		Symmetric Gauss Seidel	1e-08	0.1
p	GAMG		Gauss Seidel	0	0.1
h,Yi (O_2,N_2,H_2O)	PBiCGStab	DILU		1e-07	0.1

Table 3.2: Solution subdictionaries for the case of study.

The Preconditioned Conjugate Gradient (PCG) exploits the structure of symmetric positive definite matrices. The `PBiCGStab` is the stabilized preconditioned conjugate gradient.

The Geometric Algebraic Multigrid (GAMG) is often a good solver for the pressure equation. This solver consists of two phases, the set-up and the solver phase. In the first phase, a set of coarsed meshes is created. The solution in this new mesh with a smaller number of cells is calculated, which is quicker, then, this solution is mapped onto a finer mesh, using it as an initial guess in order to obtain an accurate solution on the fine mesh.

The Diagonal Incomplete-LU (DILU) preconditioner is asymmetric. The Incomplete LU factorization changes a matrix into the product of two, a lower triangular matrix L, and an upper triangular matrix U.

The Diagonal Incomplete-Cholesky (DIC) can be a good option in terms of conservation for bad matrices. This is an incomplete factorization method based on a matrix decomposition. This factorization is carried out using two matrices, one of which is a lower triangular matrix and the other is its conjugate. In the case of incomplete factorization, the factorization is given by a lower triangular sparse matrix (K). The factorization would be $A = KK*$.

A Gauss-Seidel method is an iterative technique used to solve the number of equations of a square system. This method consists of a forward sweep followed by a backward sweep.

The relative tolerances are set to zero for the final values of the variables specified previously in the Table 3.2.

The **PIMPLE** algorithm is selected as the iterative solver. The number of outer correctors is set to 3 (`nOuterCorrectors`), this activates the PIMPLE loop leading to a re-calculation of the pressure-momentum coupling. In this case, three times in a one-time step. The number of correctors (`nCorrectors`) is set to 2, these are the correctors for the PISO loop which in this case will re-calculate the pressure twice. Also, the PIMPLE algorithm is set with a **non-orthogonal corrector** (`nNonOrthogonalCorrectors`), which after solving the pressure equation once, solves it again to take into account the mesh non-orthogonality and enhance convergence.

3.6.3 Chemkin folder

The *chemkin* folder is the one that contains the information of the selected chemical mechanism.

CHEMKIN is a software package designed to simplify the creation, solving, and comprehension of problems related to elementary gas-phase chemical reactions. It offers a versatile and robust tool for integrating intricate chemical kinetics into fluid dynamics simulations.

Within this folder, three files should be found, namely:

- *chem.inp*: manages gas-phase equation-of-state, thermodynamic properties, and chemical kinetics.
- *therm.dat*: which is the thermodynamic database.
- *transport.dat*: deals with gas-phase molecular transport properties.

Chapter 4

Results and discussion

4.1 Cold gas simulations

4.1.1 C1 case

The first case to analyze is the C1 case of the cold gas simulations. In Figures 4.1a and 4.1b can be observed the field of temperature and speed in a normal slice in the Y axis that cuts the burner in half.
The first thing that can be observed is a homogeneous distribution of the temperature, which is to be expected since this simulation is not reactive and is carried out only with cold air. That is why a temperature of about 288 K can be seen throughout the chamber.
As it has been well said, since it is a non-reactive simulation, the only field of interest is the velocity. A symmetrical case can be seen, in which there is an area of the flow with high speed (the entrance region) and the rest of the flow, most of it, is maintained at a lower speed, in fact, an order of magnitude lower. This can be explained thanks to the recirculation and reverse flow zones that have been explained earlier in the theory.

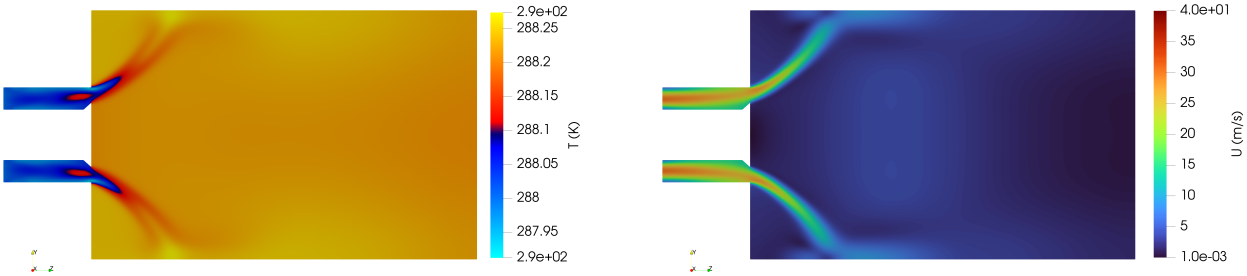

(a) **(b)**

Figure 4.1: (a) Temperature field for the C1 case. (b) Velocity field for the C1 case.

The recirculation zones can be better observed in Figure 4.2. A Central Toroidal Recirculation Zone (CTRZ) can be clearly distinguished in the centre of the flow and the Corner Recirculation Zone (CRZ) can be seen at the corners. With the direction of the arrows in the figure, the reverse flow is also identified.

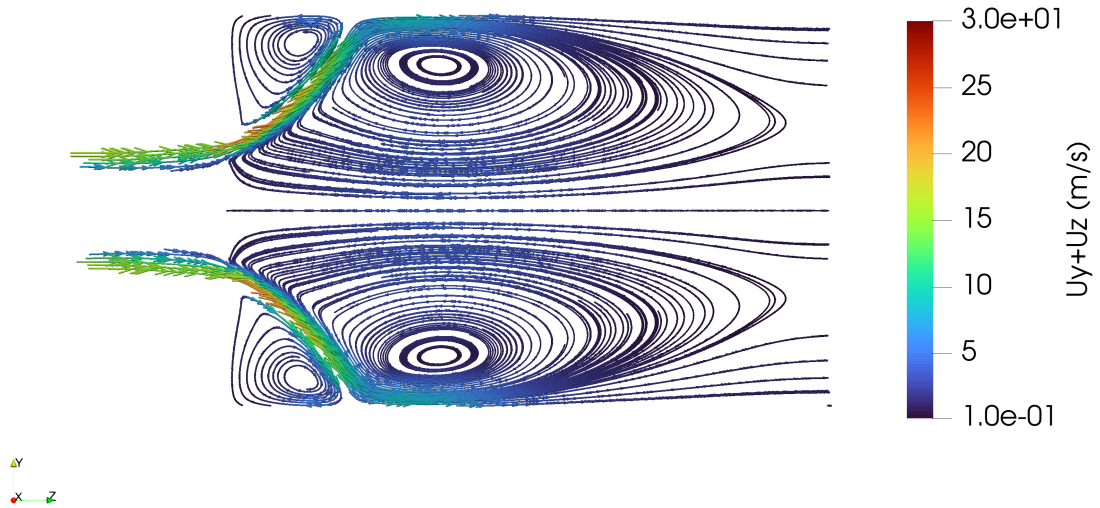

Figure 4.2: Axial and radial velocities for the C1 case.

The distribution of axial velocities along the length of the burner on surfaces normal to the Z axis has also been studied. Figure 4.3a shows the areas closest to the entrance. In addition, the recirculation mentioned above is confirmed here too.

The distribution is symmetrical and the velocity peaks are observed near the inlet in the flow zone that divides the central recirculation and the corner recirculation. If the other figures are analyzed (4.3b and 4.3c), it is evident that the peaks decrease until they reach an almost flat distribution towards the end of the burner. The central flow zone with a negative velocity confirms the occurrence of reverse flow.

This case has also been validated with the official repository of Cambridge University. From which experimental data of both cold gas cases are obtained. As is known, validation in CFD simulations is very important to ensure the certainty of the results. In this case, the velocity distributions along the length of the burner are compared. The comparison of the axial distribution of velocities has been carried out in three points of the chamber. One at 49mm (figure 4.4a), another at 59mm (figure 4.4b) and the last at 74mm (figure 4.4c).

The experimental data shows the same trend as the results using the software. In fact, they are practically identical. Again, the area of greatest velocities is at the start of the burner.

Radial velocity profiles along the burner are shown in figures 4.5a, 4.5b and 4.5c. Thanks to the positive and negative values of this distribution, the existence of the recirculation flow can be confirmed. Again, these values have been compared with the experimental data obtained by the University of Cambridge (figures 4.6a, 4.6b and 4.6c). As with the axial velocities, the behaviour is very similar.

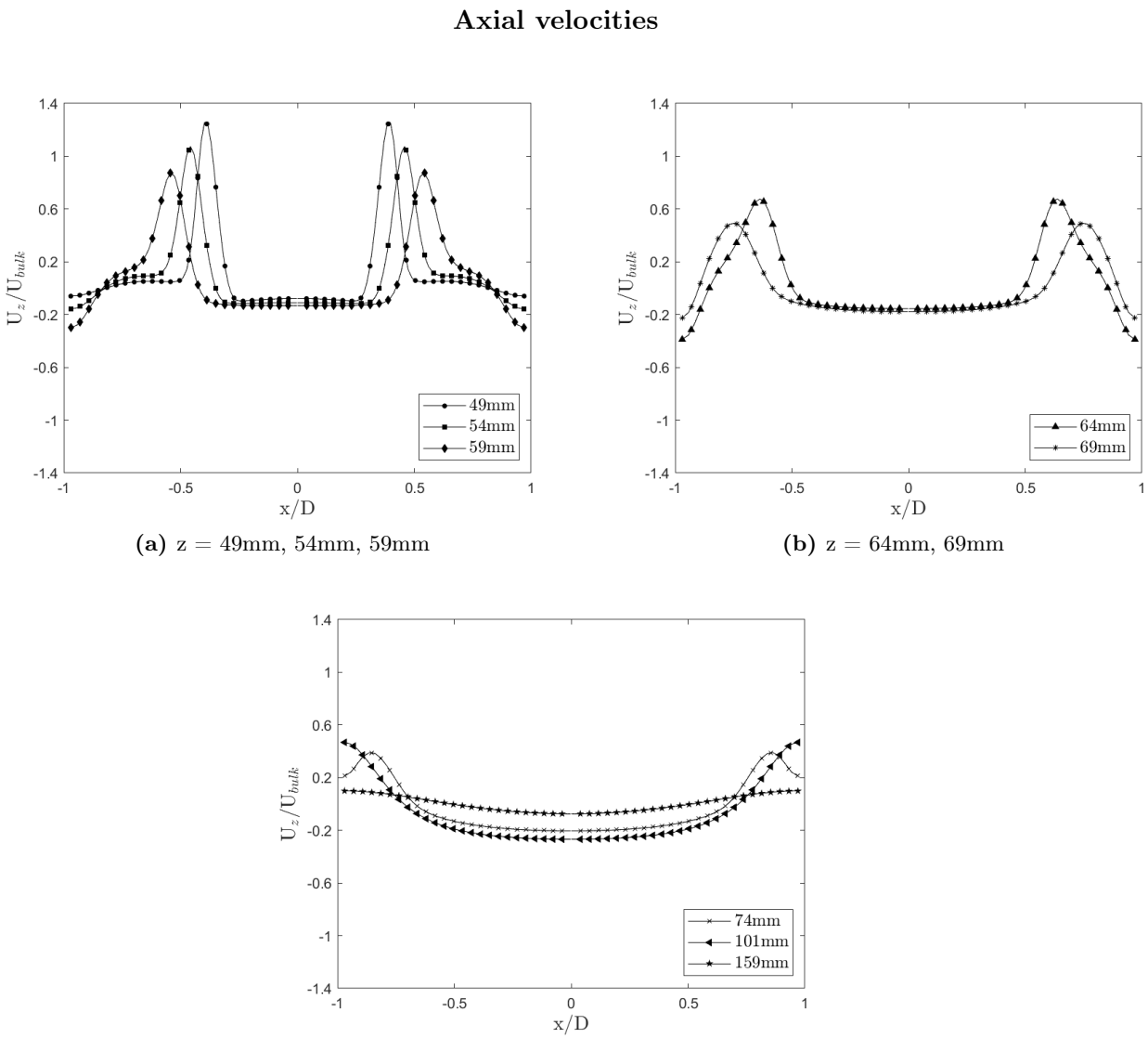

(a) z = 49mm, 54mm, 59mm

(b) z = 64mm, 69mm

(c) z = 74mm, 101mm, 159mm

Figure 4.3: Axial velocities for the cold gas case C1.

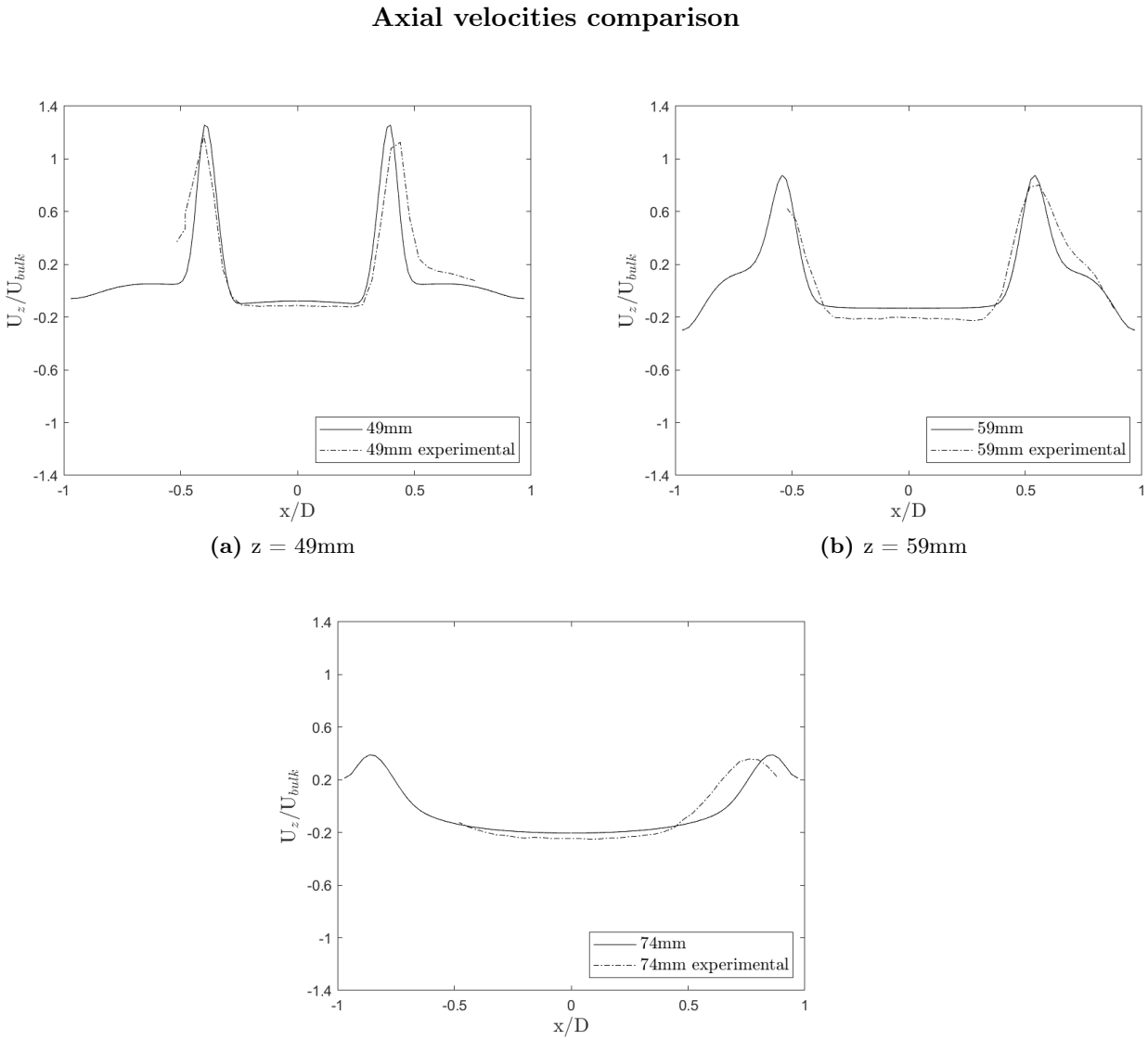

(a) z = 49mm

(b) z = 59mm

(c) z = 74mm

Figure 4.4: Comparison between experimental and numerical results of the axial velocities for the cold gas case C1.

Radial velocities

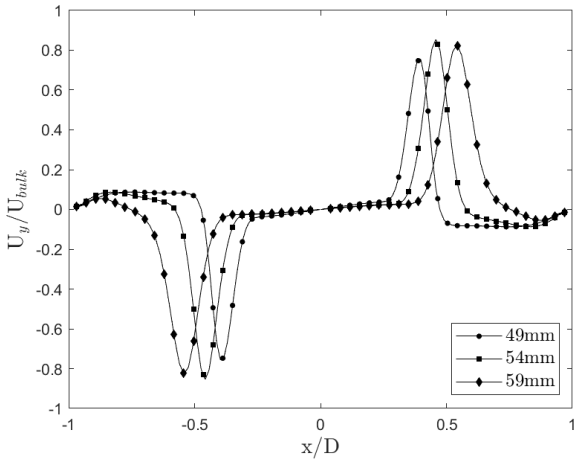

(a) z = 49mm, 54mm, 59mm

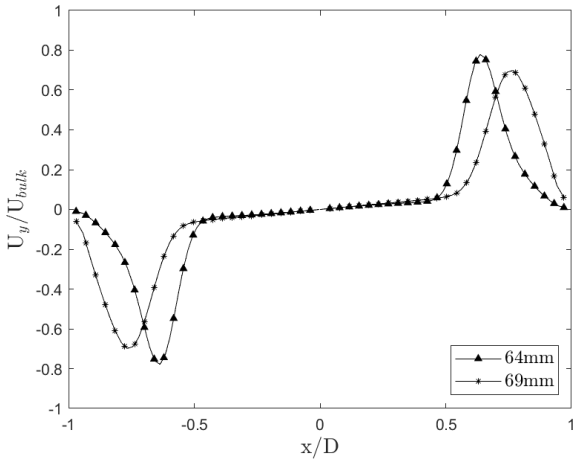

(b) z = 64mm, 69mm

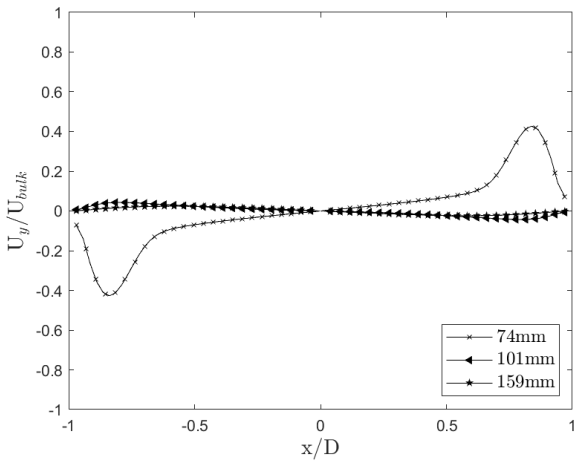

(c) z = 74mm, 101mm, 159mm

Figure 4.5: Radial velocities for the cold gas case C1.

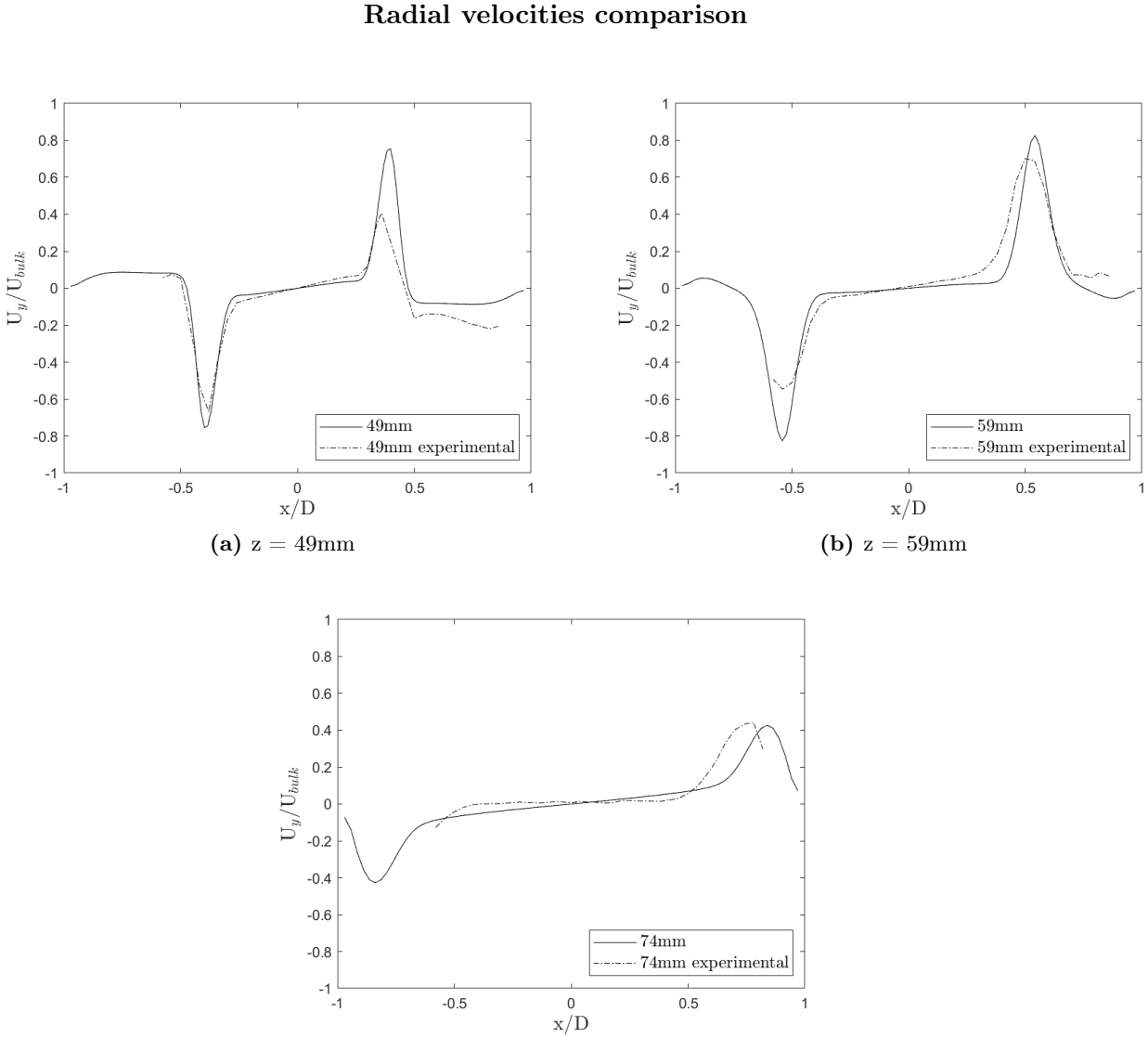

(a) z = 49mm

(b) z = 59mm

(c) z = 74mm

Figure 4.6: Comparison between experimental and numerical results of the radial velocities for the cold gas case C1.

Swirl velocities

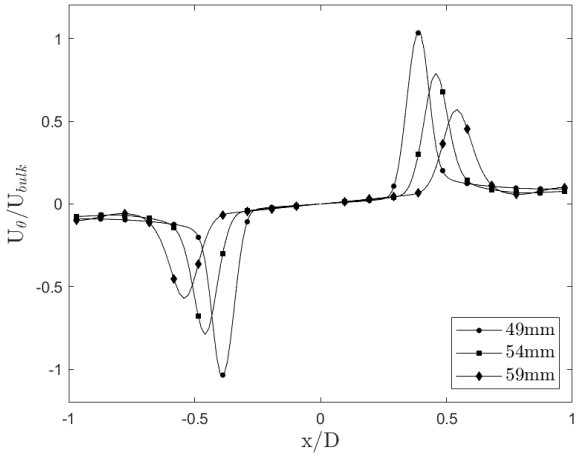

(a) z = 49mm, 54mm, 59mm

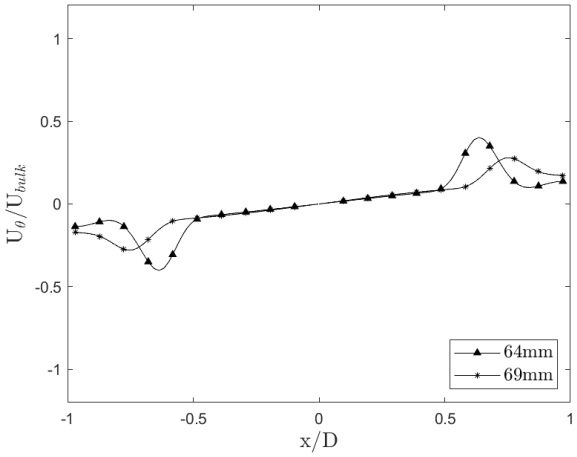

(b) z = 64mm, 69mm

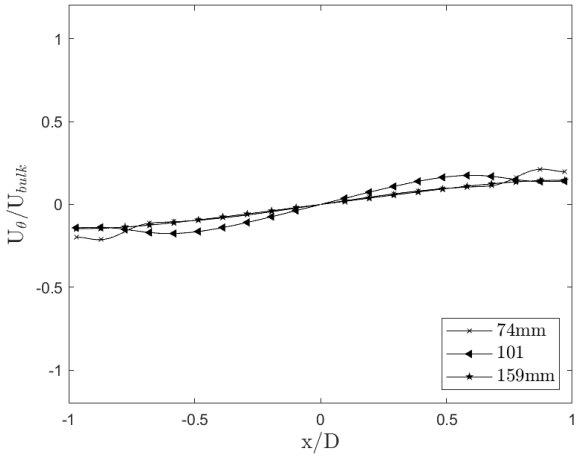

(c) z = 74mm, 101mm, 159mm

Figure 4.7: Swirl velocities for the cold gas case C1.

Lastly, the swirl velocities have been analyzed in figures 4.7a, 4.7b and 4.7c. The behaviour of these velocities is the same as the previous profiles, as the distance to the combustor inlet increases, the distribution becomes flatter and the peaks less pronounced. Negative speed zones are observed which, once again, verify the flow recirculation zones.

The comparison of these data with the experimental ones is made in the figures 4.8a, 4.8b and 4.8c. Again, the experiments carried out with the case analyzed by CFD are validated.

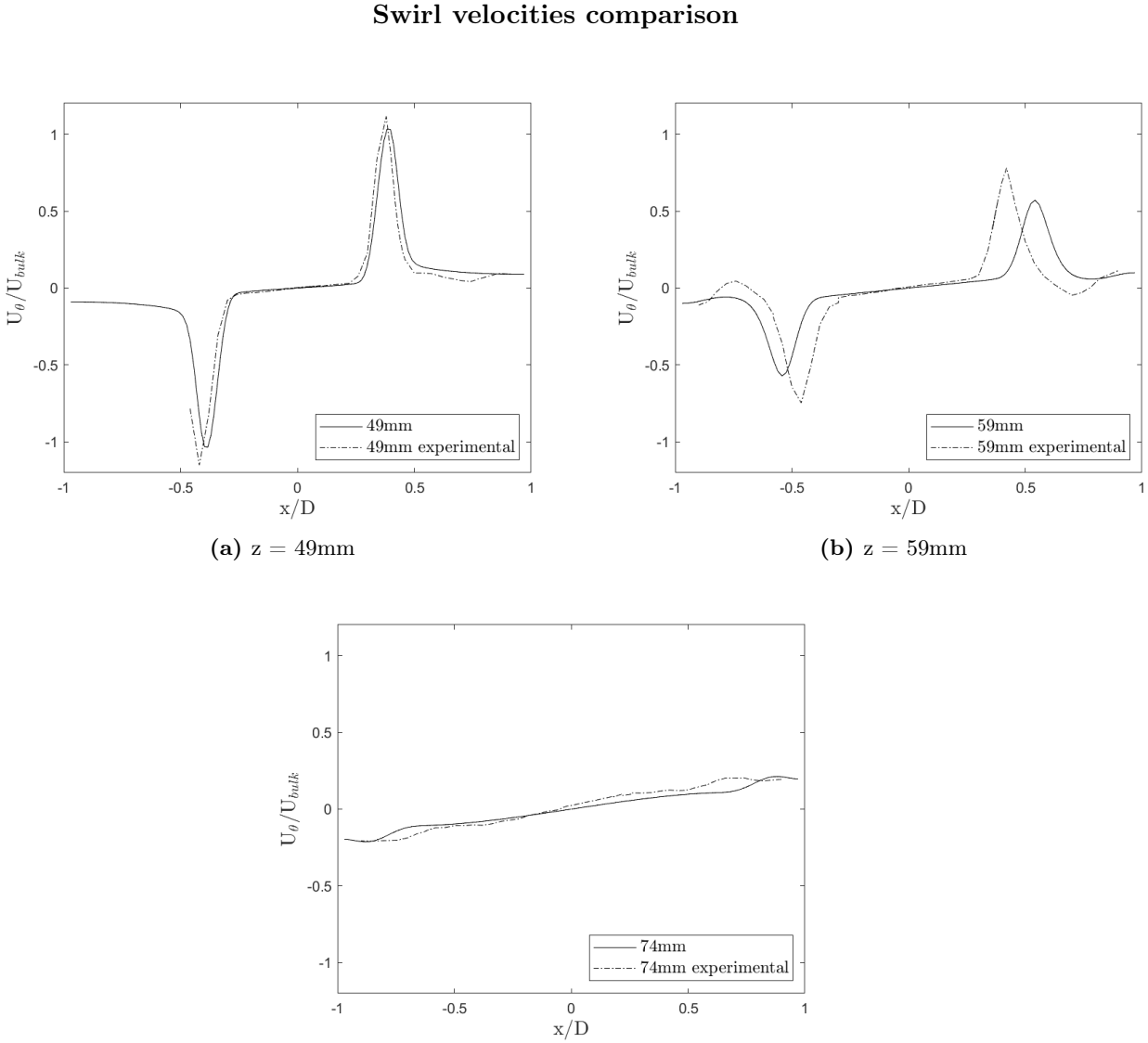

(a) z = 49mm

(b) z = 59mm

(c) z = 74mm

Figure 4.8: Comparison between experimental and numerical results of the swirl velocities for the cold gas case C1.

In terms of velocity magnitude, the axial, radial and swirl types exhibit the same magnitude order. When located at z=49mm maximum values are around 18 m/s. At z=74mm the maximum values decline and fall within 5 and 8 m/s.

4.1.2 C2 case

The C2 case is, again, a cold gas simulation, the only difference between this case and the previous one is the increase in mass flow rate. As previously mentioned, since it is a non-reactive case, only the velocity field will be observed.

In Figure 4.9 the velocity field of this case is displayed as was done with the previous case (C1). The only difference is the increase in speed, which is observed in comparison with the graphs of the previous case (Figure 4.18), the velocity is higher in this case, reaching nearly 40 m/s while in the C1 case, the maximum velocity is around 30 m/s.

Figure 4.9: Velocity field for the C2 case.

The streamlines with the radial and axial velocities are shown in Figure 4.10. The identified recirculation zones are the same as in the previous case, as expected.

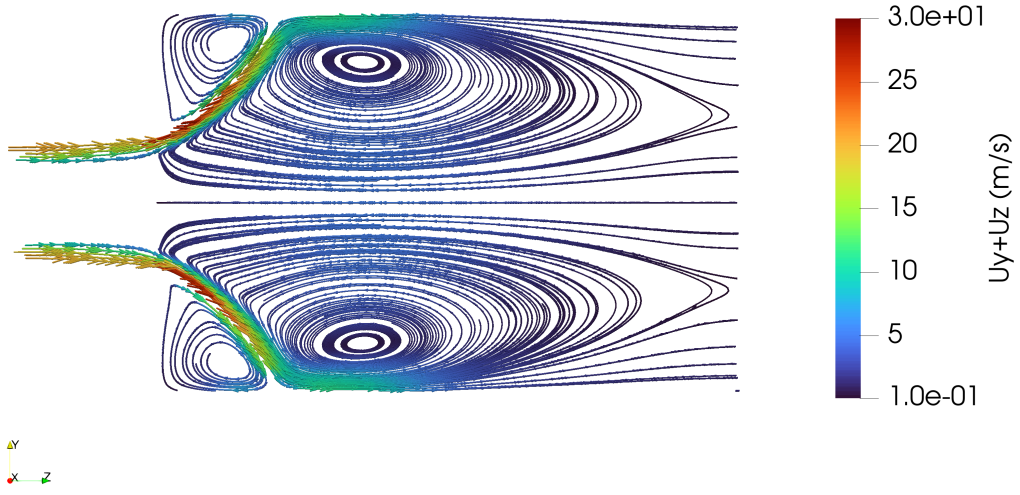

Figure 4.10: Streamlines with axial and radial velocities for the C2 case.

Again, velocity profiles on a surface normal to the Z axis through the length of the burner are analyzed. As with the previous simulation, validation is performed with the experimental data from the Cambridge University repository.

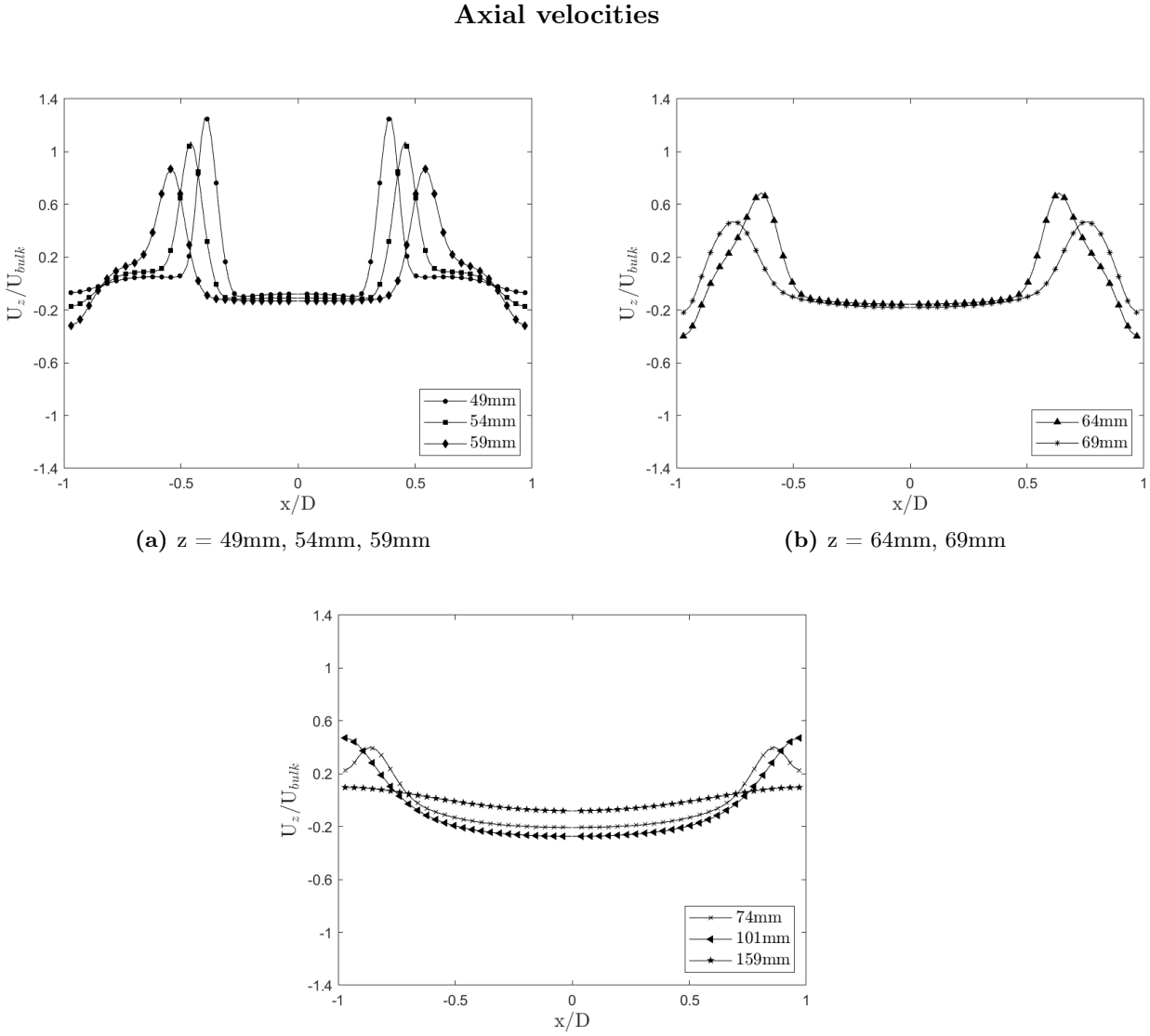

(a) z = 49mm, 54mm, 59mm

(b) z = 64mm, 69mm

(c) z = 74mm, 101mm, 159mm

Figure 4.11: Axial velocities for the cold gas case C2.

Figures 4.11a, 4.11b and 4.11c show the axial profiles, which are exactly the same as those of the C1 case (figures 4.3a, 4.3b and 4.3c), since both are normalized by their bulk velocity. The same analysis is done for radial and swirl velocities. These are not shown in this document to avoid repetition.

Likewise, the comparison between the experimental cases and the CFD simulation for the axial velocity can be observed in figures 4.12a, 4.12b and 4.12c, looking at the results, this simulation can be validated as well.

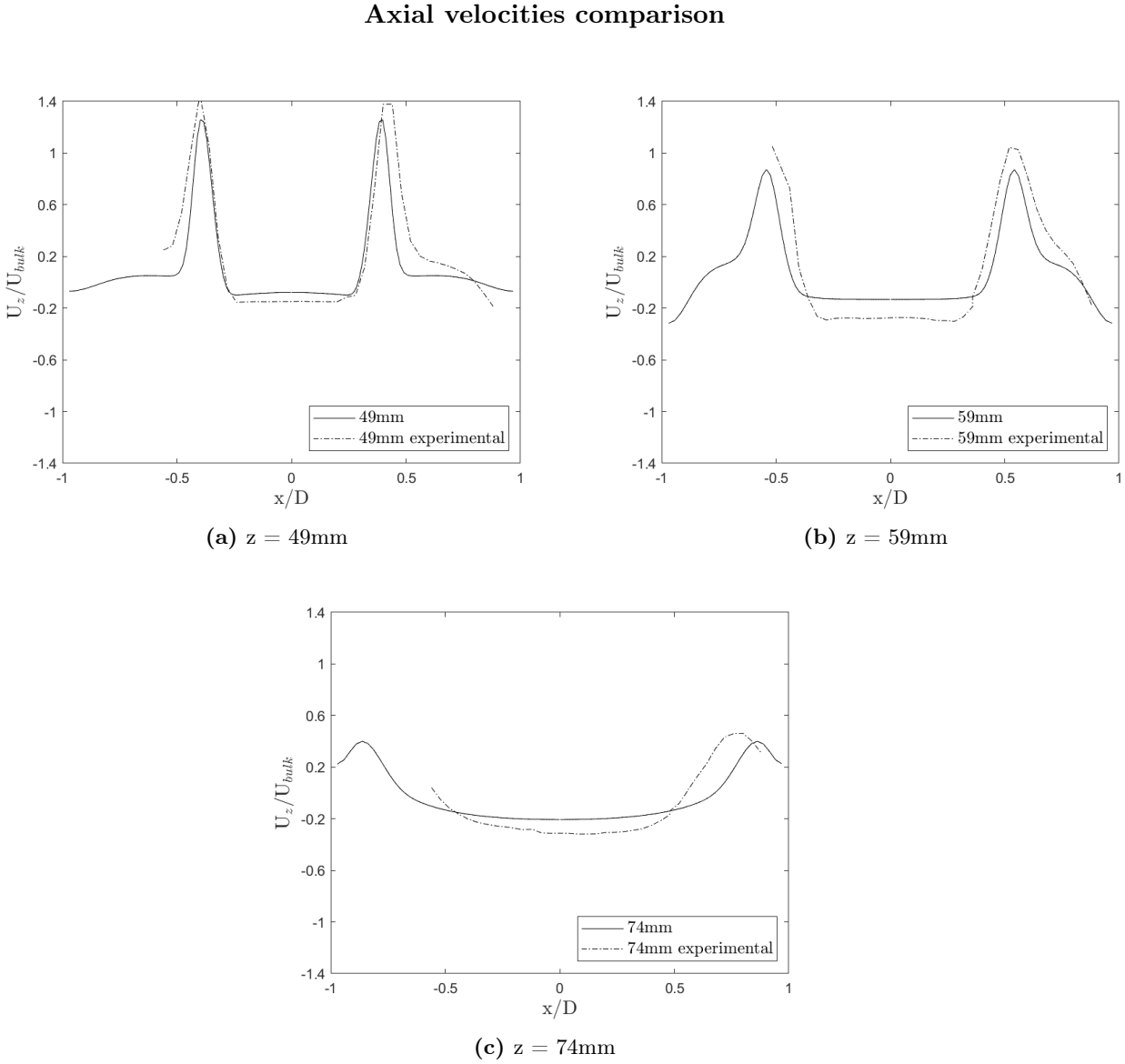

(a) z = 49mm

(b) z = 59mm

(c) z = 74mm

Figure 4.12: Comparison between experimental and numerical results of the axial velocities for the cold gas case C1.

4.2 Reacting simulations: Heptane (H1S1)

4.2.1 H1S1: One step chemical reaction

In this section, the results obtained for the case of n-heptane will be shown. The first scenario is the one-step case, in which no chemical mechanism is used and the reaction occurs from left to right in a single step. The simulation for this case has been conducted until 0.24 seconds.

Species mass fraction

The first thing to study is the mass fractions of the species involved in this reaction. As mentioned before, the reactants are heptane and oxygen, while the products are carbon dioxide and water vapour. Nitrogen, an inert gas, has also been taken into account.

The first aspect to examine is the mass fraction of the fuel, in this case, heptane (figure 4.13a).

The highest amount of heptane is located precisely in the region where the fuel is injected, as expected, while in the rest of the combustor, the amount of fuel is negligible. In fact, the edges of the flame can subtly be seen, where there still exists a slight (almost zero) concentration of heptane. This flame will be better observed in subsequent results. The absence of additional fuel throughout the combustor indicates that everything is being consumed within the flame, suggesting that there is no unburned fuel remaining (at this time).

Regarding the mass fraction of oxygen (figure 4.13b), an opposite behaviour is observed. In the fuel injection zone, the oxygen is at a minimum, and the oxygen injection zone can be clearly identified. The mass fraction of oxygen remains nearly constant in the rest of the burner.

This flame structure is typically that of a diffusion flame. At the flame front, which is the visible region separating the outer and inner zones, the mass fraction of oxygen and fuel is almost negligible. Outside the flame front, the mass fraction of oxygen is at its maximum, and the fraction of fuel is zero. Finally, within the flame front, the mass fraction of fuel is at its maximum, and the fraction of oxygen is zero.

Reactants mass fraction

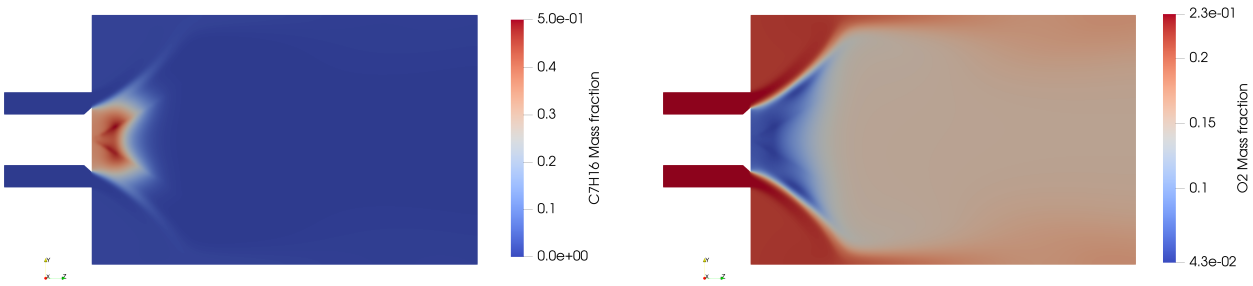

(a) C_7H_{16} **(b)** O_2

Figure 4.13: Mass fraction of reactants for the one step heptane case.

The flame front, therefore, acts as a sink for fuel and oxygen and a source of products. As seen in figures 4.14b and 4.14a, it is at this flame front where the mass fraction of products is at its maximum.

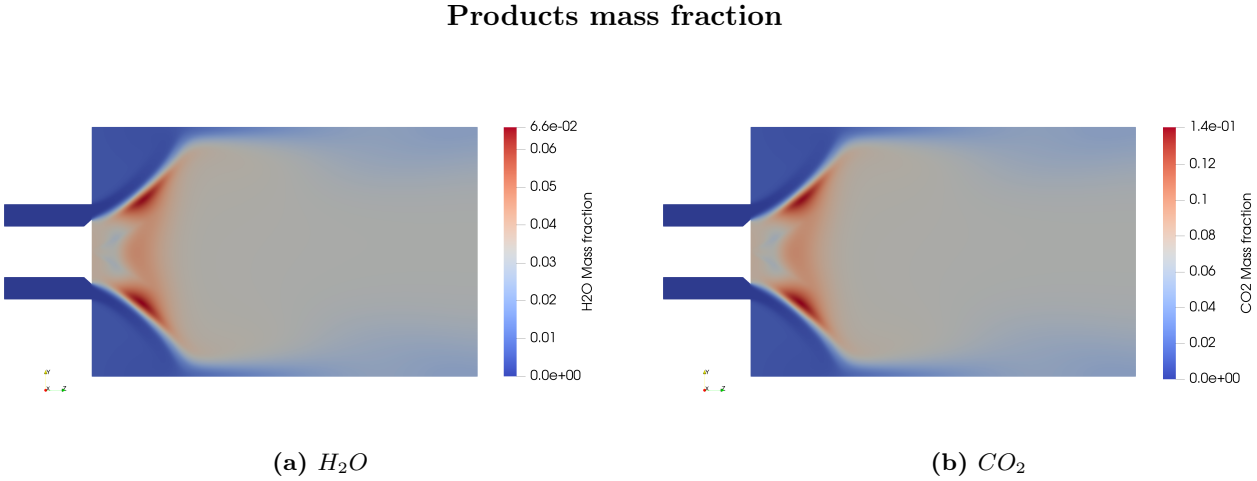

(a) H_2O **(b)** CO_2

Figure 4.14: Mass fraction of products for the one step heptane case.

The inert gas, nitrogen (Figure 4.15), has a minimal mass fraction within the flame front. The mass fraction will increase as it approaches the flame (from the centre outwards) and then remains constant through the combustor. The behaviour of the inert gas (N_2) is completely opposite to that of the fuel.

Figure 4.15: Inert gas mass fraction for the one-step heptane case.

This flame structure can be observed more clearly in the figures 4.16a, 4.16b and 4.16d. The reaction zone or flame front acts as a fuel sink and a source of products. Oxygen is almost absent within the flame front. While moving along the longitudinal axis of the burner, it is possible to observe that the mass fraction of fuel increases slightly before decreasing. The behaviour is nearly identical for all three figures, but it can be noticed that as the z-coordinate increases, the flame will diminish until the reactive zone disappears.

Flame structure

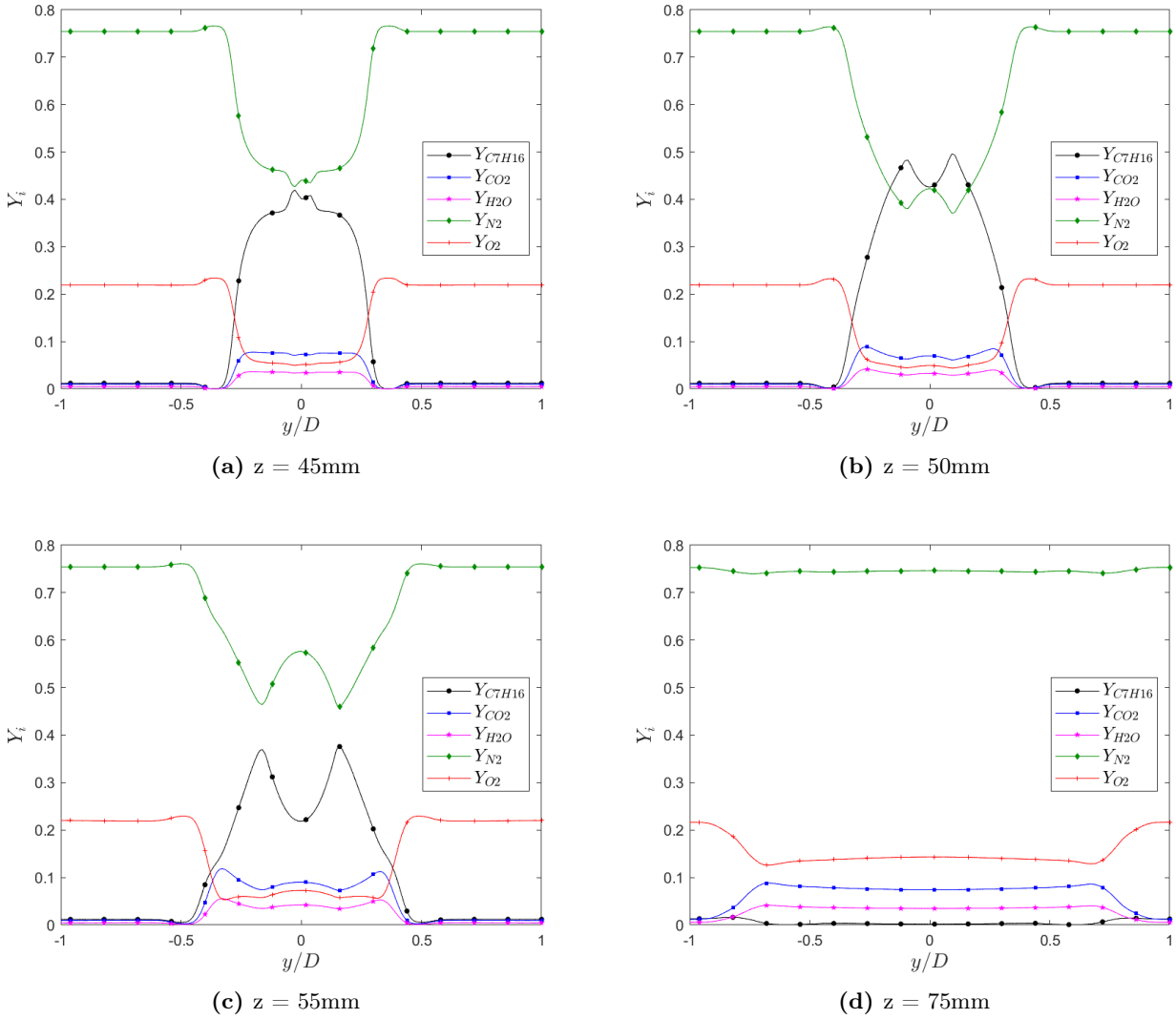

(a) z = 45mm

(b) z = 50mm

(c) z = 55mm

(d) z = 75mm

Figure 4.16: Mass fractions for different Z normal surfaces along the burner.

Temperature field

The temperature field is shown in the Figure 4.17. The maximum temperature is located at the flame front, as expected, reaching around 2100 K.

In this temperature field, it is possible to clearly distinguish the cold oxygen entering the chamber and the cold fuel injection cone. The temperature of the hot gases downstream of the flame ranges between 1000 and 1500 K.

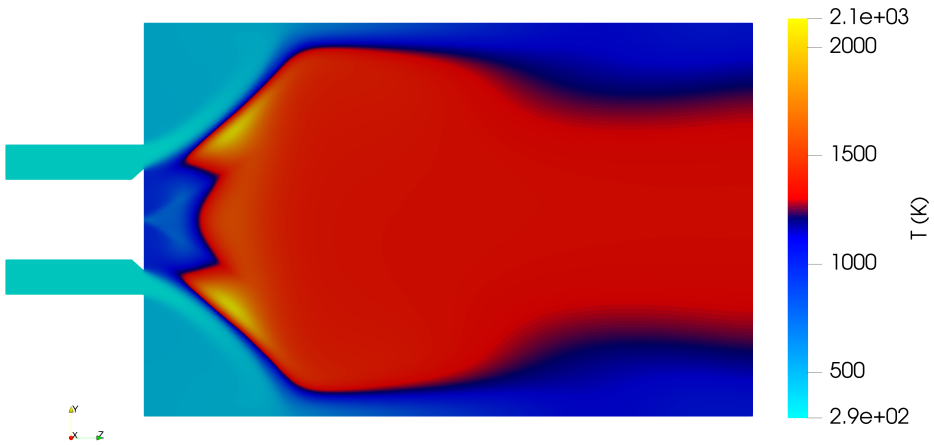

Figure 4.17: Temperature field for the one-step heptane case.

Velocity field

Regarding the velocity, a very similar behaviour to the cold gas cases can be observed. In this instance, the fuel injection cone is also visible in the velocity field.

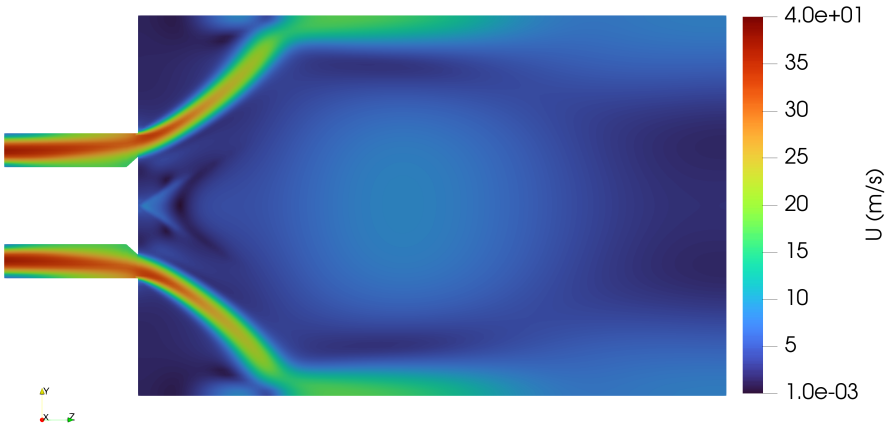

Figure 4.18: Velocity field for the one-step heptane case.

When analyzing the recirculation zones in the Figure 4.20 and Figure 4.19, it can be observed that they are practically the same. However, due to the presence of the fuel and its injection, a Merging Recirculation Zone (MRZ), also known as a Wake Recirculation Zone (WRZ), can be seen in the area near the cone.

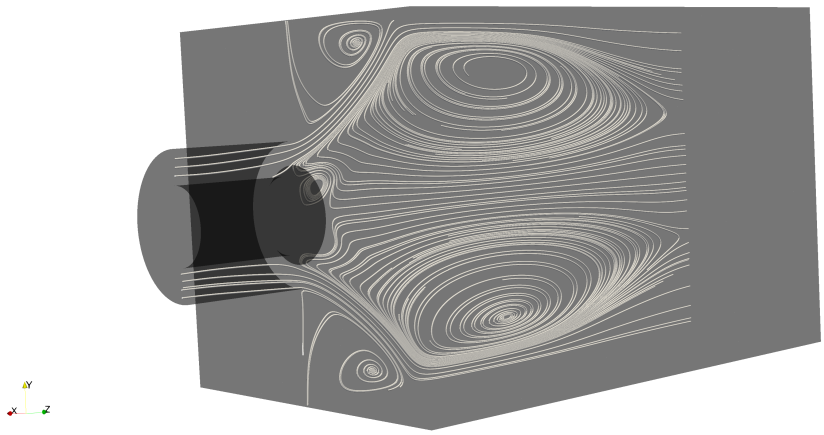

Figure 4.19: Velocity streamlines in a Y normal slice for the one step heptane case.

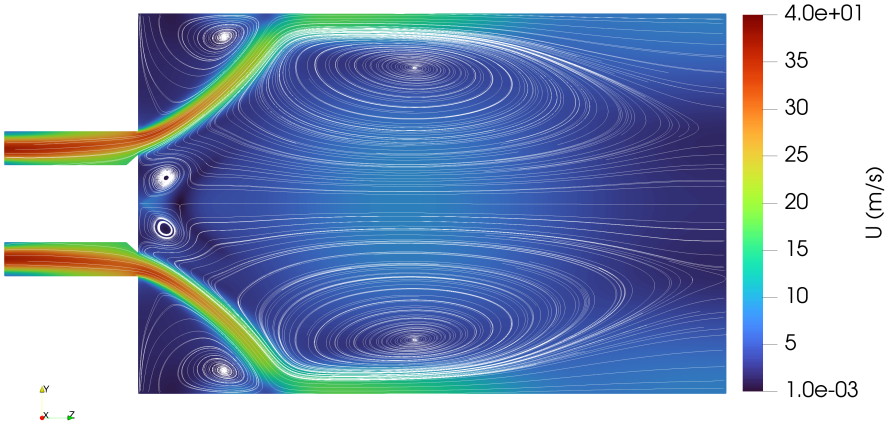

Figure 4.20: Velocity streamlines within the velocity field for the one-step heptane case.

Density field

The density field is observed in the Figure 4.21. It can be seen how the oxygen is introduced into the burner with an atmospheric density at sea level, around 1.2 (kg/m^3). The fuel cone can be identified, as well as the reaction zone. Downstream, the density maintains a nearly constant value.

Figure 4.21: Density field for the one-step heptane case.

Reaction rate

The reaction rate quantifies the progress of the reaction, or equivalently, the rate of change of species. This value will help identify how much heat release is occurring. If this value is displayed along the length of the burner (Figure 4.22), the boundaries of the reaction zone can be perfectly identified, and the flame is observed. In the coloured zones is where the reaction is taking place.

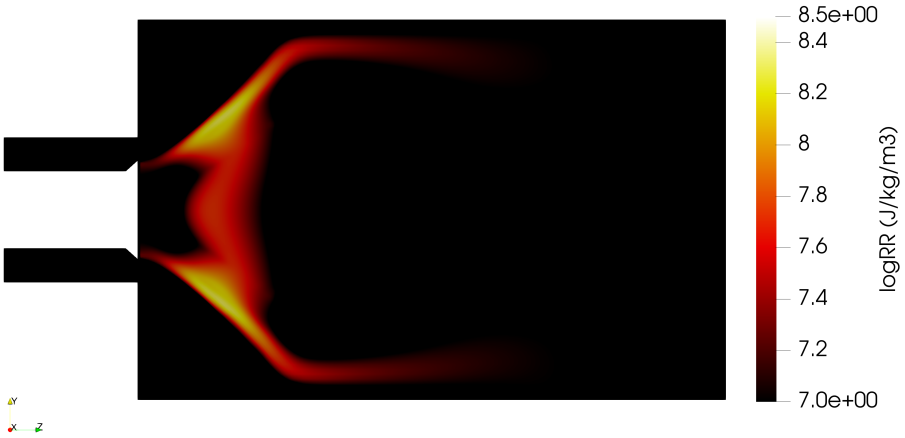

Figure 4.22: Reaction rate for the one-step heptane case (logarithmic scale).

EDC

As explained earlier, the EDC considers combustion to occur where dissipation takes place. Furthermore, this factor is directly proportional to the production rate. If the EDC is displayed along the longitudinal axis of the burner (Figure 4.23), it can be observed that this factor reaches maximum values precisely where the reaction is occurring and approaches nearly zero in the other areas.

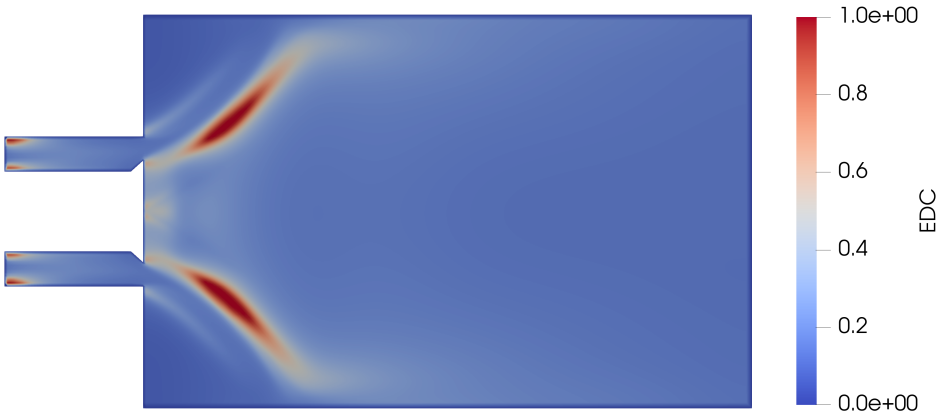

Figure 4.23: Eddy Dissipation Concept (EDC) for the one step heptane case.

Droplets analysis

The fuel is injected in liquid state into the combustion chamber. This makes the simulation of the multiphase type. The fact that there are more than one phase means that the behaviour of these droplets must be taken into account. When a fuel is injected as a spray, its atomization and subsequent vaporization are crucial for combustion to occur.

Atomization is the process by which the fuel jet will break into tiny droplets that will become smaller and smaller until the droplet regime is very dilute. Atomization occurs due to the interaction between the liquid and the surrounding air. When the droplets are small enough, their vaporization takes place. As mentioned earlier, the distribution of these droplets can be approached statistically. Specifically, in this simulation, the Rosin-Rammler distribution is used.

In the Figure 4.26, the fuel droplets can be observed, which have been scaled with a factor of ten times their diameter for proper visibility. These droplets can be represented based on diameter, which, as evident, decreases along the longitudinal axis of the burner and as they move away from the injector. This reflects the fuel atomization discussed earlier. It is also observed that there is a decreasing concentration of droplets in the region, indicating that the droplets eventually reach a very dilute regime.

Furthermore, they have also been colour-coded based on their diameter size, allowing the magnitudes of these droplets to be observed. The largest droplets are on the order of tenths of millimetres, while the smallest ones are in the range of thousandths of millimetres.

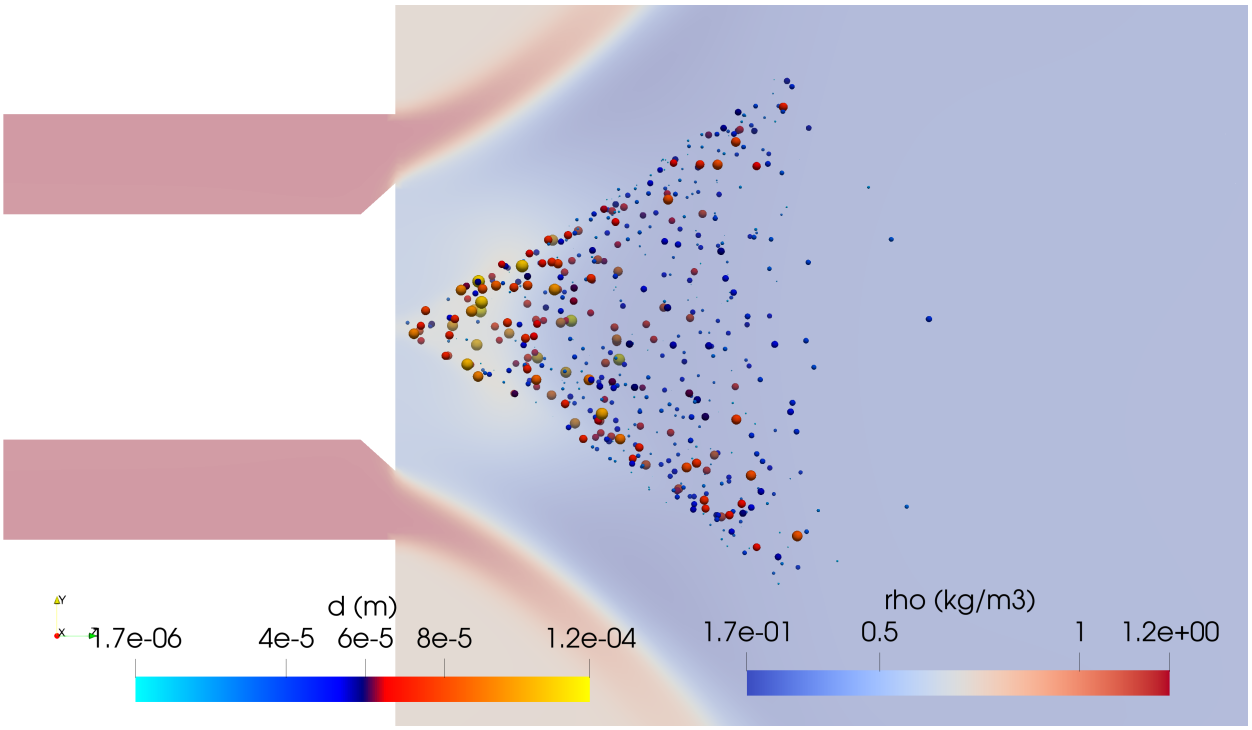

Figure 4.24: Droplets diameter within fuel mass fraction. Droplets scale= $10 \cdot d$.

Another interesting variable to analyze is the temperature of these droplets. As shown in the Figure 4.25, the droplets heat up until they reach a temperature around 370 K . This is due to the vaporization discussed earlier. The liquid state of the fuel cannot exist below a certain temperature at a specific pressure, which is known as the boiling temperature. The operating conditions of the burner are at 1 atm. At this pressure, the boiling temperature of heptane is around 370 K.

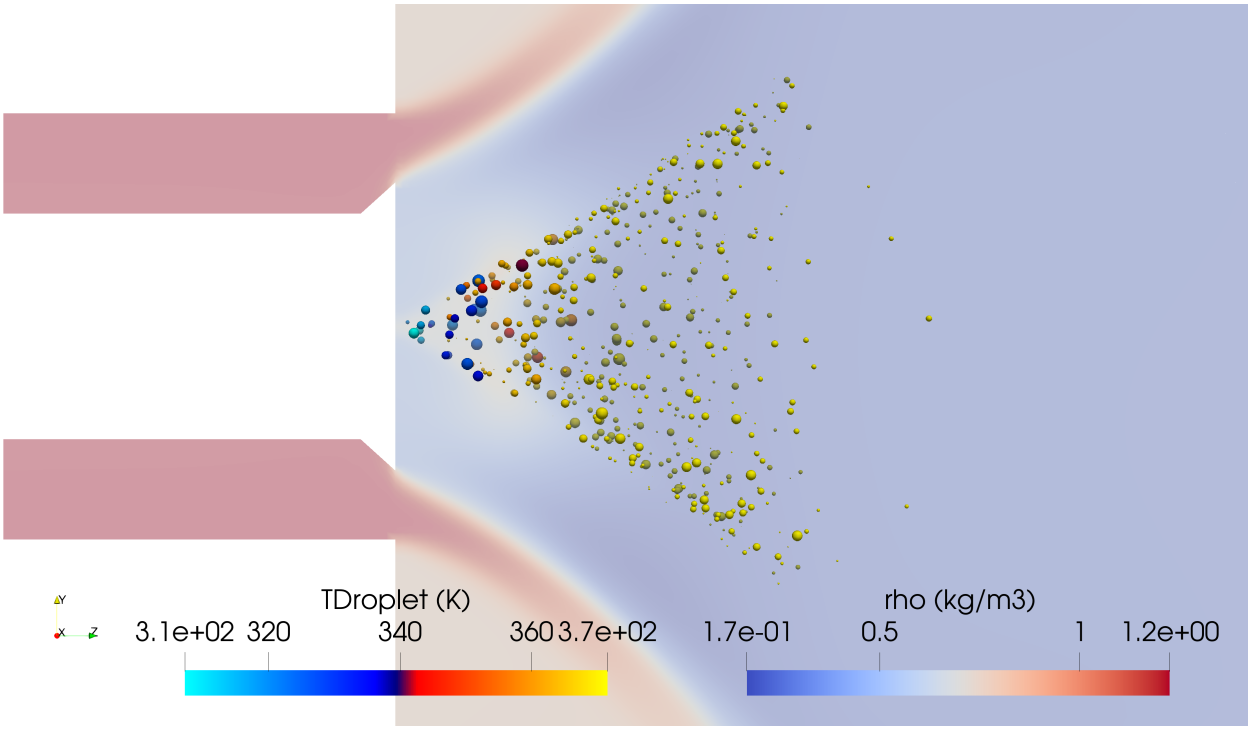

Figure 4.25: Droplets temperature.

Lastly, the droplet evaporation rate is presented in the figure. It can be observed that when the droplets are very close to the injector, the evaporation rate is zero. In this zone, the droplets are very large and too cold to begin evaporating. Atomization is important because the rates of mass and heat transfer between the liquid and gas phases increase as the exposed area between phases increases. Therefore, if the liquid jet breaks into small fragments in such a way that the total area of these fragments is much larger than the original area, the vaporization will be greater. As the droplets become smaller and the temperature increases, the evaporation rate ceases to be zero.

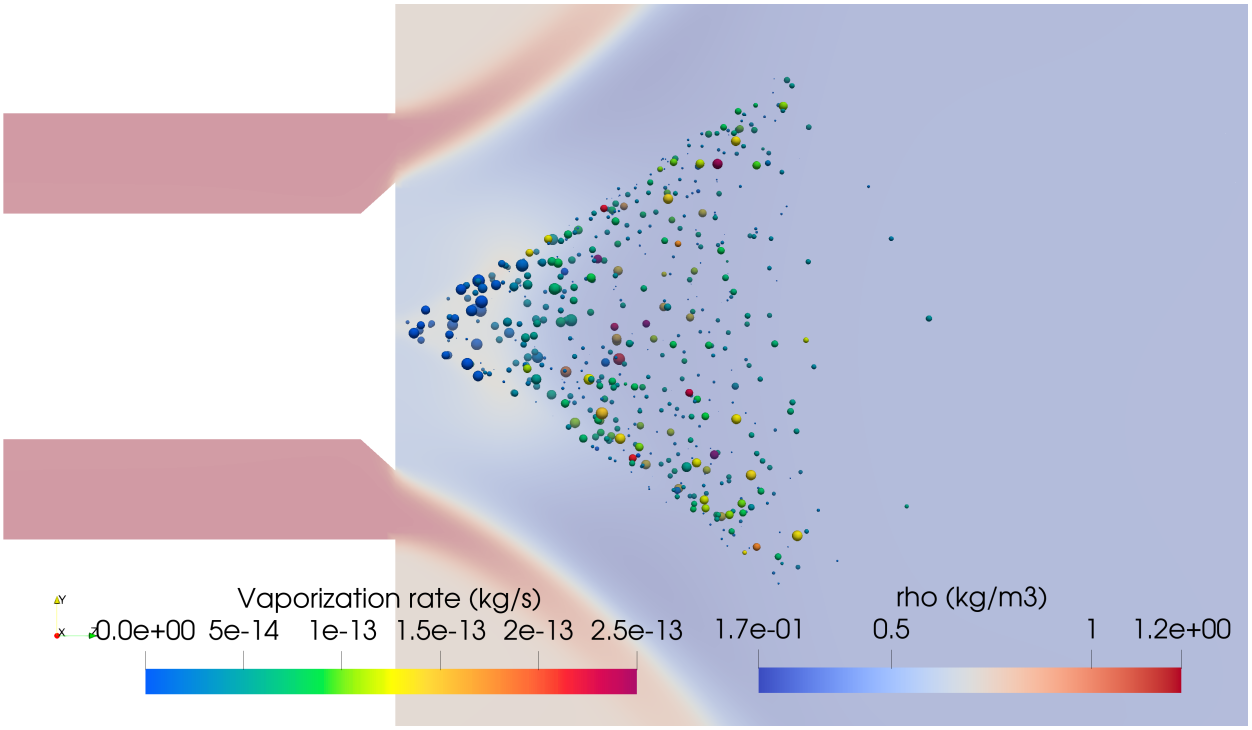

Figure 4.26: Vaporization rate of droplets. Droplets scale= $10 \cdot d$.

Temporal evolution

Studying the temporal evolution of the single-step case is interesting to understand how the simulation progresses, the stability of the flame and the process of combustion.

First of all, the reaction rate is analyzed for different moments in time in the Figure 4.27. As previously mentioned, the reaction rate shows the edges of the flame, that is, where the reaction is taking place. It can be observed that initially (0.01 s), the flame is confined to the first third of the combustor, and then it gradually moves towards about two-thirds of it. Furthermore, in the early moments, the flame is characterized by brighter edges and a more intense reaction, and the intensity of the reaction decreases as time progresses.

At 0.02 seconds, it can be observed that the reaction retreats almost towards the injector, although there is still an area without reaction where the fuel injection cone is visible.

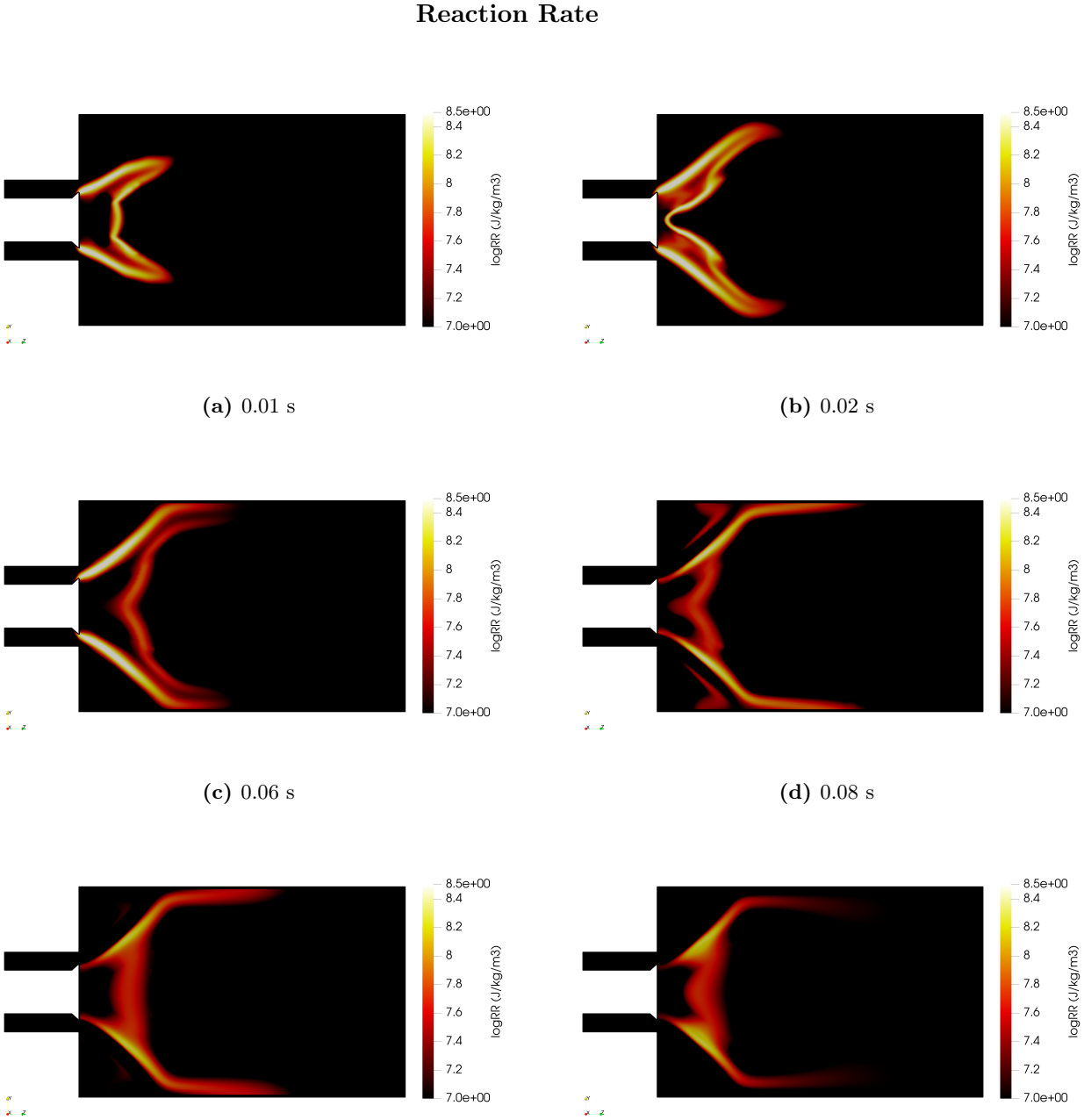

(a) 0.01 s

(b) 0.02 s

(c) 0.06 s

(d) 0.08 s

(e) 0.10 s

(f) 0.24 s

Figure 4.27: Reaction Rate for different time instants for the one-step heptane case.

It is also interesting to analyze the evolution of temperature (Figure 4.28) at different moments in time, as shown in the figure. Thanks to this image, it is possible to explain how combustion is simulated in the OpenFOAM case.

To simulate the combustion process, a process similar to ignition is carried out. Initially, air is injected at around 1200 K, as seen in figures 4.41a and 4.28b, indicated by the dark blue colour. This high air temperature initiates the combustion, as the temperature reaches approximately 2100 K, represented by the yellow colour. These first two images are closely related to the previous reaction rate analysis, where it is possible to observe how the flame grows. In the figure 4.28b it is reflected how the hot combustion products propagate throughout the burner until hot products are

present along the entire length of the burner (figure 4.41b). In this last figure, the air injection is still at 1200 K. However, from this moment when ignition has already occurred and combustion is self-sustained, the inlet air temperature is lowered to 288 K, which means cold air. Because the air injection temperature has decreased, the rest of the temperature within the combustion chamber will also decrease gradually, as can be seen in figures 4.28d, 4.28e, and 4.41d.

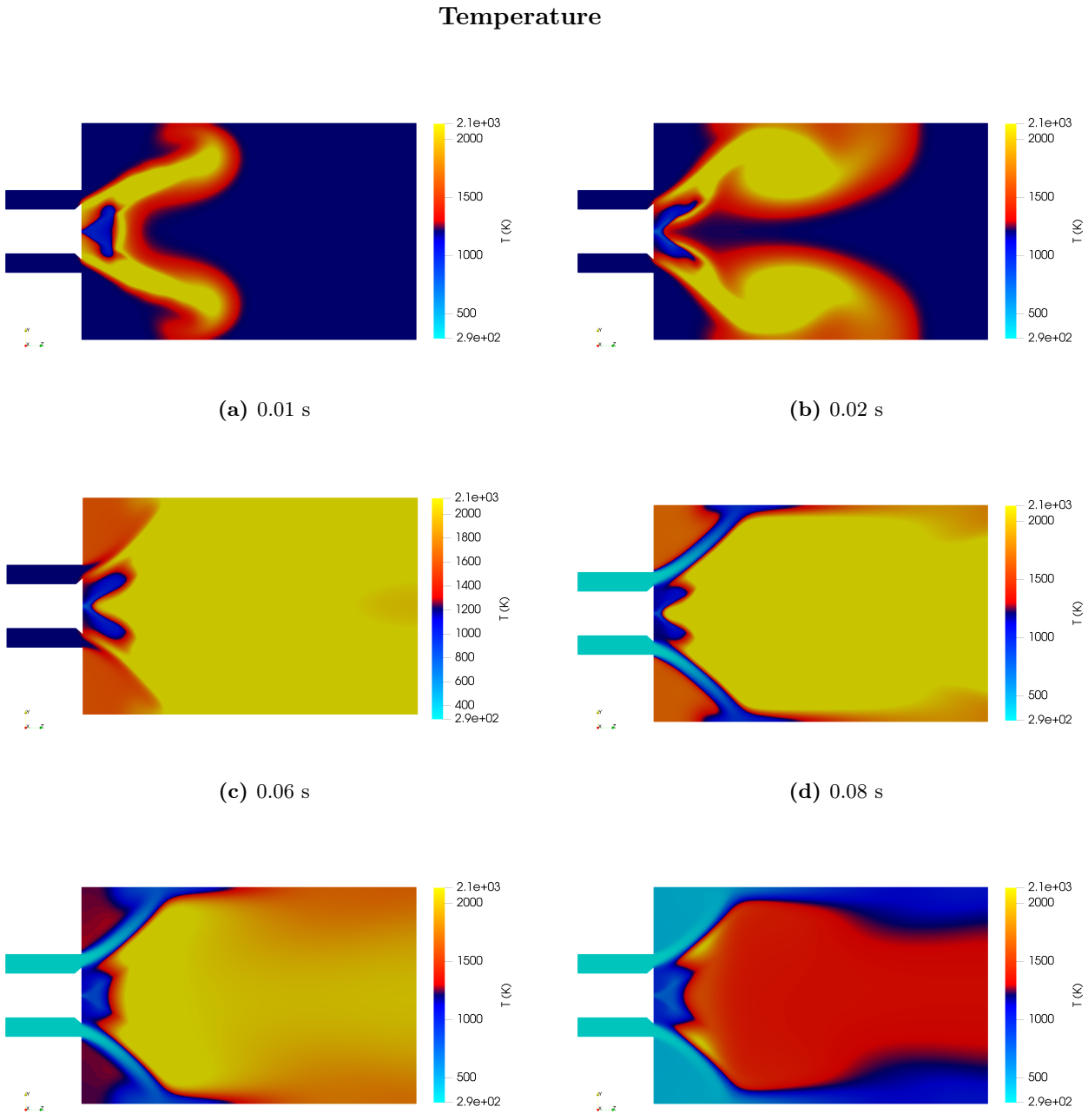

(a) 0.01 s **(b)** 0.02 s

(c) 0.06 s **(d)** 0.08 s

(e) 0.10 s **(f)** 0.24 s

Figure 4.28: Temperature field for different time instants for the one step heptane case.

Finally, the evolution of the velocity magnitude can be observed, as well as the streamlines of axial and radial velocity (figure Figure 4.29). In these figures, the formation of the recirculation zones is shown and how they move downstream of the combustor, ultimately resulting in the distribution that has been analyzed earlier. What is certain is that recirculation zones identified throughout the

study appear at all moments.

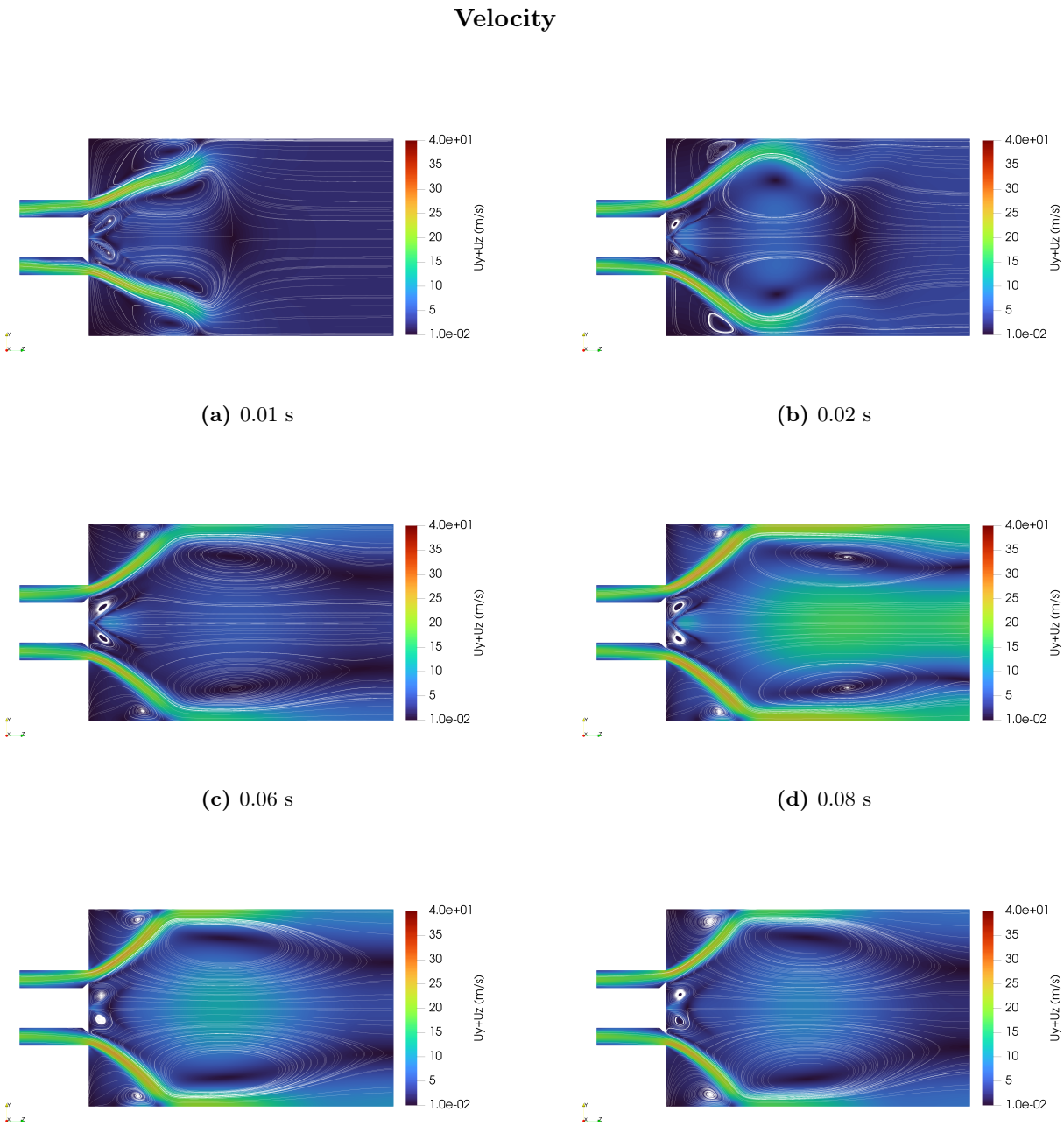

(a) 0.01 s

(b) 0.02 s

(c) 0.06 s

(d) 0.08 s

(e) 0.10 s

(f) 0.24 s

Figure 4.29: Velocity field with streamlines (radial and axial) for different time instants for the one step heptane case.

4.2.2 H1S1: CERFACS chemical mechanism

Once the simulation of a step for heptane has been completed, a chemical mechanism is employed in which, as explained earlier, the combustion process is represented in a more realistic manner by taking into account certain reactions and intermediate species. Therefore, in this case, the simulation starts from the last simulated time in the one-step reaction (0.24 s) to observe whether the selected chemical method accurately represents the flame. This is a common approach when addressing chemical simulations. A one-step case is previously simulated to obtain a sustainable simulation and a flame which is useful as a trigger for the chemical mechanism.

Results

The last simulated time using this mechanism is 0.2538 seconds. The following results are of primary interest for the case study.

The temperature can be observed in the Figure 4.30, and as evident, this distribution is very similar to what had been calculated in the one-step case for 0.24 seconds. In this figure, it can be seen that downstream of the flame, the temperature in the combustion product zone is lower than in the one-step reaction case. A lower temperature compared to the one-step case is to be expected. When simulated with a single step, the adiabatic temperature is usually over-predicted, this is because species and intermediate reactions that tend to absorb heat are not considered. In addition, dissociation reactions may also appear, increasing the endothermic character of the overall reaction.

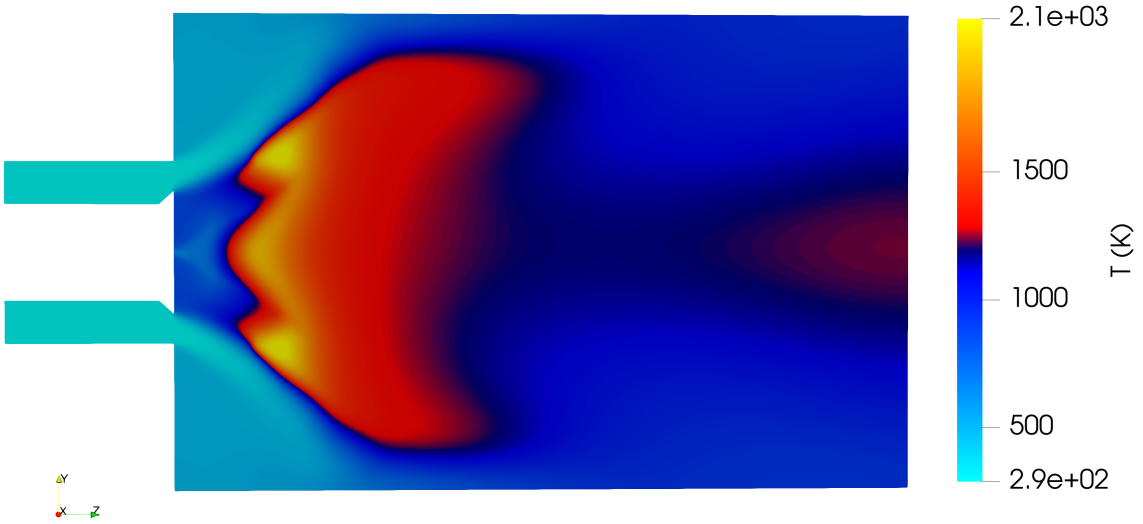

Figure 4.30: Temperature field with the CERFACS mechanism for the heptane reacting case. (time=0.2538s)

On the other hand, the velocity field (Figure 4.31) and its recirculation zones are the same as in the previous case, where once again, it can be identified a Central Toroidal Recirculation

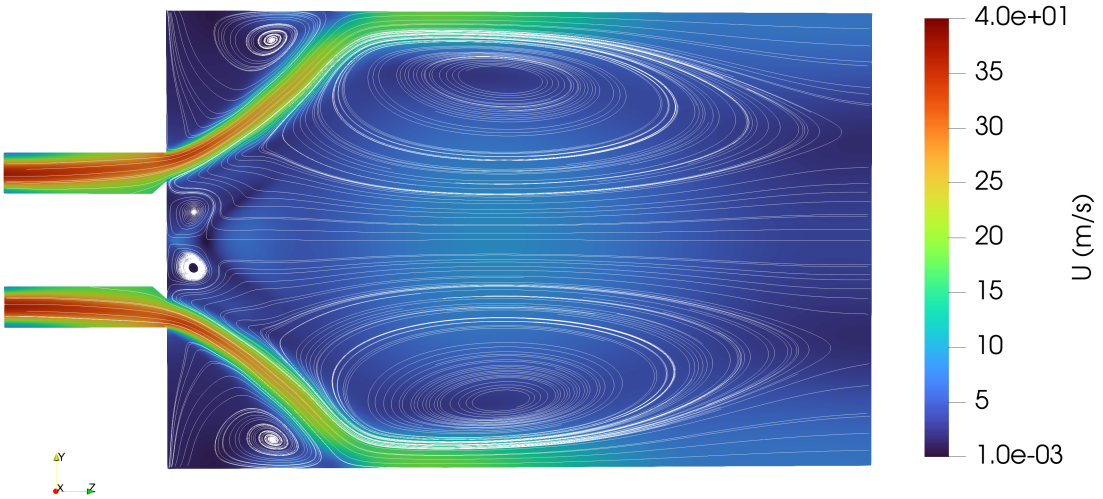

Figure 4.31: Velocity field with the CERFACS mechanism for the heptane reacting case with streamlines for the radial and axial velocity. (time=0.2538s)

Zone (CTRZ), a Corner Recirculation Zone (CRZ), and near the fuel injection point, the Merging Recirculation Zone (MRZ). Furthermore, the absolute velocity values are also the same.

With the reaction rate (Figure 4.32), it's possible to observe the flame's reaction zone and, therefore, its contour. Two main observations can be made when comparing it to the previous case. The flame has a similar shape but is detached from the injector, which is the phenomenon known as lift-off. On the other hand, the flame exhibits a more pronounced "M" shape, and the reaction rate is slightly higher at its edges, making it appear brighter. The reaction rate is more intense because the intermediate reactions release heat, this is not considered in the previous case of one-step.

When comparing the results of the RR with the velocity, it becomes clear that where the flame occurs the velocity ranges between 0 and 10 m/s. It has already been explained in previous chapters that for the combustion of a hydrocarbon to occur, the speeds cannot be very high. The recirculation zones and the presence of the bluff body help to lower the speed.

When using a chemical mechanism, in this case one developed by CERFACS, in addition to the combustion products that appeared before (CO_2 and H_2O), all the intermediate products that can be of interest both for understanding the true combustion reaction and for pollution-related reasons appear. One of the main causes of pollution includes these intermediate products that are not completely consumed due to incomplete fuel combustion and are then expelled into the environment.

In the Figure 4.33, two of these intermediate products can be observed, as well as water vapour and carbon dioxide. OH is incorporated because it plays a crucial role as a radical species in chain-branching reactions that are essential for maintaining the flame. On the other hand, CO serves as an indicator of incomplete combustion and tends to accumulate under conditions near extinction and during extinction transients. Hence, as evident, the OH mass fraction accurately delineates the flame's boundary and will be employed for this purpose experimentally in the subsequent steps.

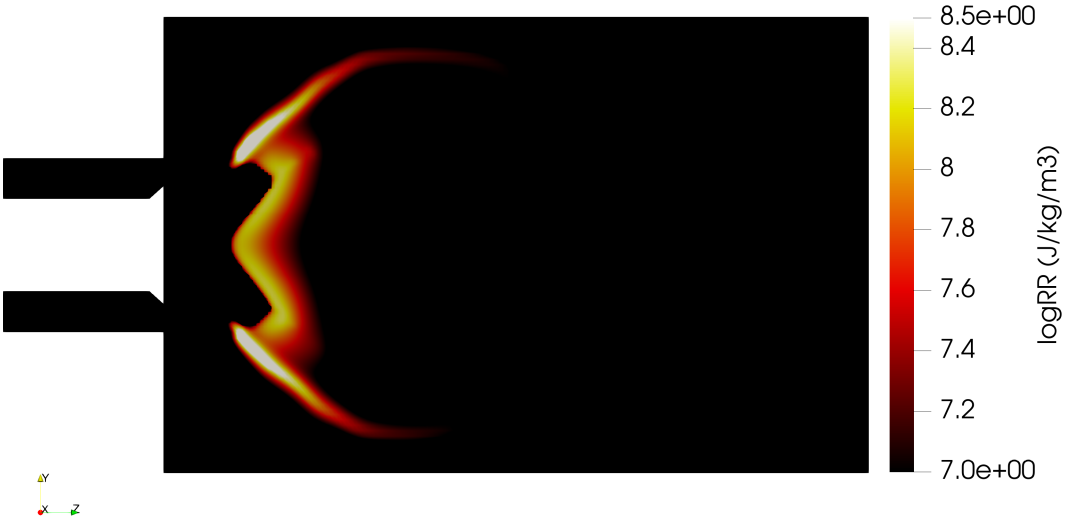

Figure 4.32: Reaction Rate with the CERFACS mechanism for the heptane reacting case with a logarithmic scale. (time=0.2538s)

The intermediate products are only present in the flame zone, while water vapour and carbon dioxide appear throughout the combustor, with the latter being the most abundant. The fact that carbon monoxide and hydroxide only appear in this zone indicates that combustion is nearly complete. This can also be observed in other intermediate products shown in the Figure 4.34.

Other than the species mentioned above, there are additional ones of special interest, including acetylene (C_2H_2), which is a soot precursor, studied due to the impact that its emission has. Additionally, formaldehyde (CH_2O) is a marker of incomplete combustion. If mass fractions of some species are plotted along the longitudinal axis, the Figure 4.35 is obtained. In Figure (b) some of the species shown in Figure (a) are shown with another rank axis ordered. Furthermore, this representation is interesting because it allows to observe the displacement of the flame.

The species that have the highest concentration are carbon monoxide, followed by ethylene (C_2H_4) and acetylene, but they are quickly depleted. Almost all species are significant between 40 and 80 mm, which is identified as the zone of intermediate reactions.

With all of the above mentioned, it can be confirmed that combustion occurs completely, with no production of soot under the conditions studied. This is positively contributed by the type of injection used and the swirl movement. Furthermore, it indicates that the atomization and evaporation process of heptane droplets occurs effectively.

As an additional comment, the temporal evolution of these mass fractions of species that provide information about incomplete combustion could be graphed. However, this information is not reliable because the starting point of this simulation is the one chemical step case, as explained above. In the one-step simulation, the intermediate species do not appear, so as soon as the simulation with the chemical mechanism begins, their mass fractions keep growing. This result would give a false sensation that combustion is less efficient over time, which is not true. Furthermore, the time simulated with the chemical mechanism is not large enough for this study to be significant.

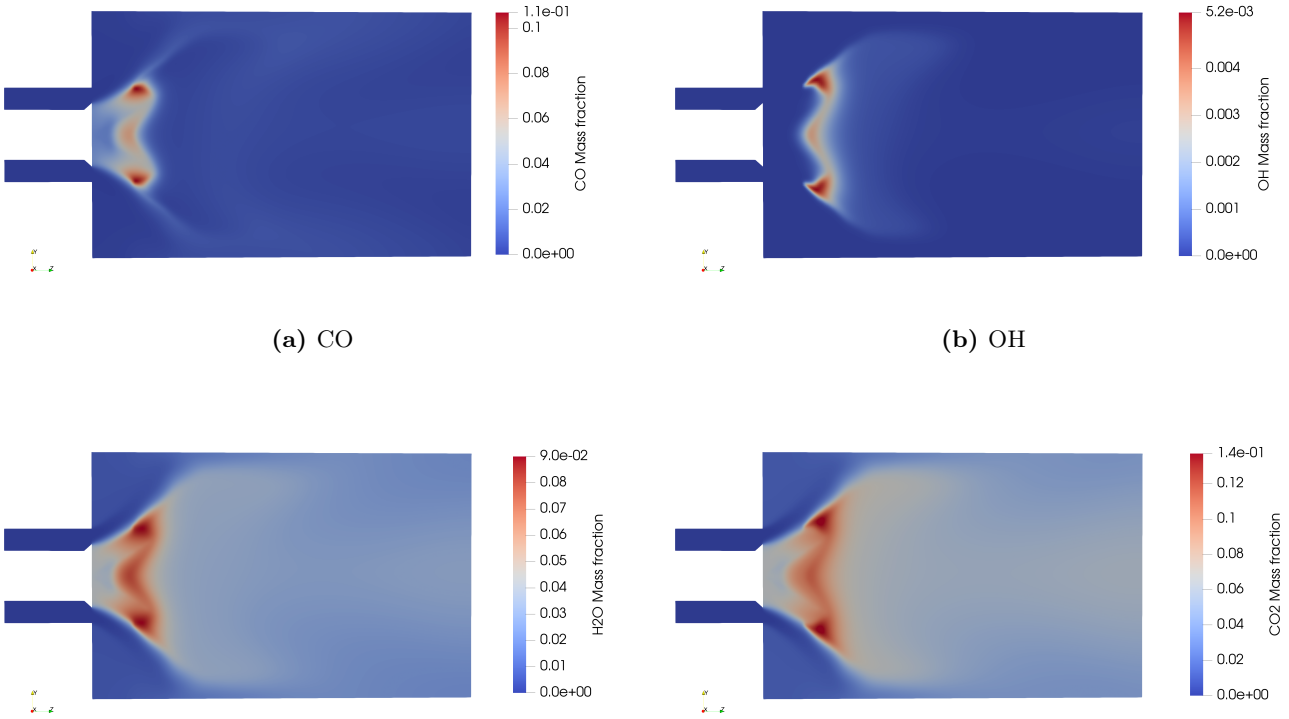

(a) CO **(b)** OH

(c) H_2O **(d)** CO_2

Figure 4.33: Major combustion products with the CERFACS mechanism for the heptane reacting case. (t=0.2538s)

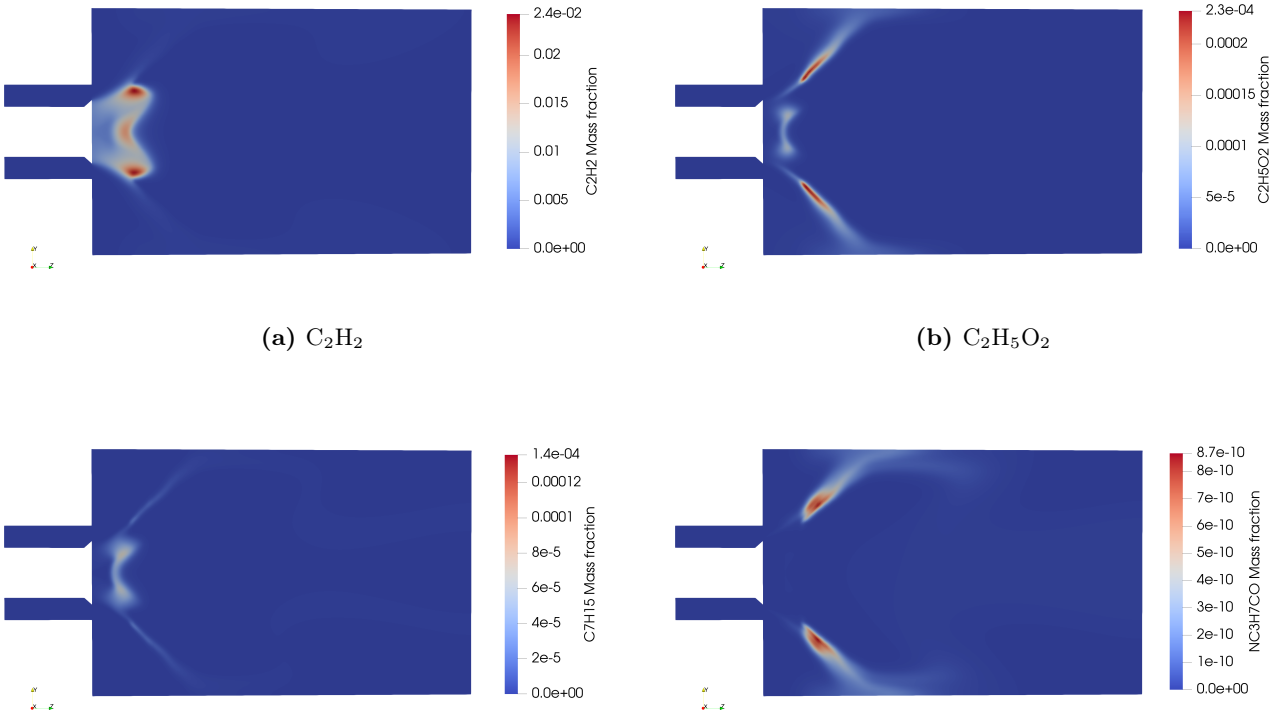

(a) C_2H_2 **(b)** $C_2H_5O_2$

(c) C_7H_{15} **(d)** NC_3H_7CO

Figure 4.34: Intermediate combustion products with the CERFACS mechanism for the heptane reacting case. (t=0.2538s)

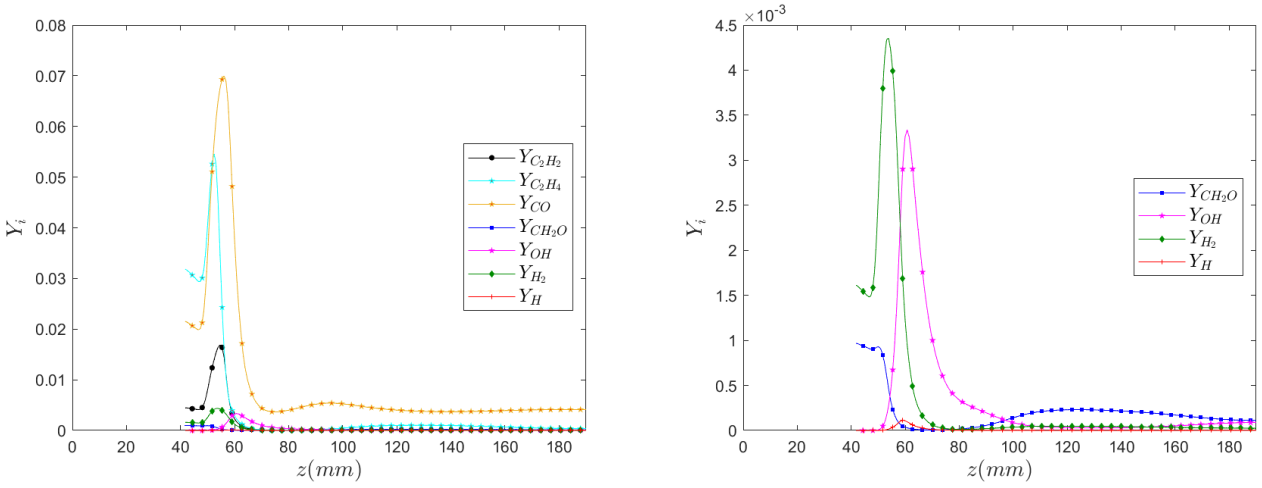

(a) **(b)**

Figure 4.35: Mass fraction of some species along the longitudinal axis of the burner. (t=0.2538s)

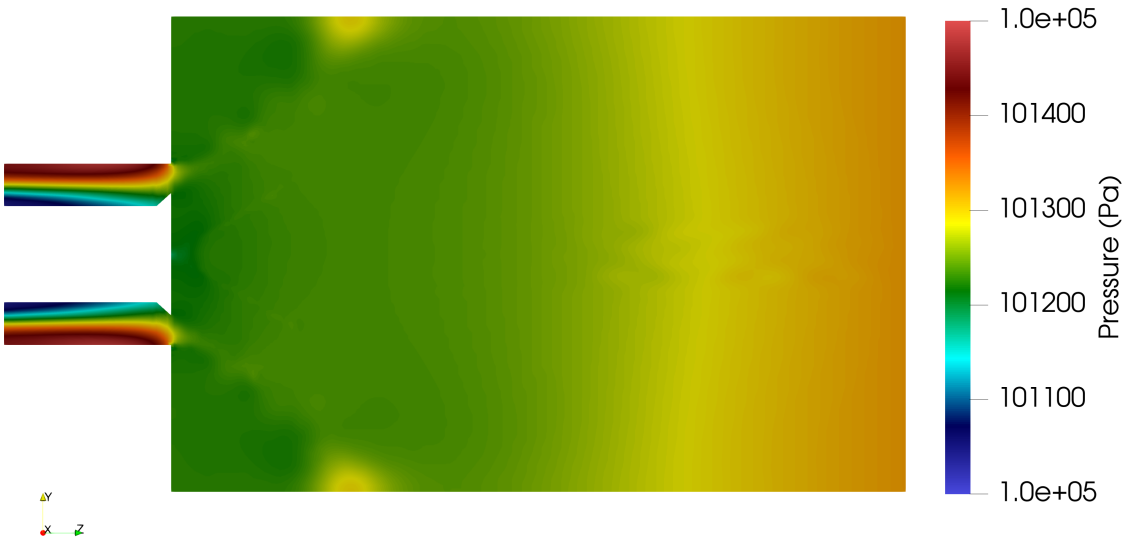

Figure 4.36: Pressure field with the CERFACS chemical mechanism for the heptane reacting case. (t=0.2538s)

In the Figure 4.36, the pressure field along the burner can be observed. In the setup chapter, it has been mentioned that outside the control volume of the burner, the pressure has been defined with the atmospheric value (101325 Pa). Within the burner, it is the transport equations that calculate its value. In the figure, slight pressure gradients can be identified. Towards the end of the combustor, the pressure increases slightly, also at the edge that separates the Corner Recirculation Zone (CRZ) and the Central Toroidal Recirculation Zone (CTRZ). The pressure values are expected, their low variation is attributed not only to combustion but also to the swirl phenomenon. There can be no recirculation zones without pressure gradients.

Comparison with the experimental results

In this section, the results will be compared with those obtained experimentally through the University of Cambridge, as this is one of the main objectives of this project. This data includes axial velocities and the Sautter Mean Diameter (SMD) obtained using the Phase Doppler Anemometer (PDA) method, which is a measurement method that allows the measurement of a statistical distribution and velocity in a flow field.

Other provided measurements include OH* chemiluminescence, Planar Laser Induced Fluorescence (PLIF) of OH, and Mie scattering. These OH distributions serve to represent where the reaction rate is highest or the heat release is occurring. Essentially, they identify where the reaction is happening with the highest intensity. To compare these measurements, both the reaction rate calculated with OpenFOAM and the mass fraction of OH will be used.

In Figure 4.37, the data from the Cambridge repository is displayed, while in Figure 4.38, the data calculated using OpenFOAM and the CERFACS chemical method are presented.

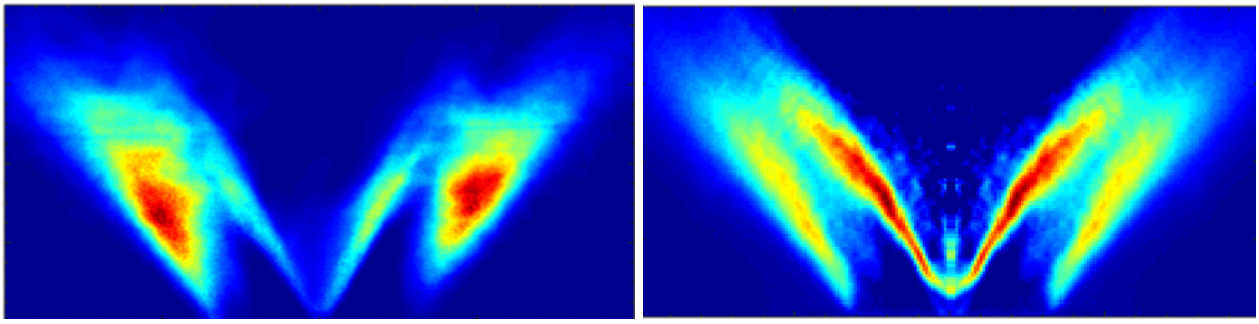

(a) Experimental OH PLIF **(b)** Experimental OH* chemiluminescence

Figure 4.37: Experimental OH measurements obtained through various methods from the University of Cambridge repository. [51] [50]

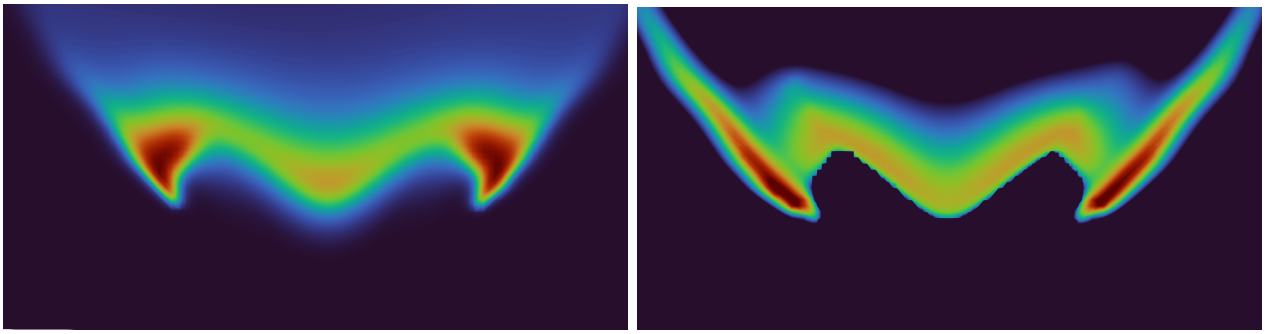

(a) OH mass fraction **(b)** Reaction rate

Figure 4.38: Results obtained using the OpenFOAM software for the reactive case of heptane with the CERFACS chemical mechanism. The reaction rate is shown on a logarithmic scale.

When comparing both figures, several observations can be made. First of all, the flame's morphology is accurately represented. It can be observed that the flame exhibits an **"M" shape**.

The shape that flames take depends on various factors, including the injector, geometry, thermodynamic conditions, flow conditions, and the injected reactants' properties. Flames with swirl motion, as in the case of this study, often stabilize into a V or M shape due to these recirculation flows. As mentioned throughout this project, swirl flows create a recirculation zone in the corners called the Corner Recirculation Zone (CRZ). Additionally, an inner recirculation zone is also formed, referred to as the Central Toroidal Recirculation Zone (CTRZ) or Inner Recirculation Zone (IRZ). These two recirculation flows contribute to flame stabilization.

The region of the flame in contact with the IRZ is known as the Inner Shear Layer (ISL), while the portion in contact with the corner recirculation zone (CRZ) is the Outer Shear Layer (OSL). An M-shaped flame is one that has a reaction layer stabilized in the ISL and has a protruding tip that extends into the OSL.

The Figure 4.39 helps to illustrate the ideas explained earlier.

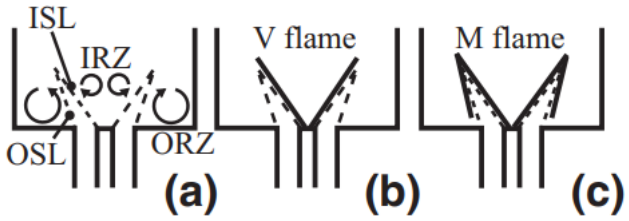

Figure 4.39: (a) Schematic of a swirled jet flow in a combustion chamber with its inner (ISL) and outer (OSL) shear layers and the inner (IRZ) and outer (ORZ) recirculation zones. (b) V flame. (c) M flame. [18]

Another observation from the comparison between experimental data and the results obtained through OpenFOAM is that the flame is not anchored to the injector region; it is separated downstream. This phenomenon is known as **"lift-off"** and is also a subject of study. It is evident that this has occurred due to the chemical mechanism used by CERFACS, as in the one-step analysis, the flame was indeed anchored.

Because the formation of soot is closely related to the lift-off height, this topic is extensively studied. However, there are only a few studies that specifically address flame lift-off and blow-off for liquid fuel sprays.

The flame lift-off height is the location where the local flame propagation speed matches the velocity of the air-fuel mixture. This particular point is subject to the interplay of various factors, including atomization, vaporization, and chemical kinetics. These processes, in turn, are influenced by the specific operating conditions under examination and the type of fuel being utilized.

As previously mentioned, the chemical mechanism being used is responsible for the separated representation of the flame. In the case of this study, the way kinetics are being treated with this method is very slow, causing reactions to occur at a slow rate, heat release to be slow, and consequently, the flame to move and lift off.

In addition to all of this, the phenomenon is also influenced by the volatility of the fuel. Broadly speaking, larger droplet sizes and fuels with lower volatility tend to result in greater flame lift-off heights. Heptane is considered a high-volatile fuel in comparison to others, such as n-dodecane and n-decane. These along with its smaller droplet size promote improved fuel/air mixing, leading to a greater proportion of localized pre-mixed regions with fuel-lean conditions. Nonetheless, heptane does exhibit the lift-off phenomenon, although it is less pronounced compared to some other fuels. There are prior studies that support these claims, such as [16].

Fuels with low volatility are of particular interest in the aerospace sector as their properties are more similar to those of kerosene. However, in this project, only reactive simulations with n-heptane have been conducted, making it impossible to compare the lift-off height with other fuels.

Therefore, it can be stated that the primary reason for the displaced flame is primarily due to the chemical mechanism used.

Another comparison that can be made thanks to the Cambridge University repository is the axial velocity obtained using the PDA method. The results of this comparison are shown in the Figure 4.40.

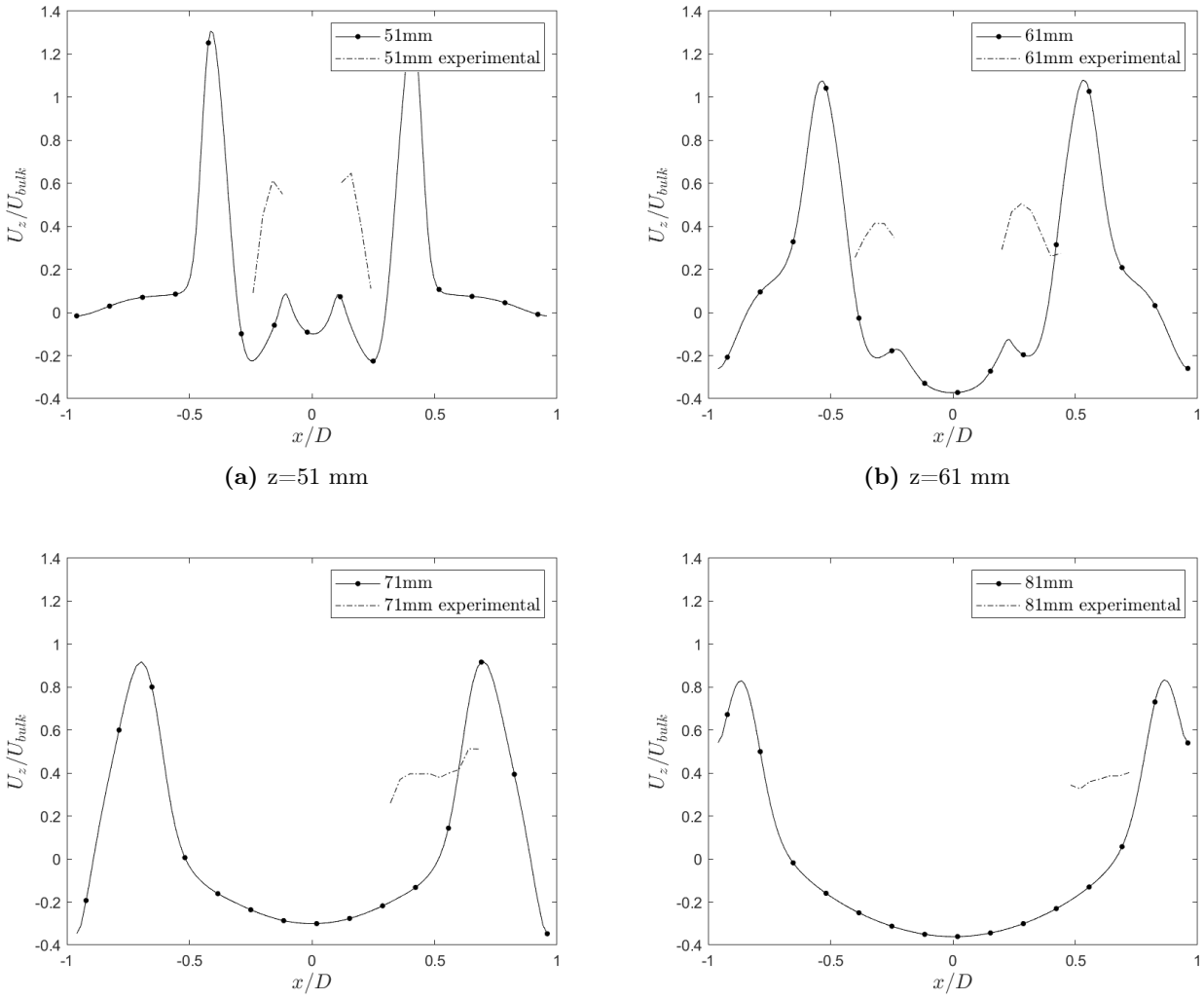

(a) z=51 mm

(b) z=61 mm

(c) z= 71 mm

(d) z= 81 mm

Figure 4.40: Comparison of the axial velocities obtained through OpenFOAM and the experimental data from the Cambridge University repository.

The first observation in this comparison is that there is no correlation between the experimental and numerical results. One of the reasons is that, as mentioned earlier, the flame is separated from the injector in the CFD results, while it is not separated in the experimental data. The comparison is done at the same distance in the z-axis between the two data but in each dataset, a different point of the flame is being observed because the flames are located at different positions along the Z-axis. This makes this comparison not very meaningful. Furthermore, the PDA method is not very reliable for reactive cases.

Another thing that can be observed, for instance, in the case of z=51 mm, is that the velocity peaks in the numerical result are higher than in the experimental data.

This makes sense because, as mentioned earlier, the lift-off phenomenon is closely related to chemical kinetics, and therefore, to velocities, residence times, mixing times, among others. An increase in flow velocity typically results in a higher lift-off height. As the flow velocity rises, the resulting speed propels the droplets directly downstream, thereby shifting the flame's stabilization point, so it can be said that the obtained results align with the occurrence of the lift-off phenomenon.

Temporal evolution

In this case, the temporal evolution is also analyzed, specifically focusing on temperature and reaction rate.

Regarding temperature (Figure 4.41), the main observation is that the region downstream of the combustion products gradually cools. Additionally, the flame takes on a more pronounced "M" shape, with higher temperatures at its edges.

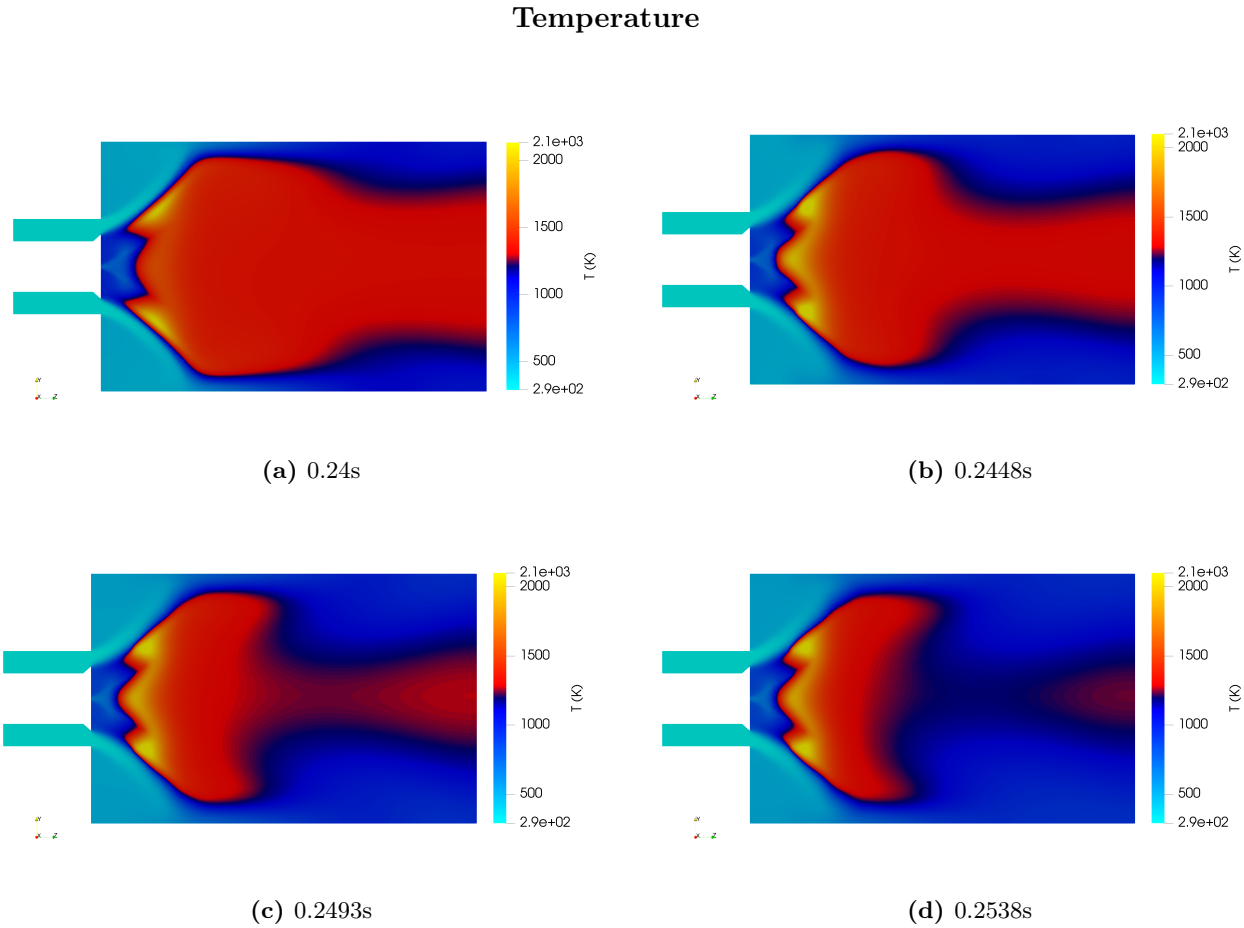

(a) 0.24s **(b)** 0.2448s

(c) 0.2493s **(d)** 0.2538s

Figure 4.41: Temperature field for different time instants with the CERFACS chemical mechanism for the n-heptane reacting case.

Observing the reaction rate (Figure 4.42), it's evident that from the very beginning, the flame becomes completely detached and gradually assumes the "M"-shaped topology mentioned earlier. Additionally, it can be seen that the flame edges recede toward the first third of the combustor, whereas at the initial time (t=0.24s), the flame edges extend roughly to the middle. The reaction occurs more intensely with this mechanism, which is why the flame appears brighter starting from 0.24 seconds.

One of the reasons for analyzing the temporal evolution in this case is to detect instabilities such as blow-off. The lift-off phenomenon mentioned earlier can be a precursor to the well-known blow-off. "Blow-off" occurs when the flow velocity is sufficiently high, causing the flame to be unable to be stabilized or maintained at a fixed location. As a result, the flame propagates downstream and eventually goes out. As can be seen in the Figure 4.42, in the case under study, the flame position remains constant around the longitudinal axis of the combustor. Therefore, it is evident that the

blow-off phenomenon is not going to occur, and the flame is simply separated due to the reasons studied earlier.

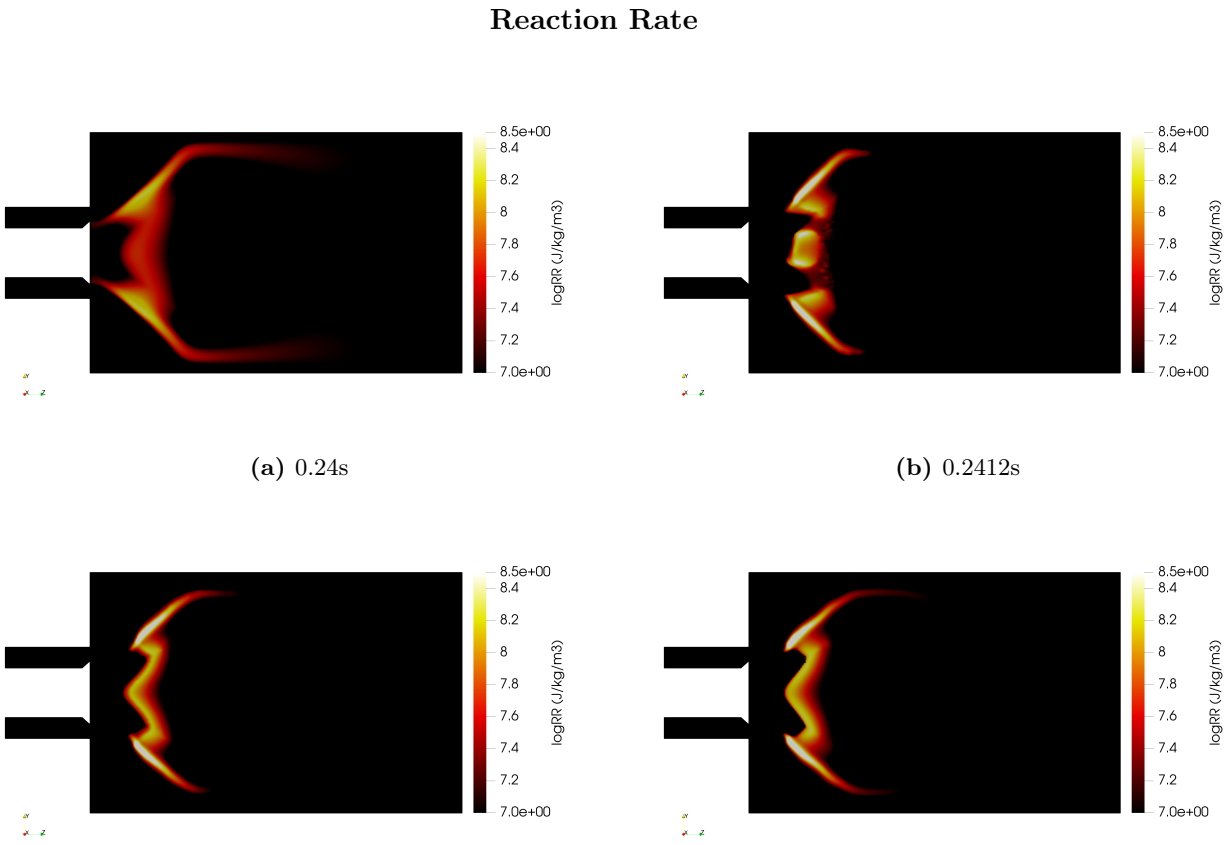

(a) 0.24s

(b) 0.2412s

(c) 0.2463s

(d) 0.2538s

Figure 4.42: Reaction rate for different time instants with the CERFACS chemical mechanism for the n-heptane reacting case (logarithmic scale).

4.2.3 H1S1: High-temperature chemical mechanism

Another n-heptane chemical mechanism has been used for the simulation with 37 species and designed for high-temperature ignition. This mechanism suits the conditions since the goal is to have a mechanism which correctly reproduces the ignition of the fresh mixture once it comes into contact with the hot-gas combustion products inside the chamber.

The objective of this simulation is to try to reproduce the flame both in a qualitative and quantitative way due to the failure in this sense of the previous mechanism.

Unfortunately, this mechanism has failed since the flame has been extinguished shortly after starting the simulation. The results that justify this event are shown below. This simulation has been carried out in the same way as the previous one, it has started from 0.24 seconds. It has been faster than the previous one in terms of computational cost, which was expected because the number of species and reactions was lower, and simulated up to 0.3 seconds.

In the Figure 4.43, The temperature begins to drop from the moment the simulation with this mechanism starts. At 0.27s the combustor has a temperature of about 290K throughout its length.

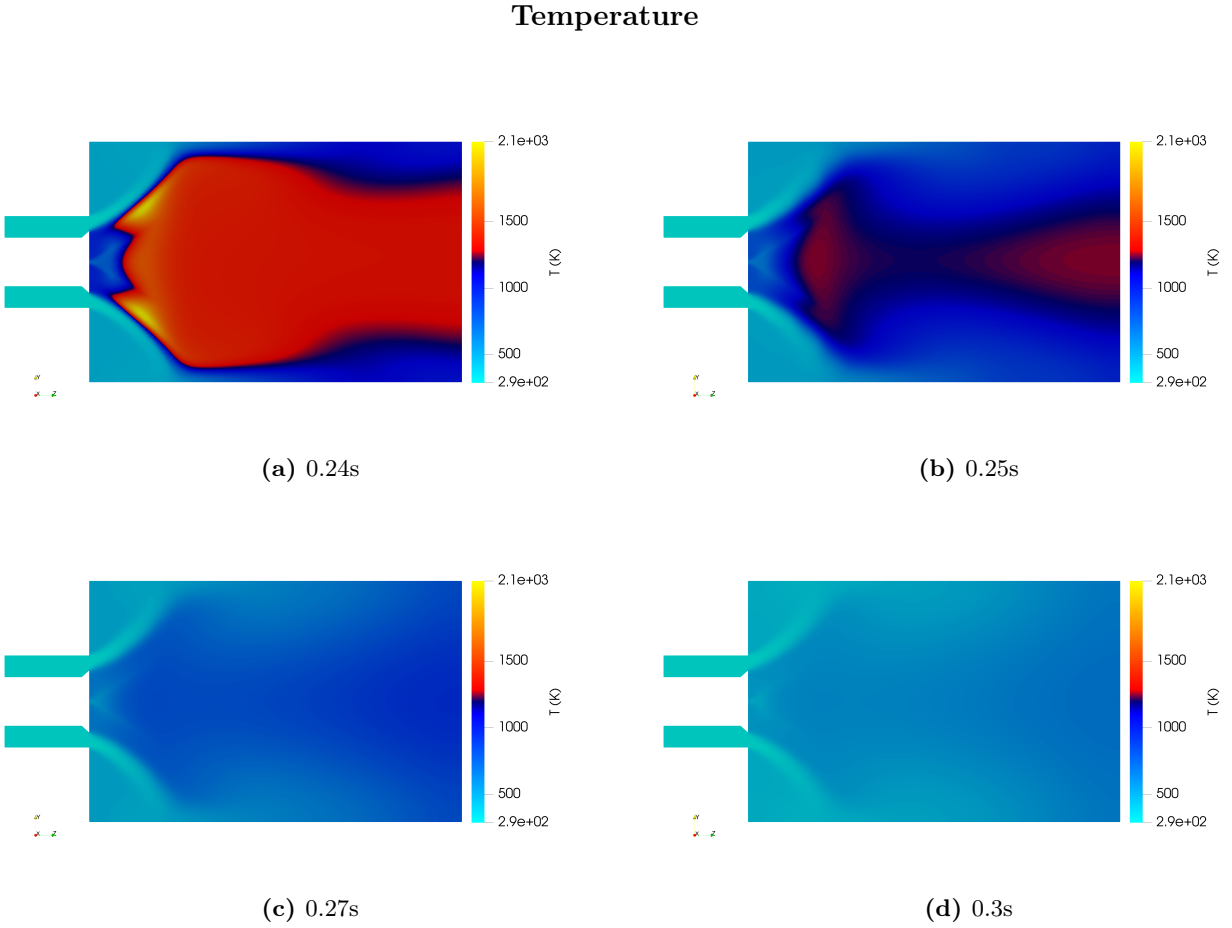

(a) 0.24s **(b)** 0.25s

(c) 0.27s **(d)** 0.3s

Figure 4.43: Temperature for different time instants with the high-temperature chemical mechanism for the n-heptane reacting case.

This aligns perfectly with the reaction rate results which are displayed in the Figure 4.44. As can be seen in the RR, according to the range of interest studied in the previous simulations on the logarithmic scale, in this case at an instant 0.25 seconds, there is no flame or reaction, so it can be said that the flame has been extinguished.

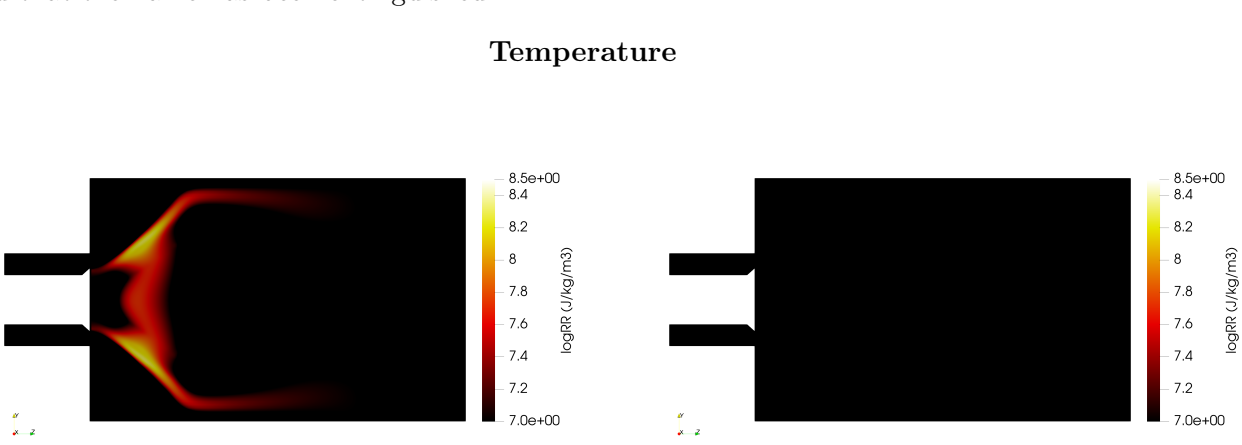

(a) 0.24s **(b)** 0.25s

Figure 4.44: Reaction rate for different time instants with the high-temperature chemical mechanism for the n-heptane reacting case (logarithmic scale).

The same occurs with the OH mass fraction, which has been previously used to compare with the Cambridge repository results. The mass fraction of OH at 0.25 seconds is of the magnitude order of 10^{-11}, while in with the CERFACS mechanism the magnitude order is of 10^{-03}.

This shows that this mechanism does not serve to represent the case of study and that the CERFACS mechanism has been more successful in the simulation of the case.

Chapter 5

Conclusions and Future Work

5.1 Conclusions

In this section, the conclusions obtained after the completion of this project are detailed.

First of all, **validation** has been successfully achieved with the non-reactive cases of cold air simulation. When comparing the numerical results with the experimental ones regarding axial, radial, and swirl velocities at different positions along the longitudinal axis of the combustor, it is confirmed that they are nearly identical. Furthermore, the various recirculation zones known in confined swirl flows can be identified.

Furthermore, concerning the non-reactive cases, it can be stated that increasing the bulk velocity does not affect the normalized velocity profiles. The same normalized velocity profiles are obtained in cases C1 (U_{bulk}=14.3 m/s) and C2 (U_{bulk}=18.5 m/s).

The reactive case (H1S1) of a single heptane step is useful as a precondition for the chemical mechanisms subsequently used. In this case, the main combustion products can be observed. By analyzing these products and reactants, it is possible to determine the typical structure of a **diffusion flame** with a turbulent jet. In this structure, the flame front acts as a sink for fuel and oxygen. Additionally, thanks to the reaction rate, the flame has been observed perfectly, which correlates with the temperature being highest at the flame front.

In addition to this, for the single-step case, a brief analysis of the fuel spray droplets injected into the combustion chamber has been conducted. In this analysis, it is possible to observe the distribution that the droplets follow and how atomization and evaporation occur. Thanks to the representation, it is evident that the diameter of the droplets decreases as they move away from the injector (atomization). The temperature representation shows that these droplets reach a maximum temperature, which is the boiling temperature of heptane (evaporation).

All the comments about the previous results have not been validated with any experimental case, but the analysis of this case has helped recognize known phenomena through prior literature review and the study of similar cases. However, the case of one chemical step is very fast and does

not take into account chemical kinetics, which is why unrealistic values are obtained. For example, overprediction of temperature. That is why its results are not really representative and to draw relevant conclusions it is necessary to perform the simulation with a chemical mechanism.

Lastly, the single-step case has served to better understand the functioning of these simulations in OpenFOAM. With the time evolution of the reaction rate, it can be observed how the flame (reaction zone) forms and then remains anchored and static after a certain point in time. The time evolution of temperature is useful for understanding how the ignition process has been simulated in the software, adding hot air initially until combustion occurs and is self-sustained, and then gradually reducing the temperature to obtain the final distribution.

Regarding the case with the CERFACS chemical mechanism, as an initial conclusion, it can be stated that the **significant computational cost** associated with simulating a reactive case with only some intermediate species has been confirmed. This simulation was completed in approximately three weeks, using a skeletal mechanism.

The results with the CERFACS chemical mechanism for the reactive heptane case have indeed been compared to the experimental results from the University of Cambridge. When comparing the results, the first observation is that the flame is unanchored, and the **lift-off phenomenon** is observed, while the flame shape is represented correctly. This has been verified through the mass fraction of OH and the reaction rate.

Since in the single-step heptane case the flame is not lifted, the reason why flame is displaced seems to be the chemical mechanism used, as it accounts for very **slow chemical kinetics**. There are other factors that can affect this phenomenon, such as the volatility of the fuel. Compared with previous publications, heptane, although in other studies it exhibits lift-off despite being a highly volatile fuel, does not significantly contribute to the displacement of the flame or increased lift-off height. While the nature of the fuel can have some influence, the comparison between the single-step case, where the flame is anchored, and the case with the chemical mechanism leads to the conclusion that it is this chemical mechanism that is responsible for the flame being displaced.

The fact that the flame is lifted makes it impossible to compare the numerical case with the experimental one in a quantitative manner, with the axial velocities provided by Cambridge University. Therefore, concerning this reactive case and taking into account all the previous comments, it can be concluded that **the flame's topology has been reproduced**, specifically as an M-type flame. Thus with the CERFACS mechanism, a qualitative reproduction has been achieved, but not a quantitative one.

Through the temporal analysis of the case with the CERFACS mechanism, it has been confirmed that the lift-off phenomenon is not a precursor to the well-known blow-off, in which the flame continues to move until it extinguishes. The reaction rate figures make it evident that the flame is separated from the very beginning when using this mechanism and remains in the same longitudinal position throughout the simulation.

The second mechanism used of 37 species has not worked since the flame has been extinguished with it. This emphasizes the importance of employing suitable chemical kinetics to achieve a precise simulation of experimental scenarios. That is, the choice of the chemical mechanism is not trivial.

In conclusion, as a general overview of the project, it can be said that through the completion of this project, there has been a basic level of learning regarding the use of OpenFOAM software, including the use of terminal commands and programming in C++. Additionally, proficiency with the post-processing program Paraview has been developed. The project has expanded the understanding of CFD simulations in the context of combustion in swirling flows. Furthermore, concepts previously learned about combustion, computational fluid dynamics, fluid mechanics, and gas turbine combustors, among others, have been applied.

5.2 Future work

After completing the execution of this project, it is important to identify the logical steps to follow in order to continue with the research that has been conducted.

- Conducting simulations with other chemical mechanisms for the heptane case is essential to achieve both quantitative and qualitative representation. In this project, the significant impact of the results depending on the chosen chemical mechanism has been confirmed. Future simulations can be carried out using mechanisms containing more species, which will provide a more accurate representation of combustion reality but will also entail higher computational costs.

- Conduct simulations with the other single component fuels for which the University of Cambridge provides data and follow the same steps as those carried out for heptane. This approach allows for a broad spectrum of validated cases for this geometry.

- Investigate multi-component fuels that are more realistic and require the development of surrogates needed for the numerical study of these fuels. Surrogate mixtures are created to mimic the thermophysical, thermochemical, and chemical kinetic characteristics of the actual fuel, enabling the performance of fundamental experiments and predictive simulations. This is why they are so crucial in the study of fuels that the industry deals with to enhance the current environmental situation.

- Study of SAFs. All the previous steps are useful for the future development of sustainable aviation fuels using the CFD tool.

Part II

Economic cost

Chapter 6

Economic cost

In any engineering project, it is necessary to calculate the economic cost associated with the human labor, equipment, and resources required for its execution. In this chapter, the cost of this master's thesis will be detailed.

To enhance comprehension of each aspect, the budget will be segmented into categories encompassing personnel costs, operational expenses, equipment outlays, total expenditure, and net margins and profits.

6.1 Personnel expenditure

This project has been carried out by the student Laura Martínez Ruiz with the assistance and guidance of Jacopo Liberatori (a doctoral student at the University of Rome, La Sapienza), Professor Pietro Paolo Ciottoli from the University of Rome, La Sapienza, and Professor Luis Miguel García-Cuevas González from the Universitat Politècnica de València (UPV). Since this master's thesis was conducted during a period of mobility in Rome, Professor Pietro Paolo Ciottoli has acted as the tutor at the host university (external tutor), and doctoral student Jacopo Liberatori as the co-tutor (external co-tutor). Professor Luis Miguel García-Cuevas González is the tutor at UPV.

The student's salary has been estimated based on the salary of a Junior aerospace engineer in Spain, which is approximately 24000€ per year, equivalent to 8.27€ per hour. In this project, the student has dedicated the equivalence of 8 hours per day for a period of 3 months, totaling 720 hours of work.

The tutor at UPV, Luis Miguel García-Cuevas González, has devoted approximately 5 hours to project supervision. The annual salary for a contracted Ph.D. holder, as in this case, is 30139.94€ per year for 1700 annual hours, which amounts to 17.72€ per hour.

The salary for a doctoral student at the University of Rome, La Sapienza, is 1200€ net per month, with a total annual amount of 13638.47€. Which, for approximately 1700 hours worked in a year, would amount to around 8€ per hour.

Since this budget calculation has been based on salary values in Spain, and this master's thesis

is defended in Spain, the same salary assumptions are applied to the professor from Rome.

Due to a lack of information, the salary of the tutor in Rome, as well as social security contributions, will be calculated based on the values in Spain at UPV.

The total personnel cost can be observed in Table 6.1.

Subject	Dedicated time (hours)	Salary (€/hour)	Total salary (€)
Laura Martínez Ruiz	720	8.27	5954.4
Jacopo Liberatori	60	8	480
Pietro Paolo Ciottoli	10	17.72	177.2
Luis Miguel García-Cuevas González	5	17.72	88.6
Total personnel cost			**6700.2**

Table 6.1: Personnel cost for the project.

Since the salary of the tutor are linked to the economic activity of UPV, the government must pay additional contributions on their gross salaries, as expressed in Table 6.2.

Concept	Amount (%)
Common contingencies	23.60
Unemployment	5.50
Vocational training	0.60
AT y EP	1.50
FOGASA	0.20
Total	**31.40**

Table 6.2: Social security contributions.

That's why an additional 234.18€ must be taken into account from the salaries of the tutors and co-tutor.

Therefore, the total personnel cost would amount to **6934.38 €**.

6.2 Operational cost

Operational costs should include expenses related to travel, software licenses, and the cost of materials used for the project's execution.

To carry out the project, weekly trips were made to the University of Rome, La Sapienza, for approximately four months. These trips were conducted using public transportation in the city of Rome. The cost of these trips is **48€** , as each round trip incurred an expense of 3€.

The software used is as follows:

- Matlab. The license used has been provided by UPV, and the cost of the license is 250€ per student per year. Since the project was developed over 4 months, it incurs a cost of 83.3€.
- Mathematica. This software is also available through UPV's license. According to the Wolfram website, an academic personal license is priced at 1789€ per year. For the four months of usage in this project, the cost totals 596€.

Software	Monthly cost (€/month)	Total cost (€)
MATLAB	20.83	83.32
Mathematica	149.08	596.32
Microsoft Teams	4.2	16.8
IVA		21%
Total software cost		**842.69**

Table 6.3: Software license costs.

- Microsoft Teams. This software has been used to facilitate remote communication with project tutors when needed. The university provided it under a student license, which incurs a monthly cost of 4.20€.
- OpenFOAM. This is the software used for CFD simulations. It did not incur any additional costs for the project as it is freely available.
- ParaView. For post-processing the results obtained from OpenFOAM, we used this program, which also did not result in any additional costs as it is freely available.

The pricing details for the use of the different software programs employed are presented in the Table 6.3.

Furthermore, during the completion of the bachelor's thesis, a laptop computer has been employed, and the workspace has been illuminated with LED light bulbs.

All these associated costs are displayed in Table 6.4.

	Consumption (W/h)	Unit cost of electricity (€/kWh)	Total cost (€)
Laptop	100	0.2298	16.55
Lighting	1.2	0.2298	0.08
IVA			21%
Total electricity consumption cost			**20.12**

Table 6.4: Total project electricity consumption cost.

When the costs of travel, licenses, and consumption are combined, the total operational project cost amounts to **910.81 €**.

6.3 Equipment costs

For the completion of this project, an ASUS Zenbook laptop was used, featuring 16 GB of RAM, 500 GB of internal storage, an 11th generation Intel Core i7 processor, and an Intel Iris Xe graphics card. The operating system utilized was Microsoft Windows 11. This computer was purchased in 2022.

The cost allocation for these items is based on a depreciation period of 4 years.

The cost associated with the electronic equipment used can be seen in the Table 6.5.

Electronic Equipment	Acquisition cost (€)	Usage period (months)	Total cost (€)
ASUS ZenBook	1200	4	**100**

Table 6.5: Electronic equipment cost for the completion of the project.

6.4 Total cost

Cost	Quantity (€)
Personnel	6934.38
Operational	910.81
Electronic equipment	100
Total	**7945.19**

Table 6.6: Total cost of the project.

If all the amounts obtained previously are added together, the total cost of the project can be observed in the Table 6.6.

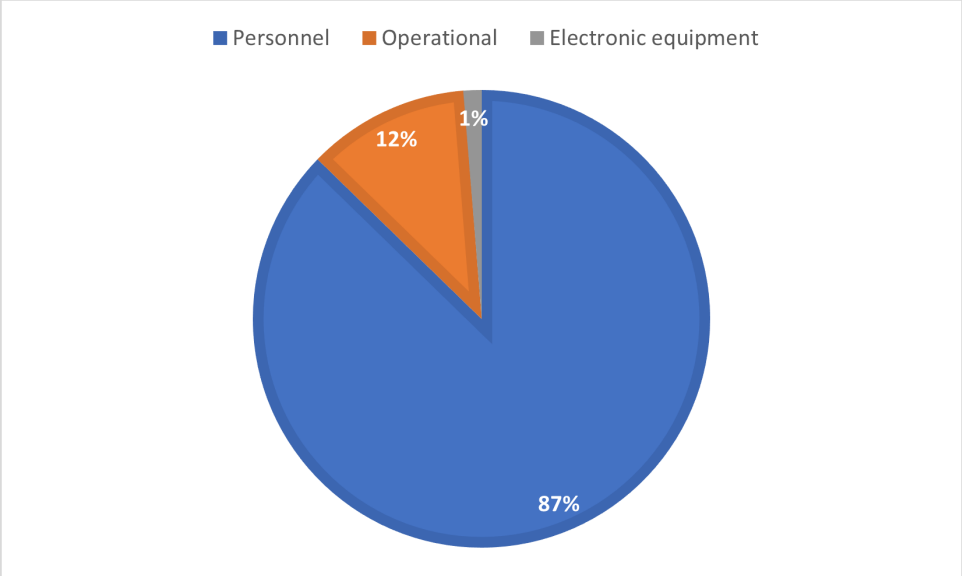

Figure 6.1: Pie chart of the total project costs.

In conclusion, it can be stated that the largest contribution to the cost comes from personnel, followed by operational costs, and finally equipment costs. This can be observed in the Figure 6.1.

Part III

Terms and conditions

Chapter 7

Terms and conditions

This project operates in accordance with the Spanish legal regulations regarding workplace safety and health, as specified in Royal Decree 488/1997 dated April 14th. The Royal Decree 488/1997, issued on April 14th, outlines the basic safety and health regulations for tasks involving equipment containing display screens. This legislation ensures compliance with Law 31/1995, dated November 8th, on Occupational Risk Prevention.

Most of the work has been carried out remotely, involving collaboration between the University of Rome, La Sapienza, and UPV. For this reason, it is also part of the legal framework of UPV, which will be elaborated upon further.

7.1 Legal framework

7.1.1 General conditions

This legislation is divided into six articles, three transitional provisions, and annexes.

- **Article 1** of this Royal Decree establishes the minimum safety and health provisions for the use of equipment with display screens by workers. These provisions are fully applied within the framework of Law 31/1995 on Occupational Risk Prevention. However, certain cases are excluded from the scope of this Decree, such as driving positions in vehicles or machinery, computer systems in means of transportation, computer systems for public use, portable systems not used continuously in workplaces, calculators, cash registers, and classic-design machines commonly known as "window machines."

- **Article 2** establishes some definitions useful for this framework. A "display screen" is defined as any alphanumeric or graphic screen, regardless of the visual representation method used. A "workstation" refers to equipment with a display screen, a keyboard or data acquisition device, a program for person/machine interconnection, office accessories, as well as a seat, table or work surface, and its immediate work environment. Lastly, a "worker" is any person who regularly uses equipment with a display screen.

- **Article 3** of this Royal Decree establishes the employer's obligations when it comes to the use of equipment with display screens by workers. The employer must take measures to prevent risks to workers' health and safety, including risk assessment, limiting screen work duration,

and scheduling breaks if necessary. Other activity changes can be specified and further detailed in collective agreements.

- **Article 4** sets up that the employer must guarantee the right of workers to adequate health surveillance, especially concerning risks to vision, physical issues, and mental strain associated with the use of display screens. This surveillance, conducted by competent healthcare personnel, shall be carried out in accordance with guidelines and protocols established by health authorities. It shall be offered to workers before the start of the work with a display screen, with a frequency adjusted based on the level of risk as determined by the responsible physician, and when disorders related to this type of work appear. If the medical surveillance states the need for ophthalmological examination, workers have the right to it and if it is demonstrated that special corrective devices are required to protect vision and normal devices are not suitable, the employer must provide them to workers free of charge.

- **Article 5** of this regulation establishes the employer's responsibilities regarding information and training. In compliance with the provisions of the Occupational Risk Prevention Law, the employer must ensure that workers and their representatives receive adequate training (before the start of the work and during it if it is needed) and are informed about the risks associated with the use of equipment with display screens. Additionally, the employer must provide information to workers on all aspects related to safety and health in their workplaces, following the provisions explained in the preceding sections of the regulation.

Furthermore, this legislation contains an **annex**. This appendix establishes minimum provisions related to the use of equipment that includes visual display screens in the workplace. It focuses on aspects such as the equipment itself, including the screen, keyboard, work table or surface, and the work chair. It also addresses the workplace environment, including space, lighting, the management of reflections and glare, noise, heat, electromagnetic emissions, and humidity. Additionally, it focuses on the interconnection between the computer and the person, emphasizing the importance of adapting programs to the task, facilitating their use, providing information about their operation, and applying ergonomic principles in the handling of information by the user. These provisions aim to ensure a safe and healthy working environment for those who use equipment with visual display screens.

7.1.2 UPV master's thesis regulations

La *Universitat Politècnica de València (UPV)* has also a legal framework regarding the development of the master's thesis. This regulation appears in the Consolidated Text.BOUPV 29-03-2018 and its subsequent modification approved by the Governing Council on 23-12-2021. A brief summary of this regulation is presented below and an explanation of how has it been implemented in the project.

Additional Provision 1. Completion of the Bachelor's or Master's Thesis during mobility stays.

First of all, this project has been conducted as a part of a mobility program at University of La Sapienza in Rome. The regulation for thesis completion of the Bachelor's or Master's Thesis during

mobility stays establishes the following[1]:

1. The completion of a Bachelor's or Master's Thesis during a mobility stay at another university requires prior approval of the research proposal (to be submitted by the student through the institutional computer tool) by the Academic Tutoring Committee (CAT).

2. Every Bachelor's or Master's Thesis developed during mobility stays must have a supervisor at the host university as well as at UPV.

3. The thesis defence can be carried out at the host university or at UPV, depending on the exchange agreement between the universities. If the defence takes place at UPV, it will be governed by the provisions outlined in Article 13.

4. When the defence is conducted at the host university, the student, upon completing the thesis, must submit a copy of the documentation through the institutional computer tool. The grade will be recorded in the student's academic record after receiving the corresponding minutes, following the grade equivalence table specified in the exchange agreement or, in its absence, as per the Qualifications Equivalence Table published by the Office of International Exchange Programs.

The compliance of the prior regulation has been done as the CAT has approved the master's thesis within the timeframe proposed by UPV (May 31, 2023). Furthermore, the supervisor at the host university is Prof. Pietro Paolo Ciottoli while the supervisor at UPV is Prof. Luis Miguel García-Cuevas González. The defence of the project will be done at UPV since it is possible as previously explained, so Article 13 is also of interest.

Article 13. Defence and Grading

This article regarding the defence and grading of the project establishes the following.

1. All Bachelor's or Master's Theses (TFG or TFM) are publicly defended unless there are restrictions due to confidentiality agreements or intellectual property rights.

2. At least four regular defence sessions will be scheduled throughout the academic year.

3. The ERT may establish extraordinary defense sessions to help students complete their degrees.

4. Each session will last as long as necessary to grade all papers meeting the requirements.

5. The defence involves a presentation of the work by the student and responding to questions from the tribunal.

6. The maximum duration of the defence is 45 minutes.

7. In justified cases, defence via videoconference is allowed with ERT authorization.

8. The tribunal grades the work according to established regulations and issues a report.

9. The grade is communicated to the student and recorded in a report signed by the tribunal's secretary.

[1]This text is the original regulation text translated (BOUPV Núm. 118/2022).

10. If the grade is "not pass," the tribunal provides explanations and necessary changes for the work to obtain a "pass" grade.

11. The "pass" grade is granted to the student once required modifications are made.

12. In exceptional cases and unanimously, a "With Distinction" honour may be awarded for grades between 9 and 10.

13. The grade is recorded in the student's academic record.

14. Appeals against grades can be submitted following the procedure outlined in the UPV Academic and Student Evaluation Regulations.

This project will be publicly defended in the extraordinary session between the 18th of September and the 28th of September as was previously accepted by the CAT.

Other articles of interest

Other articles of interest to mention are the following:

- **Article 2. Nature of Bachelor's and Master's Theses**: This article establishes that the Master's thesis must be oriented towards a subject and competencies associated with the master's degree, with a specified number of credits (ECTS). It also specifies that, even within a team, the defence must be individual. This is justified because in this project titled 'Numerical Analysis of the Cambridge Swirl Burner,' various disciplines learned during the master's degree are applied, such as combustion, computational fluid mechanics, turbulence, and boundary layer, among others.

- **Article 7. Enrollment for the Bachelor's Thesis and Master's Thesis**: Enrollment in the Bachelor's Thesis or Master's Thesis requires students to be registered for all remaining credits to complete their academic program. Enrollment must be done by the designated date in the academic calendar of the corresponding year, typically during self-enrollment. In exceptional cases, and with valid justification, the ERT may authorize enrollment after this date, but there is no guarantee of exemptions or fee discounts as per the current regulations. Enrolling in the TFG or TFM for an academic year grants the right to submit the work in any of the sessions held during that academic year, with no limit on the number of attempts, following the deadlines and procedures outlined in this framework regulation, as well as specific agreements of the ERTs or decisions made by the Governing Council.

  Based on these points, student Laura Martínez Ruiz enrolled electronically in the Master's Thesis course in July 2022, with the intention of completing and submitting it during the academic year 2022-2023, having successfully completed all previous credits and being enrolled in the corresponding courses for that academic year.

7.2 Carbon footprint of the project

The carbon footprint website is able to calculate the tons of CO_2 due to the performance of an activity, in this case: the master's thesis development.

As has been previously explained, some electricity has been consumed due to the electronic equipment and the lightning. The total consumption is 72.37kWh.

Besides, some trips have been made in order to have meetings with the supervisors with the Rome metro. The number of kilometres travelled is estimated as 48.

With all of this information and with the mentioned web the carbon footprint of this project is estimated as: **21 kg of CO_2**.

Bibliography

[1] D. A. Paraview, una aplicación para la visualización y el análisis de datos. https://ubunlog.com/paraview-aplicacion-para-visualizacion-y-analisis-de-datos/. Accessed: August 2023.

[2] A. Aissa, M. Abdelouahab, A. Noureddine, M. Elganaoui, and B. Pateyron. Ranz and marshall correlations limits on heat flow between a sphere and its surrounding gas at high temperature. *Thermal science*, 19(5):1521–1528, 2015.

[3] A. Akerblom. Turbulence-chemistry interaction in openfoam and how to implement a dynamic pasr model for les of turbulent combustion. *Lund University*, 2023.

[4] Y. M. Al-Abdeli and A. R. Masri. Review of laboratory swirl burners and experiments for model validation. *Experimental Thermal and Fluid Science*, 69:178–196, 2015.

[5] F. C. BastianiS. Cerfacs. https://chemistry.cerfacs.fr/en/chemical-database/mechanisms-list/nc7h18_25_210_27_fc-arc-mechanism/. Accessed: 27/07/2023.

[6] T. Boushaki, N. Merlo, C. Chauveau, and I. Gökalp. Study of pollutant emissions and dynamics of non-premixed turbulent oxygen enriched flames from a swirl burner. *Proceedings of the Combustion Institute*, 36(3):3959–3968, 2017.

[7] D. E. Cavaliere. *Blow-off in gas turbine combustors*. PhD thesis, University of Cambridge, 2014.

[8] M. S. Y. Cavaliere, Kariuki and co-workers in the University of Cambridge Department of Engineering. The swirl flames data repository. http://swirl-flame.eng.cam.ac.uk/. Accessed: 2023.

[9] R. C. Chanaud. Observations of oscillatory motion in certain swirling flows. *Journal of Fluid Mechanics*, 21(1):111–127, 1965.

[10] H. Chen, D. Zhao, Z. Zhang, T. Jia, R. Zhao, and Z. Qu. Design and development of explosion-proof cavity of hydraulic system power unit applied in explosion-proof area. *Processes*, 10(9):1824, 2022.

[11] H. W. Chris Greenshields. The pimple algorithm. https://doc.cfd.direct/notes/cfd-general-principles/the-pimple-algorithm, 2022. Accessed: July 2023.

[12] S. Creedy. Why flying can beat driving in terms of fuel efficiency. https://www.airlineratings.com/news/

how-flying-can-beat-driving-when-it-comes-to-fuel-efficiency/, 2018. Accessed: August 2023.

[13] H. J. Curran. Developing detailed chemical kinetic mechanisms for fuel combustion. *Proceedings of the Combustion Institute*, 37(1):57–81, 2019.

[14] W. Dynamics.

[15] P. Ekman. *Important Factors for Accurate Scale-Resolving Simulations of Automotive Aerodynamics*, volume 2068. Linköping University Electronic Press, 2020.

[16] J. Gimeno, P. Marti-Aldaravi, M. Carreres, and S. Cardona. Experimental investigation of the lift-off height and soot formation of a spray flame for different co-flow conditions and fuels. *Combustion and Flame*, 233:111589, 2021.

[17] J. Guerrero. Introduction to computational fluid dynamics: Governing equations, turbulence modeling introduction and finite volume discretization basics. *Predavanja, Veljača*, 2014.

[18] T. F. Guiberti, D. Durox, L. Zimmer, and T. Schuller. Analysis of topology transitions of swirl flames interacting with the combustor side wall. *Combustion and Flame*, 162(11):4342–4357, 2015.

[19] K. Hanjalí. Second-moment turbulence closures for cfd: Needs and prospects. *International Journal of Computational Fluid Dynamics*, 12(1):67–97, 1999.

[20] H. Hiester, M. Piggott, P. Farrell, and P. Allison. Assessment of spurious mixing in adaptive mesh simulations of the two-dimensional lock-exchange. *Ocean Modelling*, 73:30–44, 01 2014.

[21] Y. Huang and V. Yang. Dynamics and stability of lean-premixed swirl-stabilized combustion. *Progress in energy and combustion science*, 35(4):293–364, 2009.

[22] B. HUSTED. Turbulent mixing in the lower part of the smoke layer using the fire dynamic simulator. In *BOOK OF PROCEEDINGS*, page 213, 2017.

[23] S. Iavarone, A. Péquin, Z. X. Chen, N. A. K. Doan, N. Swaminathan, and A. Parente. An a priori assessment of the partially stirred reactor (pasr) model for mild combustion. *Proceedings of the Combustion Institute*, 38(4):5403–5414, 2021.

[24] IEA. Co2 emissions in aviation in the net zero scenario 2000-2030. https://www.iea.org/data-and-statistics/charts/co2-emissions-in-aviation-in-the-net-zero-scenario-2000-2030, 2023. Accessed: August 2023.

[25] S.-J. Jeong, S. Oh, H.-K. Lee, J. Park, G. Lee, Y.-D. Pyo, and O. Lim. Research and development of a 2.9 liter light-duty dme truck using common-rail fuel injection systems. In *KSAE Annual Conference Proceedings*, pages 393–402, 2011.

[26] X. Jiang, G. A. Siamas, and L. C. Wrobel. Analytical equilibrium swirling inflow conditions for computational fluid dynamics. *AIAA journal*, 46(4):1015–1019, 2008.

[27] M. Kaplan. Influence of swirl, tumble and squish flows on combustion characteristics and emissions in internal combustion engine-review. *International Journal of Automotive Engineering and Technologies*, 8(2):83–102, 2019.

[28] M.-K. Kim, J. Yoon, S. Park, M.-C. Lee, and Y. Yoon. Effects of unstable flame structure and recirculation zones in a swirl-stabilized dump combustor. *Applied thermal engineering*, 58(1-2):125–135, 2013.

[29] C. K. Law. *Combustion physics*. Cambridge university press, 2010.

[30] M. R. Lečić, A. S. Ćoćić, and J. M. Burazer. An experimental investigation and statistical analysis of turbulent swirl flow in a straight pipe. *Therm Sci 00*, pages 191–191, 2016.

[31] D. Lee, D. Fahey, A. Skowron, M. Allen, U. Burkhardt, Q. Chen, S. Doherty, S. Freeman, P. Forster, J. Fuglestvedt, A. Gettelman, R. De León, L. Lim, M. Lund, R. Millar, B. Owen, J. Penner, G. Pitari, M. Prather, R. Sausen, and L. Wilcox. The contribution of global aviation to anthropogenic climate forcing for 2000 to 2018. *Atmospheric Environment*, 244:117834, 2021.

[32] S. Lee, S.-J. Jeong, and O. Lim. An investigation on the spray characteristics of dme with variation of ambient pressure using the common rail fuel injection system. *Journal of Mechanical Science and Technology*, 26, 10 2012.

[33] A. H. Lefebvre and D. R. Ballal. *Gas turbine combustion: alternative fuels and emissions*. CRC press, 2010.

[34] F. Liu. A thorough description of how wall functions are implemented in openfoam. *Proceedings of CFD with OpenSource Software*, 34, 2016.

[35] T. Lu and C. K. Law. Strategies for mechanism reduction for large hydrocarbons: n-heptane. *Combustion and flame*, 154(1-2):153–163, 2008.

[36] M. Margulis and E. Gilad. Development and verification of the dynamic system code thermo-t for research reactor accident analysis. *Nuclear Technology*, 196(2):377–395, 2016.

[37] D. Martinez-Sanchis, A. Sternin, J. Shvab, O. Haidn, and X. Hu. An eddy dissipation concept performance study for space propulsion applications. *Aerospace*, 9(9):476, 2022.

[38] N. Merlo, T. Boushaki, C. Chauveau, S. de Persis, L. Pillier, B. Sarh, and I. Gokalp. Experimental study of oxygen enrichment effects on turbulent non-premixed swirling flames. *Energy & fuels*, 27(10):6191–6197, 2013.

[39] A. Parente, M. R. Malik, F. Contino, A. Cuoci, and B. B. Dally. Extension of the eddy dissipation concept for turbulence/chemistry interactions to mild combustion. *Fuel*, 163:98–111, 2016.

[40] C. Pichler and E. Nilsson. Analysis of important chemical pathways of n-heptane combustion in small skeletal mechanisms. *Energy & Fuels*, 34(1):758–768, 2019.

[41] A. Razak. *Industrial gas turbines: performance and operability*. Elsevier, 2007.

[42] J. Sanchez. Estudio del flujo en la tobera del motor cohete j-2s mediante técnicas cfd, 2014.

[43] D. C. Sert. Foamy lectures. cfd lectures with openfoam. `https://users.metu.edu.tr/csert/foamyLectures/lecture01.html`. Accessed: August 2023.

[44] J. Sidey, A. Giusti, P. Benie, and E. Mastorakos. The swirl flames data repository. *URL: http://swirlflame. eng. cam. ac. uk*, 2017.

[45] SimFlow. Openfoam gui – simflow cfd. `https://sim-flow.com/what-is-openfoam/`. Accessed: August 2023.

[46] M. Stefanizzi, S. Stefanizzi, V. Ceglie, T. Capurso, M. Torresi, and S. M. Camporeale. Analysis of the partially premixed combustion in a labscale swirl-stabilized burner fueled by a methane-hydrogen mixture. In *E3S Web of Conferences*, volume 312, page 11004. EDP Sciences, 2021.

[47] W. Sutherland. Lii. the viscosity of gases and molecular force. *The London, Edinburgh, and Dublin Philosophical Magazine and Journal of Science*, 36(223):507–531, 1893.

[48] G. Vignat, D. Durox, and S. Candel. The suitability of different swirl number definitions for describing swirl flows: Accurate, common and (over-) simplified formulations. *Progress in Energy and Combustion Science*, 89:100969, 2022.

[49] V. Yakhot, S. Orszag, S. Thangam, T. Gatski, and C. Speziale. Development of turbulence models for shear flows by a double expansion technique. *Physics of Fluids A: Fluid Dynamics*, 4(7):1510–1520, 1992.

[50] R. Yuan. *Measurements in swirl-stabilised spray flames at blow-off*. PhD thesis, University of Cambridge, 2015.

[51] R. Yuan, J. Kariuki, A. Dowlut, R. Balachandran, and E. Mastorakos. Reaction zone visualisation in swirling spray n-heptane flames. *Proceedings of the Combustion Institute*, 35(2):1649–1656, 2015.

[52] W. Zeng, M. Sjöberg, D. L. Reuss, and Z. Hu. The role of spray-enhanced swirl flow for combustion stabilization in a stratified-charge disi engine. *Combustion and Flame*, 168:166–185, 2016.

Appendix A

Degree of alignment of the project with the Sustainable Development Goals.

This annex presents the Table **??** that expresses the degree of alignment of the project with the sustainable development goals of the 2030 agenda.

Sustainable Development Goals	High	Medium	Low	Not applicable
1. No poverty				x
2. Zero hunger				x
3. Good health and well-being			x	
4. Quality education				x
5. Gender equality				x
6. Clean water and sanitation				x
7. Affordable and clean energy			x	
8. Decent work and economic growth			x	
9. Industry, innovation and infrastructure				x
10. Reduction of inequalities				x
11. Sustainable cities and comunities				x
12. Responsible consumption and production				x
13. Climate action			x	
14. Life below water				x
15. Life on land				x
16. Peace, justice and institutions				x
17. Partnerships of the goals				x

Table A.1: Degree of alignment of the project with the Sustainable Development Goals of the 2030 agenda.